



Laboratory for
Electromagnetic and
Electronic
Systems

Massachusetts
Institute of
Technology

Room 77
10-050 Massachusetts
Avenue

Cambridge
Massachusetts
02139-4307

Telephone
617-253-4883
Telex
92-1473
FAX
617-258-6774

February 1, 1995

Mr. John Harding
Federal Railroad Administration
400 Seventh Street, SW
Washington, DC 20590

Dear Mr. Harding,

Enclosed is a draft copy of the final report "Investigation of the Deleterious Effects of Electromagnetic Fields on Steel Rebar Used in Guideways for EDS Maglev Systems" for FRA Contract No. DTFR53-94-C-00008. Volume 1 is not yet complete.

Sincerely,

Vivian Mizuno
Administrative Secretary to
Professor R. D. Thornton

Enclosed

Continuum
Electromechanics

Electric
Power
Systems

High
Voltage

Power
Electronics
and Control

DRAFT

**Investigation of the Deleterious Effects of
Electro-Magnetic Fields on Steel Rebar
Used in Guideways for EDS Maglev Systems**

Volume 1, Summary

January 27, 1995

**by
Dr. Richard D. Thornton**

**with contributions from:
Dr. Markus Zahn
Mr. J. Richard Hale
Dr. Robert Pillsbury
Dr. Thanasis C. Triantafillou
Dr. Jerome J. Connor
Mr. Sanjay Srinivasan
Dr. H. A. Franklin
Ms. Janie Blanchard**

**And with help from other personnel at:
MIT Laboratory for Electromagnetic and Electronic Systems
MIT Plasma Fusion Center
MIT Department of Civil and Environmental Engineering
Bechtel Corporation**

**Project done with support from
DOT FRA**

**Mr. Michael Coltman
Contracting Officer's Technical Representative**

Introduction

This report summarizes work done on an FRA contract to study the important interactions of magnetic fields with rebars. The work was done as 5 distinct tasks:

- Task 1 — Perform Magnetic Field Analysis
- Task 2 — Conduct Literature Search
- Task 3 — Characterize Interactions/Effects With Steel Re-Bar
- Task 4 — Develop Design Guidelines
- Task 5 — Define Test Procedures

This report is organized as 2 reports. Volume 1 is a summary of the conclusions from the entire project and Volume 2 is a collection of detailed reports on the individual subtasks. The literature search uncovered a number of important references relative to each of the other tasks, so the results of Task 2 are included as part of the results of the other tasks. There are 4 sections in this report corresponding to Tasks 1, 3, 4 and 5 and a fifth section that is a very short summary of the major findings of the study.

1 Magnetic Field Analysis

1.1 Overview of effects of magnetic fields on steel rebar

This section presents an overview of how magnetic fields interact with rebar to create electrical power dissipation and mechanical force. Following sections discuss the results of theoretical analysis of generic and simplified cases and numerical calculations of particular cases, including calculations for the Bechtel and Foster-Miller maglev designs.

Magnetic fields in a rebar exposed to an axial, time varying magnetic field

The analytical determination of the sinusoidal steady state magnetic fields in cylindrical rods involves the use of Bessel functions with complex arguments, and this leads to tedious calculations. Fortunately there are computer programs, such as Matlab, that can do these calculations with relative ease and, more important, there are very good approximations that are adequate for the great majority of cases.

Consider first the case where the magnetic field is constant and oriented in the direction of the rebar axis as shown in Figure 1.1.

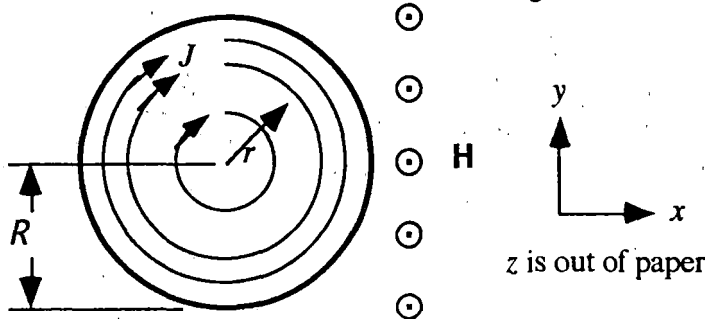


Figure 1.1. Axial, time varying field in a cylindrical conductor.

The external changing magnetic field H creates circular electrical currents J in the rebar with a direction that produces a reaction field that tends to reduce the field interior to the rebar. The magnitude of the current is proportional to the magnitude of the exciting magnetic field and the field at the periphery of the rebar matches the applied field.

If the product of electrical frequency, rebar radius, rebar magnetic permeability and rebar electrical conductivity is small, then the currents do not produce a very large reaction field so the total field can be assumed to be essentially uniform and equal to the applied field throughout the rebar. This is called the "large skin depth" approximation. It is a good approximation for normal size rebars with frequencies below about 2000 Hz if the rebar is made from nonmagnetic steel, such as some types of stainless steel, or with steel with about 13% manganese. It is also applicable to normal rebar steel if the frequency is less than about 0.5 Hz.

If the product of electrical frequency, rebar radius, rebar magnetic permeability and rebar electrical conductivity is large, then the circulating currents create a field that can be assumed to be negligible except near the surface of the rebar. This is called the "small skin depth" approximation. It is a good approximation for normal magnetic steel rebars with electrical frequencies greater than about 0.5 Hz. It is also applicable to nonmagnetic steel rebars at frequencies greater than about 2,000 Hz.

For the case of an applied axial filed the field, the field inside and outside the rebar are as given in Equation 1.1.

$$\begin{aligned} r \leq R: \mathbf{H} &= \hat{\mathbf{z}} H_z = |H_z(r)| \cos(\omega t + \theta(r)) \\ r \geq R: \mathbf{H} &= \hat{\mathbf{z}} H_0 \cos(\omega t) \end{aligned} \quad (1.1)$$

$$\text{Boundary condition at } r = R: |H_z(R)| = H_0, \theta(R) = 0$$

In this Equation the constant \mathbf{z} directed field H_z is assumed to be a complex number with the magnitude representing the peak value of the filed and the phase angle representing the phase shift of the field relative to the field at the surface. For the following discussion we focus on the magnitude of the field since this is the key to determining the forces and power loss.

The exact solution involves the Bessel Function J_0 with complex arguments as given in Equation 1.2. This solution leads to complex calculations that are possible but usually unnecessary. Shown in Figure 1.2 is an approximate solution: for $r < 1.17$ the field is assumed to be constant and for $r \geq 1.17$ the field is assumed to increase exponentially with r . A plot of field strength H_z vs. radius is shown in Figure 1.2. In this plot the axial position r is normalized by dividing it by the skin depth δ . Expressions for both the exact and approximate solutions are given in Equation 1.2. Note that the approximation is fairly good over the entire range of r and is very good at the extremes of small and large r .

$$\begin{aligned} |H_z| &= |H_z(r=0)| J_0\left(\frac{(1-j)r}{\delta}\right) = |H_z(r=0)| J_0(\sqrt{-j\omega\mu\sigma} r) \\ \text{If } r < 1.17: |H_z| &\approx |H_z(r=0)| \\ \text{If } r \geq 1.17: |H_z| &\approx |H_z(r=0)| \frac{e^{r/\delta}}{\sqrt{2\pi\sqrt{2}(r/\delta)}} = |H_z(r=0)| \frac{e^{\sqrt{\omega\mu\sigma/2} r}}{\sqrt{2\pi r \sqrt{\omega\mu\sigma}}} \end{aligned} \quad (1.2)$$

$$\text{Where skin depth } \delta = \sqrt{\frac{2}{\omega\mu\sigma}}$$

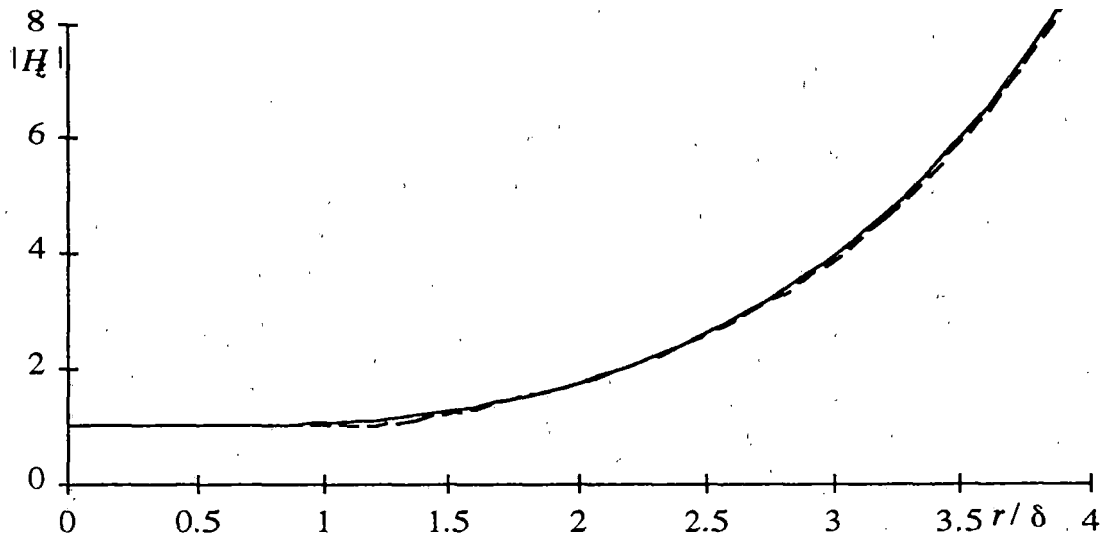


Figure 1.2. Magnitude of axial, time varying magnetic field in a rebar.

The phase shift is not shown in Figure 1.2 but must be considered in a detailed analysis. In fact, a good simplified model of the behavior is to assume that a "magnetic wave" impinges on the surface of the rebar and propagates into the interior. If the small skin depth approximation is valid, then it can take several cycles of the electrical frequency for the wave to propagate to the center of the rebar. Unless the excitation persists for several cycles the sinusoidal steady state will not be reached.

Electrical current in a rebar exposed to an axial, time varying magnetic field

Once the magnetic field is determined, the currents are readily found because they are proportional to the rate of change of magnetic field. Thus, Equations 1.2 for \mathbf{H} field become Equations 1.3 for the \mathbf{J} field.

$$|J_{\phi}| = \frac{|H_z(r=0)|\sqrt{2}}{\delta} J_1\left(\frac{(1-j)r}{\delta}\right) = \frac{|H_z(r=0)|}{\delta} J_1(\sqrt{-j\omega\mu\sigma} r)$$

$$\text{If } r \leq 1.17: |J_{\phi}| \approx \frac{|H_z(r=0)|}{\delta} \frac{r}{\sqrt{2}} = |H_z(r=0)| \frac{\omega\mu\sigma r}{2} \quad (1.3)$$

$$\text{If } r > 1.17: |J_{\phi}| \approx \frac{|H_z(r=0)|}{\delta} \frac{e^{r/\delta}}{\sqrt{2\pi\sqrt{2}(r/\delta)}} = |H_z(r=0)| \sqrt{\frac{\omega\mu\sigma}{4\pi}} e^{\sqrt{\omega\mu\sigma/2} r}$$

Note that J_0 and J_1 are Bessel Functions, not current densities, and that the skin depth is as defined in Equation 1.2.

The exact and approximate current density is shown in Figure 1.3. Note that \mathbf{J} has a *sinh* like behavior while \mathbf{H} has a *cosh* like behavior. If the geometry were planar instead of cylindrical, then the *sinh* and *cosh* functions would replace the J_0 and J_1 Bessel functions. All of these functions predict exponential behavior for large arguments and the magnitude increases by a factor of about e when the distance increases by one skin depth.

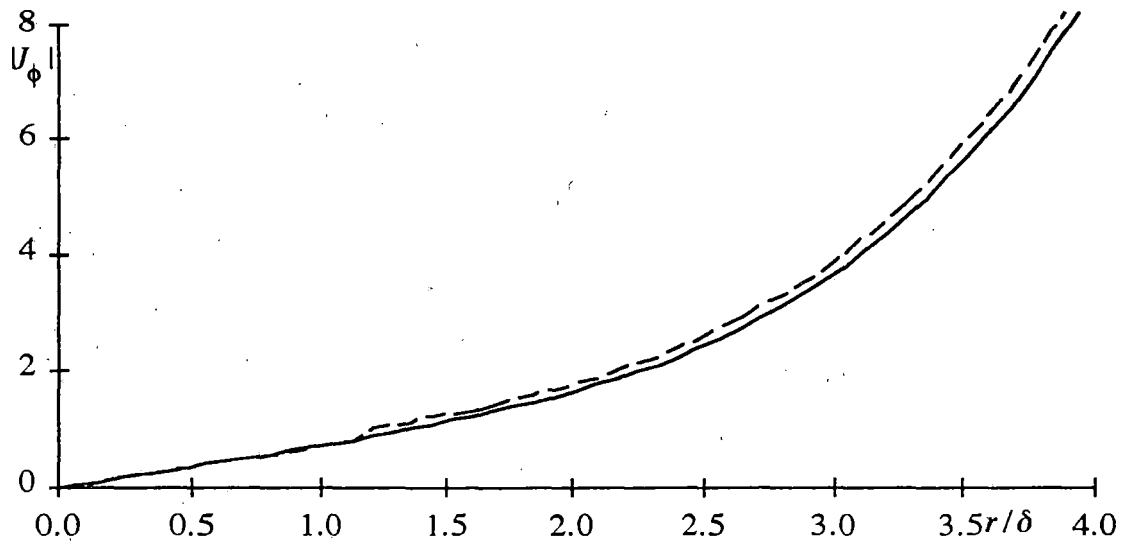


Figure 1.3. Magnitude of radial, time varying currents in a rebar.

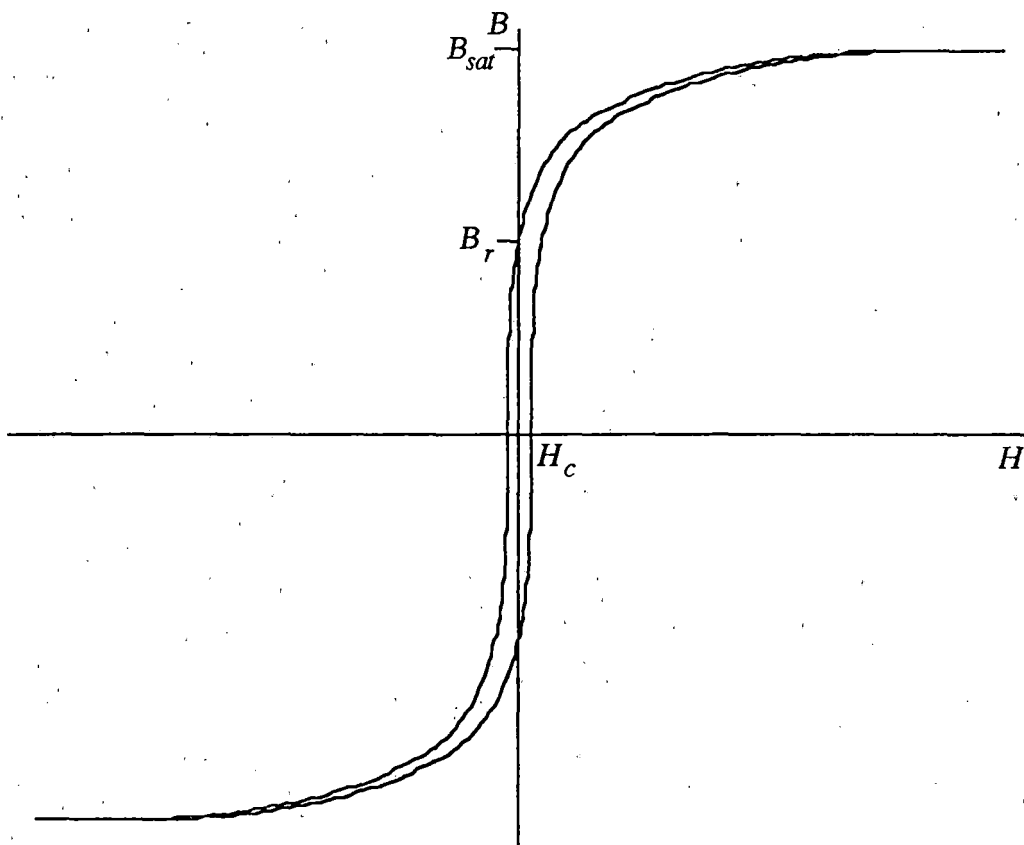


Figure 1.4. Typical magnetization curve for a ferromagnetic material.

Effect of nonlinearity in the B-H characteristic

If a rebar has a high magnetic permeability, as is the case for ordinary mild steel, then the nonlinearity in the B-H characteristic can play a major role. Figure 1.4 shows a

typical magnetization characteristic for steel. The H field in the rebar and near the surface must match the applied field, and this Figure shows that it takes very little H field for major nonlinearities to be important. The effect is to cause saturation at the surface of the rebar where the field is high, and the magnitude of H will be less than predicted by the preceding linear analysis. When the field is strong enough for saturation we can visualize a large skin depth for fields near the surface but a small skin depth once the field attenuates to the center of the rebar. Thus we can imagine a flattening of the exponential curves, shown in Figure 1.2 and 1.3, for large r . The problem is that the nonlinear magnetization creates harmonics of the excitation frequency and a simple linear model is not possible.

Table 1.1. Electrical properties of various metals at 20° C.

Material	μ/μ_0	$\rho, \mu\text{ohm-m}$	δ at 60 Hz, mm
Copper	1	0.01724	8.5
Aluminum	1	0.0283	10.9
Steel: rebar	3000	0.208	0.54
13% Mn	1	0.678	53.5
stainless	1	0.910	62.0

Table 1.2. Magnetic properties of typical steel

	Symbol	Units	M19
Saturation flux	$B_{sat}(H)$	T	1.8
H for B_{sat}	H_{sat}	a/m	1000
Coercive force	H_c	a/m	10
Remnant flux	B_r	T	0.8
Initial permeability	μ_i		2000

The nonlinearity problem is primarily important when the skin depth is small, for the following reasons. If the skin depth is large the field is nearly uniform in the rebar and is not much greater than the applied field. For the case where the field is provided by a passing magnetically suspended vehicle, the applied field is only a fraction of one Tesla and this is not enough to cause major problems with nonlinearities in most steels. However, when the skin depth is large the field is heavily concentrated near the surface, and then the B field in the rebar and near the surface can be many times larger than the applied B field.

One method of dealing with the nonlinearity is to use a lumped circuit model as shown in Figure 1.5. This model is particularly convenient for dealing with the small skin depth case because then we can use a planar model that treats the surface of the rebar as though it were a flat sheet. The inductors in this model can be thought of as representing the B-H characteristic of a thin layer of steel and thus all inductors have identical nonlinear characteristics. If we neglect hysteresis, then the resistors in the model are linear. There are very efficient algorithms for predicting the currents and voltages in this lumped circuit model for the case of an applied field of any frequency or shape. Thus we can use non sinusoidal excitation and accurately predict the magnetic field, the electric current and the power dissipation in the rebar. We can even add circuit elements that will model the hysteresis loss, but this is not expected to be nearly as large as the eddy current power loss that is represented by power dissipation in the resistors in the model.

{For the final report this method will be expanded and some results presented.}

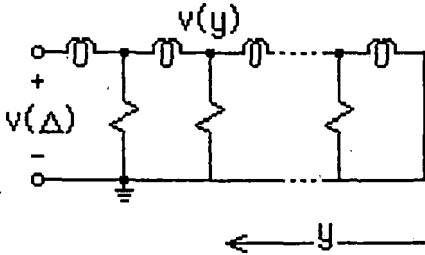


Figure 1.5. Lumped model for magnetic field analysis.

Magnetic fields in a rebar exposed to a transverse, time varying magnetic field

The preceding analysis has focused exclusively on the case of a field that was in the direction of the axis of the rebar. In reality there is a complex field pattern. As the maglev vehicle passes the field changes from axial to transverse to axial in the opposite direction to transverse in the opposite direction etc. Even though we can not simply add the effects of the axial and transverse fields, it is very helpful to understand fully the effects when they are separate. Then, using an understanding based on the simple models, we are in a position to do detailed numerical analysis of a specific case.

In order to study the case of a transverse applied field, we model the magnetic and current fields as shown in Figure 1.6. The currents now flow in the axial direction and is largest near the top and bottom and zero in the center of the rebar pictured in Figure 1.6.

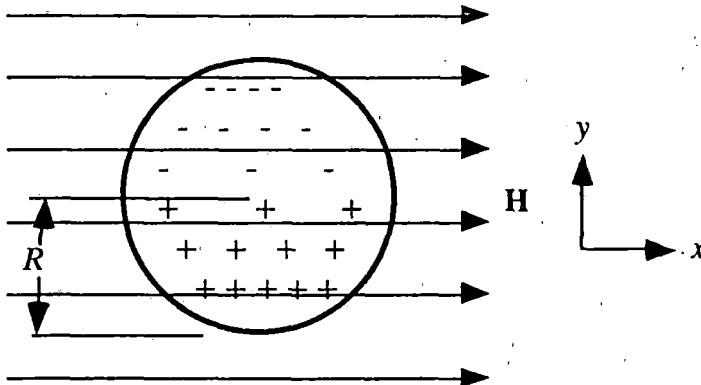


Figure 1.6. Transverse field in a cylindrical conductor.

In spite of the differences in the magnetic and current fields in the rebar, some aspects of the fields are very similar to what they were for the axial case. Most important, the skin depth is the same. Also, if the rebar is nonmagnetic, then the power loss is twice as large for the transverse case as for the axial case, assuming the same applied field. This suggests for a nonmagnetic rebar we can get a rough guide as to the power loss by simply adding the loss from the axial and transverse cases. This is not precisely valid, but it can tell us approximately how large an applied field we can allow and to stay within given power loss constraints. The next page gives some graphs, taken from Volume 2, that show typical power loss vs. electrical frequency for different sizes and types of rebar.

If the rebar is magnetic, then the fields and currents in the rebar are dramatically smaller for the transverse field than for the axial field. This is discussed later, but the result is that for a magnetic steel rebar the only important losses will be the ones due to the axial field while for a nonmagnetic rebar the losses will be comparable for the two types of excitation.

Mechanical force on rebar

A magnetic field can create a force on a rebar. If the rebar is magnetic, then there is a force even when the field is not changing. This is called the magnetic force. If the field is changing, then there is an additional component called the "Lorentz Force." This force is produced by the interaction of the induced currents with the magnetic field. The magnetic force is always attractive, meaning the rebar is pushed in the direction of increasing magnetic field strength while the Lorentz Force is always repulsive, meaning it pushes the rebar in the direction of decreasing magnetic field strength.

This study has shown that the mechanical forces are not large enough to damage the rebar or weaken the bond between the rebar and the concrete. They can, however, be large enough to affect the behavior of the vehicle.

When the vehicle is stationary there is an attractive force between the vehicle magnets and the guideway rebars. Most maglev designs, including both the Bechtel and Foster-Miller designs, use a symmetrical disposition of magnets and rebars. Hence the attractive forces tend to cancel and produce no lateral force on the vehicle. They could produce a vertical force, either up or down, but even here there tends to be cancellation because of the large number of rebars, so the total vertical force may not be a problem. The serious issue is the destabilization of lateral guidance. If the vehicle moves laterally from the symmetry position, then the forces will increase on one side and decrease on the other side so as to try to pull the vehicle further from the symmetry position. This destabilizing effect can create lateral forces greater than 10% of vehicle weight and must be considered in analyzing lateral guidance schemes.

The Lorentz force can have both good and bad effects. The worst effect is that the power loss in the rebars is translated into a Lorentz force that brakes the vehicle. All of the power dissipated in the rebars comes from this braking effect. The Lorentz force is, of course, the force that suspends a vehicle in an EDS system, but it is much more efficient to use a Lorentz force on an carefully designed aluminum suspension structure. A steel rebar can not provide efficient magnetic suspension because of the low conductivity of steel in comparison with the conductivity of aluminum or copper. For a magnetic steel rebar it is unlikely that the Lorentz force will ever be enough to cancel the magnetization force and we should try to minimize all Lorentz forces on a rebar. The next section presents some graphs that show these forces.

1.2 Symbolic analysis

Prof. Markus Zahn and several students have done an extensive symbolic analysis of the interaction of a magnetic field with a rebar. The analysis is quite general assuming only that the rebar is a long, round cylinder with constant conductivity and located in an almost uniform, time varying field. For much of the work the magnetic characteristics have been assumed to be linear, but some work addresses the nonlinearity issue. Selected graphs from this report are reproduced in this section. The detailed analysis and a additional graphs are given in a report in Volume 2.

Sinusoidal steady state power loss

Figures on the next page show the power dissipation as a function of electrical frequency. The graphs show results for a range of materials including mild steel used in normal rebars, 13% manganese (non magnetic) steel, stainless steel and aluminum. The plots show results for rebar radii of 0.5, 1 and 1.5 cm and for peak magnetic field of 0.5 Tesla. The power dissipation varies as the square of the field strength, so it is easy to extrapolate this data to other field intensities.

An important conclusion is that over a wide range of conditions the small and large skin depth approximations lead to accurate predictions and simple conclusions.

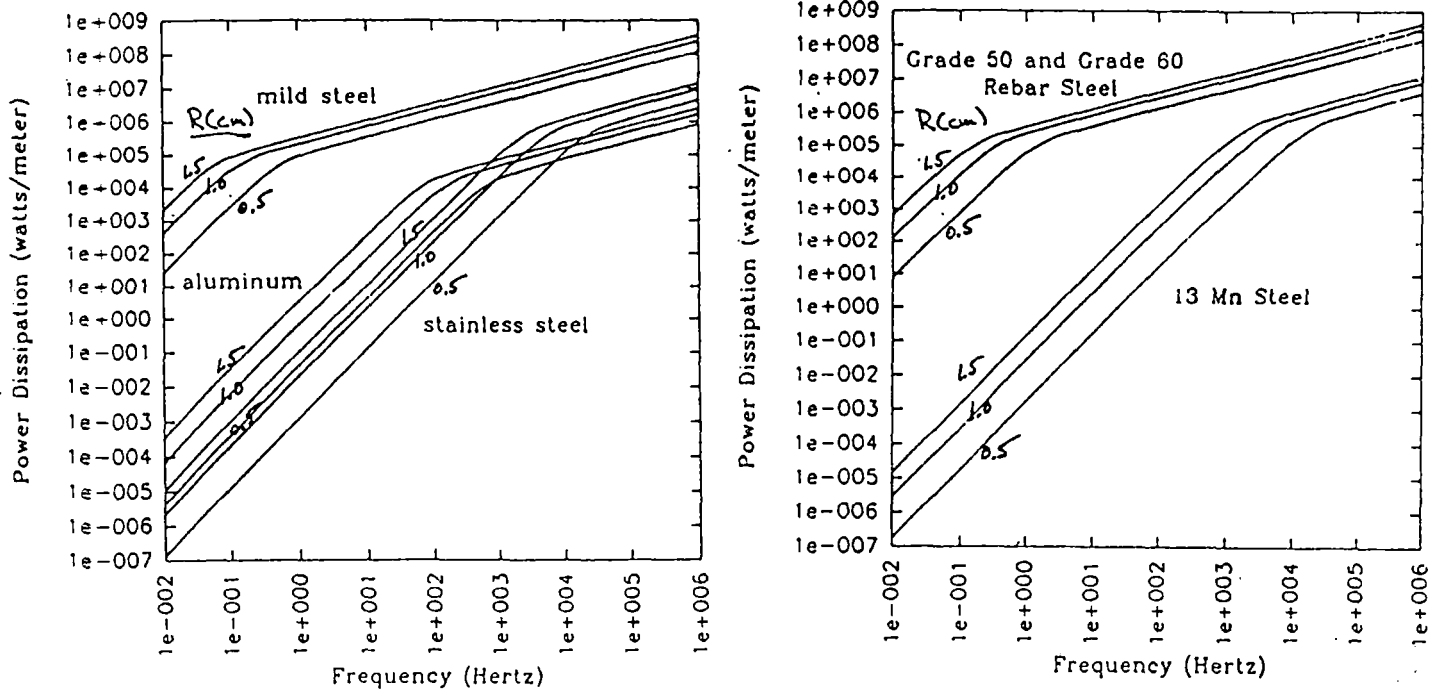


Figure 3: Dimensional dissipated power per unit length (watts/m) for an axial magnetic field versus frequency in Hertz for the materials in Table 1 for radius $R=0.5, 1.0,$ and 1.5 cm with peak magnetic field strength $|\mu_0 \hat{H}_o|=0.5$ tesla.

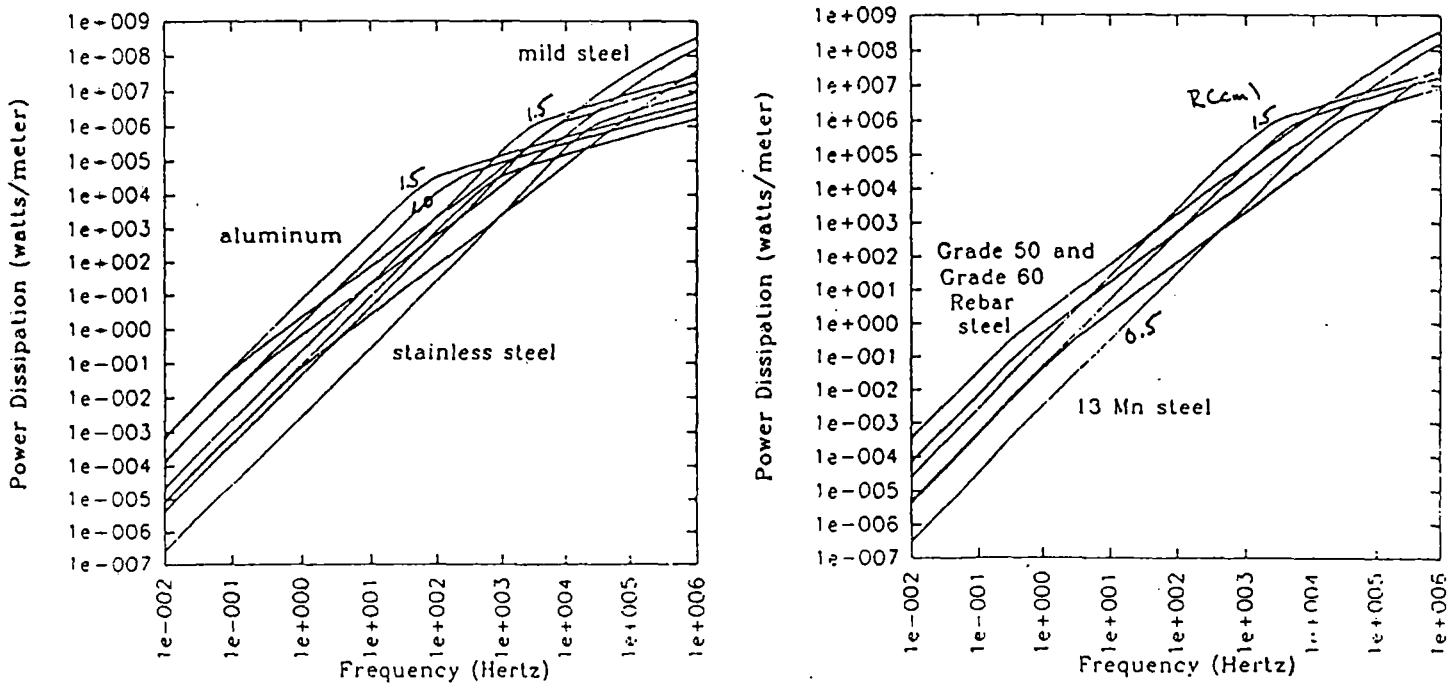


Figure 8: Dimensional dissipated power per unit length (watts/m) in a transverse magnetic field versus frequency in Hertz for the materials in Table 1 for radius $R=0.5, 1.0,$ and 1.5 cm and peak magnetic field strength $|\mu_0 \hat{H}_o|=0.5$ tesla.

Small skin depth limit

This case applies to mild steel for frequencies greater than about 0.5 Hz. It is also applicable to manganese steel for frequencies above about 2,000 Hz, but this is so high that it is probably not of major importance for rebars used in maglev applications.

For a given field strength and for non magnetic material the power loss for magnetic fields in the transverse direction is twice that for magnetic fields in the axial direction. The power loss is proportional to the square root of frequency, so it is greatest at higher frequencies.

For magnetic materials the transverse magnetic field produces substantially lower losses than the axial field. For both axial and transverse magnetic fields the power loss increases with increases in magnetic permeability μ .

Axial field

$$\langle P \rangle = \frac{\pi R |H_0|^2}{\sigma \delta} = \frac{\pi^3 R |B_0|^2}{\mu_0} \sqrt{\frac{\pi f \mu}{\sigma \mu_0}}$$

Transverse field

$$\langle P \rangle = \frac{\pi R |H_0|^2}{\sigma \delta} \left(\frac{2}{1 + \left(\frac{\mu \delta}{\mu_0 R} \right) + \frac{1}{2} \left(\frac{\mu \delta}{\mu_0 R} \right)^2} \right) = \frac{\pi^3 R |B_0|^2}{\mu_0} \sqrt{\frac{\pi f \mu}{\sigma \mu_0}} \left(\frac{2}{1 + \left(\frac{\mu \delta}{\mu_0 R} \right) + \frac{1}{2} \left(\frac{\mu \delta}{\mu_0 R} \right)^2} \right) \quad (1.5)$$

Large skin depth approximation

This case applies to Manganese steel at frequencies up to about 2,000 Hz and for mild steel at frequencies below about 0.5 Hz. For a given field strength and for non magnetic material the power loss in the transverse direction is twice that in the axial direction. The power loss is proportional to the square root of frequency, so it is greatest at higher frequencies.

For magnetic materials the transverse magnetic field produces substantially lower losses than the axial field. For both axial and transverse magnetic fields the power loss increases with increases in magnetic permeability μ .

Axial field

$$\langle P \rangle = \frac{\pi \mu_0 R^4 |H_0|^2}{4 \sigma \delta^4} = \frac{\pi \sigma R^4 |B_0|^2}{4 \mu_0} \left(\pi f \frac{\mu}{\mu_0} \right)^2$$

Transverse field

$$\langle P \rangle = \frac{\pi \mu_0 R^4 |H_0|^2}{2 \sigma \delta^4} \left(\frac{2 \mu_0}{\mu + \mu_0} \right)^2 = \frac{\pi \sigma R^4 |B_0|^2}{2 \mu_0} \left(\pi f \frac{\mu}{\mu_0} \right)^2 \left(\frac{2 \mu_0}{\mu + \mu_0} \right)^2$$

Effect of changes in rebar radius R

It is interesting to observe that for the small skin depth case the power loss only increases in proportion to R while the mechanical strength of the rebar varies as R^2 ; hence it is preferable to use fewer and larger rebars. On the other hand, for the large skin depth case the power loss varies inversely as R^4 so it is desirable to use many small rebars. This

suggests that a middle size rebar is the worst possible choice. Unfortunately, current construction practice does not allow one to use either very small or very large rebars, so it is not clear whether there is much to be gained by changing rebar size from what is current practice.

Mechanical force on a rebar in a magnetic field

The force is the sum of the magnetization force and the Lorentz Force, as explained in the previous section. Here we give approximations for the limiting conditions and graphs of typical results are shown on the next page.

Small skin depth approximation

This case applies to mild steel for frequencies above about 0.5 Hz. For a given field strength and nonmagnetic steel the power loss in the transverse direction is twice that in the axial direction. For nonmagnetic materials the force due to the transverse field is three times that due to the axial field, but for high μ materials the force due to the transverse field is much smaller.

Axial field

$$\langle f_y \rangle = -\frac{1}{2} \pi \mu R |H_0|^2 a$$

Transverse field

$$\langle f_y \rangle = -\frac{3}{2} \frac{\mu_0}{\mu} \pi \mu R |H_0|^2 a$$

Large skin depth approximation

This case applies to Manganese steel at frequencies up to 2000 Hz and for normal steel rebars at frequencies up to 0.5 Hz. Note that the loss increases as the fifth power of the radius R so smaller diameter rebars are preferable.

Axial field

$$\langle f_y \rangle = \frac{1}{2} \left[1 - \frac{\mu_0}{\mu} - \frac{R^4}{10\delta^4} \right] \pi \mu R |H_0|^2 a$$

Transverse field

$$\langle f_y \rangle = 3 \left(1 - \frac{\mu_0}{\mu} - \frac{R^4}{5\delta^4} \right) \left(\frac{\mu_0}{\mu + \mu_0} \right)^2 \pi \mu R |H_0|^2 a$$

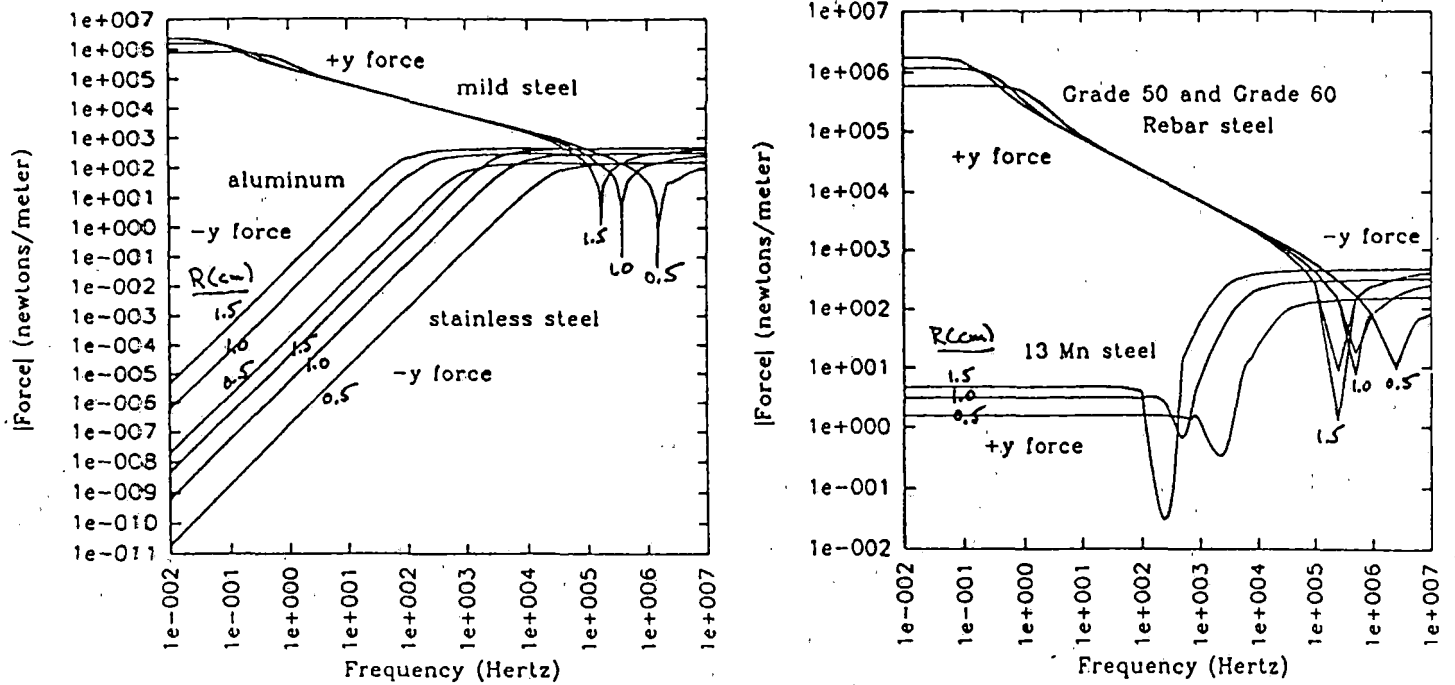


Figure 5: Total dimensional force per unit length (newtons/m) in the y direction versus frequency in Hertz due to the sum of Lorentz and magnetization forces from an axial magnetic field with a weak gradient, $a=0.1$, in the y direction for radius $R=0.5, 1.0$, and 1.5 cm with peak magnetic field strength of $|\mu_0 \hat{H}_0|=0.5$ tesla.

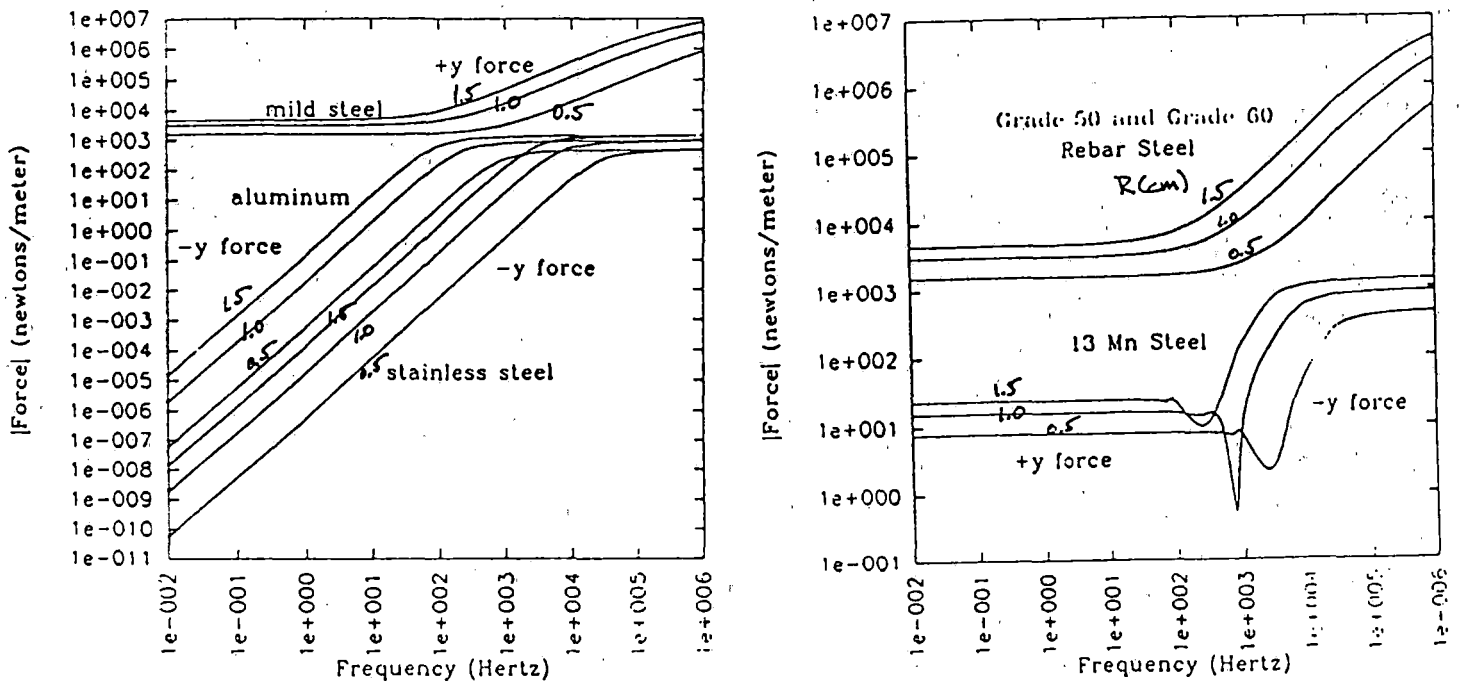


Figure 10: Total dimensional force per unit length (newtons/m) in the y direction versus frequency in Hertz due to the sum of Lorentz and magnetization forces from a transverse magnetic field with a weak gradient, $a=0.1$, in the y direction for radius $R=0.5, 1.0$, and 1.5 cm with peak magnetic field strength of $|\mu_0 \hat{H}_0|=0.5$ tesla.

Conclusions

The use of mild steel is unacceptable for fields as large as 0.5 Tesla because of the very large power loss. This loss is so high that it produces a significant drag on the vehicle and the rebars would get unacceptably hot. If the field is reduced to about 0.05 Tesla then the power loss is reduced by a factor of 100 and this is probably acceptable. In the case of mild steel these conclusions are based on the assumption of linear B-H characteristic and this is known to overestimate the power loss. Hence the numerical examples should be checked if one wishes to place rebars in locations where the field is more than about 0.05 Tesla.

The use of magnetic steel rebars in fields as high as 0.5 Tesla is also undesirable, though possible acceptable, because of the destabilizing magnetic force. This force will not damage the rebars or rebar/concrete bond, but it can adversely affect ride quality and guidance cost.

The use of nonmagnetic 13% manganese steel has dramatic advantages and can be used at field strengths up to about 0.5 Tesla. For nonmagnetic steel the linear analysis is quite accurate and we can predict losses with some confidence.

{This rest of the report is not finished and the reader is referred to Volume 2 where the results of detailed analytical and numerical analyses are presented. An outline is given below and the summary will be completed in the near future.}

1.3 Numerical analysis

Simple test cases and comparison with symbolic analysis
Analysis of Bechtel Foster-Miller guideways
Typical design examples

1.4 Summary of important conclusions

1.5 References

2 Analysis of effects of magnetic interactions on the guideway

2.1 Effects of interactions on the concrete

Magnetic force effects
Induced current heating effects
Corrosion effects

2.2 Effect of interactions on the vehicles

2.3 Summary of important conclusions

2.4 References

3 Design Guidelines

3.1 Limitations on use of rebars

3.2 Mitigation methods

Non magnetic steel rebars in selected regions
Increased spacing
Other alternatives

4 Recommended Test Procedures

4.1 Force tests

4.2 Thermal tests

5 Summary of Important Conclusions

DRAFT

**Investigation of the Deleterious Effects of
Electro-Magnetic Fields on Steel Rebar
Used in Guideways for EDS Maglev Systems**

**Volume 2
Reports on Key Issues**

January 27, 1995

**by
Dr. Richard D. Thornton
Dr. Markus Zahn
Mr. J. Richard Hale
Dr. Robert Pillsbury
Dr. Thanasis C. Triantafillou
Dr. Jerome J. Connor
Mr. Sanjay Srinivasan
Dr. H. A. Franklin
Ms. Janie Blanchard**

**And with help from other personnel at:
MIT Laboratory for Electromagnetic and Electronic Systems
MIT Plasma Fusion Center
MIT Department of Civil and Environmental Engineering
Bechtel Corporation**

**Project done with support from
DOT FRA**

**Mr. Michael Coltman
Contracting Officer's Technical Representative**

Bechtel

50 Beale Street
San Francisco, CA 94105-1895
Mailing address: P.O. Box 193965
San Francisco, CA 94119-3965

August 10, 1994

Professor Richard Thornton
(MIT/EECS, 10-005)
MIT
77 Massachusetts Avenue
Cambridge MA 02139

Dear Professor Thornton:

Enclosed is a revised copy of our final report for the "Investigation of the Deleterious Effects of Electromagnetic Fields on Steel Rebar used in Guideways for EDS Maglev Systems," dated August 8, 1994.

With this submission, we will be sending an invoice to MIT to close out the job, but will be willing to take your questions on this work following your return to MIT, per our earlier discussion. Since the total value of the subcontract is relatively small and the work is essentially completed, we are closing it out now to avoid numerous extraneous charges associated with keeping it open.

Sincerely,



J. P. Blanchard
Senior Scientist
Research & Development

w/enclosure

cc: Richard Hale (MIT/PFC, NW22-227)
Mark Zahn (MIT/EECS, 10-174)
Bob Pillbury (MIT/PFC, NW22-229)
Jerry Conner (MIT/CEE, 1-238)



Bechtel Corporation

**Investigation of the Deleterious Effects of
Electromagnetic Fields on Steel Rebar used in
Guideways for EDS Maglev Systems**

**Prepared by
Bechtel Corporation
Research & Development Department
San Francisco, CA 94119-3965**

**Revision 1
August 8, 1994**

**under subcontract # CC-S-467625
Massachusetts Institute of Technology
Cambridge, Massachusetts 02139-4307**

Table of Contents

Revision Summary	iii
Disclaimer	1
INTRODUCTION	2
TECHNICAL STUDIES	2
A. Corrosion in Maglev Guideway Structures	2
<i>Background</i>	2
<i>Factors Affecting the Corrosion of Steel in Concrete</i>	3
<i>The Effect of Electrical Current on Corrosion</i>	3
<i>Other Observations</i>	4
<i>Conclusion</i>	5
<i>References</i>	5
B. Non-Magnetic Steel in Maglev Guideway Structures	5
<i>References</i>	6
C. Rebar Bond in Maglev Guideway Structures	7
<i>Background</i>	7
<i>Reinforced Concrete Structures</i>	7
<i>Prestressed Concrete Structures</i>	8
<i>Bond of Rebar to Concrete</i>	9
<i>Concrete Cover over Rebar</i>	10
<i>Conclusions</i>	10
<i>References</i>	11
D. Analogous Systems:	
<i>Interference in Buried Pipelines Next to Electrical Power Lines</i>	11
<i>Background</i>	11
<i>Inductive Interference</i>	12
<i>Conductive Interference</i>	13
<i>Mitigation Techniques</i>	13
<i>Conclusions</i>	14
<i>References</i>	15
SUMMARY	15

Revision Summary
"Investigation of the Deleterious Effects of Electromagnetic Fields on Steel
Rebar used in Guideways for EDS Systems"

Revision 1 (dated August 8, 1994):

1. Corrosion in Maglev Guideway Structures

p. 4, under "Other Observations":

I^2R calculation of induced current density changed from 600 A/cm^2 to 60 A/cm^2 .

Note: this change does **not** alter the original conclusion that the induced currents are not expected to influence the deterioration of the beam via changes in corrosion rate of the rebar.

2. Non-Magnetic Steel in Maglev Guideway Structures

p. 6, table of material properties

Values for magnetic permeability and electrical resistivity corrected.

p. 7, references

Additional reference (Dietrich) added.

Note: Neither of these changes alters the original conclusions of this section.

DISCLAIMER OF WARRANTIES AND LIMITATION OF LIABILITIES

This report was prepared by Bechtel Corporation (Bechtel) as an account of work performed under contract to the Massachusetts Institute of Technology, sponsored by the Federal Railroad Administration (FRA). Neither Bechtel, nor any person acting on behalf of Bechtel:

(A) Makes any warranty or representation whatsoever, expressed or implied, (1) with respect to the use of any information, apparatus, method, process, or similar item disclosed in this report, including merchantability and fitness for a particular purpose, (2) that such use does not infringe on or interfere with privately owned rights, including any party's intellectual property, or (3) that this report is suitable to any particular user's circumstance; or

(B) Assumes responsibility for any damages or other liability whatsoever (including any consequential damages, even if the organization(s) named above or any representative thereof has been advised of the possibility of such damages) resulting from your selection of use of this report or any information, apparatus, method, process, or similar item disclosed in this report.

1. INTRODUCTION

Maglev vehicles, particularly those using superconductors for electrodynamic suspension (EDS), are expected to produce magnetic fields extending significant distances from the vehicle. Prior to this effort, the effects of these fields on the structural integrity of the guideway were unknown.

This report is a study of the following issues associated with potentially deleterious effects of electromagnetic fields on steel rebar used in guideways for EDS maglev systems:

- potential corrosion problems and methods of dealing with them
- potential for using manganese steel and other non-magnetic rebars
- issues related to structural failure mechanisms, such as high cycle loads, due to EM field interactions
- examples from analogous systems

2. TECHNICAL STUDIES

A. CORROSION IN MAGLEV GUIDEWAY STRUCTURES

1. Background

The subject of this discussion is whether the electrical currents induced in steel reinforcement by the passing of a maglev vehicle over a reinforced concrete beam can affect the deterioration of the beam. This discussion will be limited to "corrosion" issues, that is, chemical and electrochemical reactions. Resistance heating and other electrical issues will be discussed elsewhere.

The deterioration of reinforced concrete can occur by a number of mechanisms. Broadly these mechanisms can be divided into direct attack of the cement binder or corrosion of the reinforcing bar.

Direct attack of the cement paste occurs by reactions of compounds such as sulfates and carbon dioxide with constituents in the cement. The result can be local swelling and cracking or the development of sponginess. These are surface reactions which can proceed through the structure. They are the result of interaction with the environment and are controlled by the selection of the type of cement and surface protection. They are not electrochemical processes and are not influenced by electrical current; therefore, they will not be discussed further.

The products formed when steel corrodes have a larger volume than steel; as a result, corrosion of steel rebar in concrete produces tensile stresses in the concrete. Concrete has low tensile strength; therefore, corrosion of the rebar causes spalling of the concrete which can lead to failure of the structure. Corrosion of the steel is an electrochemical process which is influenced by electrical current.

It is clear that DC can affect the corrosion behavior of steel reinforcement in concrete. In an early evaluation of pre-stressed concrete sleepers for electrical railways, it was shown that connecting the steel to the anode of a battery caused spalling of a concrete sleeper buried in soil [1]. Furthermore, cathodic protection has been used to protect rebar from corrosion under conditions of chloride contamination that are discussed below. Whether the electrical induced by the maglev vehicle will have a significant effect on the corrosion of the rebar is the subject of this discussion. It is our understanding that these currents will be AC.

2. Factors Affecting the Corrosion of Steel in Concrete

For iron or steel to corrode in concrete, there must be water and a corrosive agent. In damp concrete, the corrosive agent is oxygen dissolved in the water. For corrosion to occur, the oxygen and water must be present at the rebar surface; the water can reach the steel surface either through cracks and voids in the concrete or by permeating through the naturally existing pores in the concrete. Since no corrosion can occur without water, the most common method of corrosion control for reinforced concrete is to provide sufficient concrete (cover) between the surface and the rebar to retard the permeation of water and other contaminants to the rebar. Coatings and sealants can provide similar protection.

As water permeates through the concrete, it becomes very alkaline because it leaches lime from the cement. Normally the environment is so alkaline that the steel is passive; that is, it does not corrode because a protective film forms on it. However, if chlorides are present, the passivity breaks down, and corrosion begins. The lowest concentration of chlorides that it expected to cause breakdown of passivity is 0.025 percent by weight of concrete.

Chlorides can come from the water used to mix the concrete, from impurities or contaminants in the sand or coarse aggregate, or from accelerators such as calcium chloride used in the curing process. These sources of chlorides can be controlled by the proper selection and control of raw materials.

A more troublesome source of chlorides is the environment to which concrete can be exposed. Sea water, chloride containing soils, and deicing salts are the most common sources. It must be emphasized that corrosion as a result of chloride contamination will in the absence of electrical currents. This type of corrosion must be considered in the design of any reinforced concrete structure.

3. The Effect of Electric Current on Corrosion

With the exception of the precious metals such as gold, all metals are thermodynamically unstable with respect to their environment. They should react the

oxygen in the air to return to their ores. Fortunately, the rate of this reaction is usually slow. Like most chemical processes, corrosion is an activated rate process, and the rate of corrosion can be related to electrical current through Faraday's law.

The electrochemical aspects of corrosion are the subject of numerous texts and reviews [2]. For purposes of this discussion, it is sufficient to note the equivalence of corrosion rate and electric current and that the corrosion reaction is composed of two partial reactions. The anodic reaction is the dissolution or oxidation of the metal. The cathodic reaction is the reduction of the corrodant, *e.g.* oxygen. The currents representing each reaction are equal and opposite in sign

Although the effects of direct current on corrosion are well understood the effects of AC are less clear. Since the currents in each direction are equal, one might expect that the net effect would be zero. However, this assumption would require that the reactions be perfectly reversible which they are not. Since conduction in electrochemical reactions is by ions and not electrons, one might also expect that any affect might be frequency dependent. At some point the rate of current reversal would become too fast to allow the ions to react.

Jones [3] performed a series of experiments in which he imposed AC and DC currents on steel coupons on which he measured weight loss. His results indicated that an AC current of 30 mA/cm² increased the corrosion rate of steel in a de-aerated sodium chloride solution by factor of five over that of samples without the imposed current. However, when a similar current was imposed on samples in an aerated solution, there was no effect on the corrosion rates. A DC current of 15 mA/cm² increased the corrosion rate in the de-aerated solution by several thousand fold. The DC current density of 15 mA/cm² was chosen to equal the anodic half of the 30 mA/cm².

Several conclusions can be drawn from these experiments. The effect of AC on corrosion rate is small compared with that of DC. From polarization measurements made in conjunction with the weight loss experiments, it appears that effect that AC has occurs when the corrosion reaction is controlled by activation polarization or charge transfer. When the corrosion reaction is controlled by diffusion of a reactive species, *e. g.* oxygen, the effect of AC is negligible. Since the corrosion of reinforcing steel in concrete is controlled by the diffusion of oxygen to the steel, it is unlikely that AC currents induced into the rebar by the maglev vehicle will affect the corrosion behavior of the rebar.

4. Other Observations

In analyzing whether currents, AC or DC, flowing in the rebar will affect corrosion behavior, it must be remembered that to cause corrosion the current must leave the rebar. It must flow through the environment to ground or another structure. The electrical engineers assure us that the AC induced in the rebar by the maglev vehicle will never leave the rebar.

In a preliminary calculation that MIT [4] performed in estimating the amount that the induced currents would raise the temperature of a rebar, they indicated that 12 watts could be induced into a 16 mm rebar. Based on the resistivity of the typical rebar steel, an I²R calculation suggests a current density of nearly 60 A/cm². This current density is

well above the level that has been reported to influence the behavior of cathodically protected pipelines [5]. However, the duration of this current is very short. It causes a temperature rise of only a small fraction of a degree K. Thus the total induced energy is small, and the effect integrated over time should be small even if the current could flow to ground.

5. Conclusion

The currents induced by a maglev vehicle into the rebar in a reinforced concrete beam are not expected to influence the deterioration of the beam by affecting the corrosion behavior of the rebar.

This conclusion is based on these premises:

- a. The induced currents are AC, of short duration and cannot leave the rebar.
- b. The corrosion of steel rebar in concrete is controlled by diffusion of oxygen to the rebar, not by charge transfer. Therefore, even if the AC current could accelerate the anodic reaction, there is not oxygen available to support increased anodic activity.

6. References for *Corrosion in Maglev Guideway*

1. Railway Technical Research Institute of Japan, "Pre-Stressed Concrete Sleepers Tested for Service on Electrified Railways," *Corrosion*, Vol. 13, August 1957. p. 120.
2. See, for example, R. F. Steigerwald, "The Electrochemistry of Corrosion," *Corrosion*, Vol. 24, Jan. 1967.
3. D. A. Jones, "Effect of Alternating Current on the Corrosion of Low Alloy and Carbon Steels," *Corrosion*, Vol. 34, pp. 428-433, Dec. 1978.
4. FRA Maglev Projects Review, MIT, June 22, 1994.
5. W. Prinz, "AC-Induced Corrosion in Cathodically Protected Pipelines"

B. NON-MAGNETIC STEEL IN MAGLEV GUIDEWAY STRUCTURES

There may be advantages to using non-magnetic reinforcement in some of the reinforced concrete structures in a maglev installation. Since some of the non-magnetic materials such as stainless steels and reinforced plastics are quite expensive compared to conventional rebar, the question has been raised as to whether a lower cost material is available. Austenitic manganese steels are commodity products that have been used for many years for wear parts in the railway industry. This section presents a brief discussion of these materials.

An extensive summary of the properties of non-magnetic manganese steels is available [1]. The following information, believed pertinent to the use of these steels for reinforcing bar in a maglev project, was taken from this summary.

1. The material that should be considered for the non-magnetic rebars is a 13% manganese, 1.2% carbon steel. This is a standard composition for cast materials, and it has been made as wrought materials although it is not a standard. There should be no problem in obtaining the alloy as rebars for a large project such as a maglev installation.

No inquiries have been made to steel mills about the cost of the material, but it is estimated that it would cost about twice as much as ordinary steel rebars. Non-magnetic stainless steel rebars would cost 5 to 6 times as much. Although manganese is more costly than iron, it is much less expensive than the nickel used to produce conventional non-magnetic stainless steels.

2. The following table presents comparative properties of a 13 percent manganese steel and two grades of conventional steel rebar:

Steel	Yield Strength (MPa)	Tensile Strength (MPa)	Magnetic Permeability	Thermal Expansion $10^{-6}/^{\circ}\text{K}$	Electrical Resistivity $\text{n}\Omega\text{-m}$
13 Mn	360	825	1.01	18.01	711
Grade 50 Rebar	350	550	3800	11.1	224
Grade 60 Rebar	400	600	3800	11.1	230

3. The austenitic manganese steels have essentially the same corrosion resistance as the carbon steels used for rebar. No galvanic corrosion effects are expected with a combination of austenitic manganese steels and ordinary rebars. For many years, austenitic manganese steel switch frogs have been connected to ordinary steels rails exposed to the atmosphere in railroads and other transit systems. Galvanic corrosion has never been a problem.

The Japanese have investigated the use of high manganese steels for use as reinforcement in concrete subjected to high magnetic fields [2]. They are also considering it for use in maglev applications [3].

In summary, high manganese steels appear to be an attractive alternative to conventional rebar when non-magnetic materials are needed.

References for Non-Magnetic Steel in Maglev Guideway Structures

1. D. K. Subramanyam, A. E. Swansiger, and H. S. Avery, "Austenitic Manganese Steels," *Metals Handbook, 10th Edition*, Vol. 1, ASM International, 1990, pp. 822-840.
2. T. Okuda, "Possibility to Reinforce Concrete with Non-Magnetic High Manganese Steel Bar," *Quarterly Progress Reports, RTRI, JNR*, Vol. 22, No. 1, 1981.

3. Y. Sato, A. Matsuura and S. Miura, "Guideway for Maglev," *Quarterly Progress Reports,, RTRI, JNR*, Vol. 27 No. 2, 1986.
4. D. W. Dietrich, "Magnetically Soft Materials," *Metals Handbook*, 10th Edition, Vol. 2, p. 765.

C. REBAR BOND IN MAGLEV GUIDEWAY STRUCTURES

1. Background

Structural systems made from concrete fall generally into two categories: reinforced concrete and prestressed concrete components. Concrete first became used for major structural applications when the lack of tensile strength of the plain concrete was successfully compensated by the addition of iron bars which provided the tensile resistance for flexural members such as beams. In the late 1800's the technique of applying a prestress to a concrete member by means of long threaded steel rods was tried with the idea of creating a dominant compressive stress in the system that would negate tensile stresses developed by the application of external loads. Various associated technical issues had to be solved before prestressed concrete became viable as a reliable structural system. These systems for concrete structures are discussed in the following sections with regard to the issue of bond between the embedded steel (rebar) and the concrete. In the context of the following discussion, the Bechtel maglev guideway design is a fully prestressed concrete system and is not classified as a reinforced concrete system.

The concern of this study is that the rebar bond in maglev guideway structures might be affected by the repeated passage of large magnetic fields giving rise to a fatigue effect. The study of fatigue identifies two classes of action: low cycle fatigue which has a few cycles of very large force such as in wind or seismic events; and high cycle fatigue which has very many cycles of a small force. The potential bond fatigue in a guideway would be a high cycle fatigue event and furthermore would be a small cyclic load imposed on a large static load. In particular, we can expect the static load to be dominant and the applied cyclic load to have two components: one is the cyclic, non-reversing axial load in any axial rebar due to passage of the train; the second is the cyclic, non-reversing transverse force on that rebar due to passing of a series of vehicle magnets. In each case the important feature is the non-reversing action of these forces which leads to the least severe, hence most tenable, fatigue situation.

2. Reinforced Concrete Structures

The steel rods (rebar) embedded in the concrete perform the function of supplying tensile resistance which is lacking in the concrete itself. Accordingly, the member section has a compressive stress area of concrete balanced by tensile forces in the embedded steel rods. Since the rebar is placed in the member before the concrete is placed, the steel becomes stressed by the subsequent deflection of the member, due to external loads. The concrete is bonded to the steel and extensive tests have been made and reported in the literature to quantify the nature of this bonded contact. The rebar bond is indirectly specified in reinforced concrete design codes since it must be accounted for in the design

of a concrete member. When external loads are applied the steel will undergo tensile strains as will the attached (bonded) concrete. Since concrete has a very limited ability to carry tension then it will crack. It is well known that reinforced concrete members will naturally be finely cracked in the process of carrying loads. This phenomenon decreases the available concrete section, increases deflections, reduces stiffness, and increases the risk of corrosion of the embedded steel in difficult environments. We should note that the majority of concrete structures are reinforced and that the above behaviors are accounted for in the engineering design process. Most buildings, for example, provide a sheltered environment for the concrete beams, slabs and columns. A quite different structural performance occurs for the prestressed concrete discussed next.

3. Prestressed Concrete Structures

The other approach to dealing with the lack of concrete tensile strength is to simply provide a preliminary compressive stress field and not allow the concrete section to experience tensile stresses upon the application of external loads. The successful execution of this idea has required the development of suitable high strength steel wires and rods as well as high quality concrete. This approach has led to two kinds of prestressing methods: pretensioning and post-tensioning the concrete members. Both pre- and post-tensioning are incorporated in the Bechtel guideway design.

Pretensioning is usually done by stretching the steel wires or strand between two anchorages at each end of the casting beds. Formwork is erected around the wires, concrete is placed and cured; then, after removal of the formwork, the wires, still under high tension, are released from the anchorages. The wires are bonded to the concrete by virtue of the embedment and the high tension in the steel is transferred to the concrete, putting the member into compression, through the bond at the end regions of the wires. This method is used to form structural units like concrete planks, roof members, and long concrete piles. Concrete bond is important for this kind of prestressing.

Post-tensioning is used almost exclusively for major structural members such as bridge girders. In this approach the formwork is assembled for the concrete member and ducts are emplaced through which steel wires or strands are passed. The concrete is placed and cured, the formwork is removed, and when the concrete has gained sufficient strength the steel wires are stretched to high tension and anchored directly to the concrete at each end of the member. The large tension in the steel strand is therefore passed to the concrete girder externally through the end anchor plates, putting the girder into compression. The bond of concrete to steel is simply not a factor in the structural performance of an end-anchored prestressed concrete member. Another advantage of this approach is that the steel strand can be de-tensioned and re-tensioned during the life of the member.

Additional rebar will usually be found in prestressed members. Rebar spirals are placed around the steel strand duct, close to the anchors, in the end anchorage zones to resist the transverse bursting tensile stresses that occur below the anchor plates. Other rebar placement might occur depending on the ratio of the live load to the dead load. If the design requires prestress of such magnitude that the preload camber is large and tensile stresses are caused in the opposite direction to the live loading, then longitudinal rebar is designed into the section to resist that tension. In addition the technique of partial prestressing is frequently invoked in which sufficient prestress is provided for

section compression before working loads are applied, but allows some tension under the external loads. Thus some axial rebar is included to handle that tension. This is a matter of relative weights of the maglev vehicle and the guideway when detailed design is developed. Partial prestressing design has most significance in increasing the ultimate strength of the member in most cases. Transverse rebar is placed in prestressed members to form a cage which provides the required ultimate shear strength for the section. It also provides lateral confinement for the axial rebar and may also be used to help locate the tendon ducts during fabrication.

4. Bond of Rebar to Concrete.

The previous discussion of concrete structural systems shows that bond between concrete and steel rebar is very important for reinforced concrete members and pretensioned members, but has no significance for fully prestressed members and is only important for the additional rebar in any prestressed member. The Bechtel maglev guideway design is for a prestressed concrete member. Hence this gives the context for considerations of the bond between rebar and concrete. The same considerations hold for non-metallic reinforcements in concrete systems.

Bond, or the attachment of concrete to the rebar, is a surface phenomenon and the strength of the bond is heavily influenced by the condition of the rebar surface. Good practice requires the elimination of rust, corrosion, oil or dirt from the rebar before placing the concrete. Bond is measured by pulling an embedded rebar from a concrete section. The resistance to pull-out (the bond strength) is increased by lugs rolled onto the surface of the rebar used in standard practice. Hence the anchorage bond resistance is partly adhesion, partly frictional and partly mechanical in origins. Another measure of bond is derived from a test where a steel rod is surrounded by a concrete cylindrical jacket; then the steel is tensioned. The relationship between crack spacing and steel tension is used to investigate flexural bond. All of this is academic in that modern design codes no longer discuss bond stress levels but instead specify development lengths for rebar which are functions of steel yield, concrete strength, and bar sizes.

Whereas concrete design is concerned about the transfer of tension from the concrete to the rebar through the bond mechanism, and standard design rules are provided for this, there is no information available about the effects on bond by a transverse force developed in the rebar, say, by an applied magnetic field. Both high cycle fatigue and low cycle fatigue have been investigated in studies of rebar bond and to develop design rules. Whereas low-cycle fatigue is characterized by a few excursions (say less than 100) of high stresses into the inelastic range, the high cycle fatigue is characterized by a very large number of cycles in the working stress range. Work at MIT indicates up to 6,000,000 magnetic force pulses per year on the rebar in a guideway for the Bechtel concept under maximum traffic conditions.

Design approaches are available in various international codes for high cycle fatigue. But it is noteworthy that since tests have shown that either the concrete or steel will fail in fatigue before the bond fatigue limit is reached, then most design equations refer to the stress range in the concrete or steel rather than to any bond stress limit. Furthermore, it is important to note that these design rules are directed to the design of reinforced concrete members and that a far less serious situation is presented in the case of partially prestressed members, and hardly at all by fully prestressed members. Most of

the rebar in the Bechtel design is non-magnetic fiber reinforced plastic (FRP) placed in the regions of highest magnetic interaction. Only some of this rebar is axial, and, if replaced by steel rebar, would likely be subject to bond stress cycling. Most of the rebar is transverse hoop rebar and its stress state is not critical. Even if it were replaced by steel rebar, the worst effect would probably be increased magnetic drag on the vehicle.

MIT studies have shown that the order of magnitude of the maximum transverse force on a steel rebar due to the passing magnets is probably no more than 30 psi over the diametrical plane. This would be a cyclic variation imposed on a background bond stress level (due to live load and dead load) which would give a stress range of only 30 psi. Fatigue susceptibility is sensitive to the stress range, and with a non-reversing stress, as in this case, very little effect would be expected in these prestressed girders.

5. Concrete Cover Over Rebar

Concrete cover required to provide protection to the concrete is specified in concrete design codes. In U.S. practice this is based on the guidelines of ACI-318 Section 7. Concrete cover is measured from the concrete surface exposed to the environment to the outermost surface of the embedded steel. Cover is specified by environment, sometimes by size of bars, and by member design type. For example, in a prestressed concrete beam exposed to weather or soils the minimum cover is specified as 1-1/2 inches (38 mm). [ACI-318 Sect. 7.7.3.1(b)]. This is to be increased by 50% when the member design causes certain tensile stresses to be exceeded (which may happen in the case of partially prestressed members). In the extreme case of a corrosive environment, which is a worse classification than marine exposure, a minimum cover of 2-1/2 inches (64 mm) is recommended. In the case of the Bechtel guideway, a nominal cover of 30 mm was specified because this design uses fiberglass reinforced plastic (FRP) rebar. These outer non-magnetic rebar eliminate corrosion as a design issue.

Note that durability in concrete members is not just a function of concrete cover. The first consideration is the water-cementitious materials ratio and the concrete strength which are basic parameters of the mix design. Other factors are the use of pozzolans; quality of aggregates; exposure conditions to weather, salts and chemicals; and conditions of placement and curing. In recent years the research on concrete durability has identified concrete permeability as a fundamental factor in the resistance of reinforced members. Increasing the impermeability provides increased corrosion resistance. If the designer is forced to reduce the cover because of geometric constraints, then manipulation of the concrete mix design and selection of coated rebar provides options. However, the use of prestressed concrete members for the guideway makes durability less of an issue since the high strength required and the elimination of cracks work to the benefit of these members.

6. Conclusions

The design concern for reduction of bond under high cycle fatigue loading from passing magnets is only relevant for those steel rebar incorporated in a guideway for flexure as well as for any pretension strands (they use bond for force transfer). Those rebar augment the section behavior under service loads, are usually in the top of the girder,

and in the Bechtel design are of non-magnetic FRP and would provide no fatigue problem. Prestressed girders always have a mesh of transverse hoop rebar but whether of steel or FRP their bond condition is not critical to the flexural performance of the guideway. These are of FRP in the Bechtel design.

Rules are presently available for the design of reinforced concrete sections under high cycle fatigue loads which can be adopted for the prestressed guideway. These rules, in various international codes as well as the ACI, deal with the concrete or steel stress limits since bond is not a problem in structural fatigue. The design stress ranges, typically using 1,000,000 cycles, show substantial allowable stress levels in the concrete or steel far exceeding the 30 psi stress range caused by the magnetic fields. In light of this it seems the magnetic effects on the guideway rebar are not likely to create a problem for rebar bond. The transverse forces due to passing magnets will need to be assessed in magnitude relative to the specific steel rebar locations in order to determine if an additional design factor should be invoked to modify the design of any embedded steel.

6. References for Rebar Bond in Maglev Guideway Structures

1. ACI 408.2R-92 "State-of-the-Art Report on Bond Under Cyclic Loads", ACI Committee 408, American Concrete Institute, Detroit MI, 1992.
2. ACI 215R-92 "Considerations for Design of Concrete Structures Subjected to Fatigue Loading", ACI Committee 215, American Concrete Institute, Detroit MI, 1992.
3. T. Y. Lin, Ned H. Burns, "Design of Prestressed Concrete Structures", 3rd Ed., John Wiley & Sons, 1981.
4. E. G. Nawy, "Reinforced Concrete: A Fundamental Approach", Prentice-Hall, 1985.
5. R. Karmacharya, M. Zahn, "Power Dissipation and Magnetic Forces on MAGLEV Rebars", MIT Laboratory for Electromagnetic and Electronic Systems, Cambridge MA, June 1994.
6. T. C. Triantafillou, "Electromagnetic Effects on Rebars in MAGLEV Guideways", MIT Cambridge MA, June 1994.
7. ACI Manual of Concrete Practice, American Concrete Institute, Detroit MI, 1993.

D. ANALOGOUS SYSTEMS:

INTERFERENCE IN BURIED PIPELINES NEXT TO ELECTRICAL POWER LINES

1. Background

Constraints placed by environmental and regulatory authorities on pipeline right-of-way acquisition have forced construction of many pipelines in electrical power transmission line right-of-ways. Pipelines sharing a ROW with power lines may be subject to electrical interference, due to both inductive and conductive effects. Magnetic induction acts along

the length of pipeline approximately parallel to the power line and can result in significant pipeline potentials even at large separation distances. Conductive interference due to currents flowing in the soil is of special significance at points in the vicinity of transmission line structures that may inject large currents into the soil during upset conditions. The effects of power system interference on pipelines are due to the relative voltage differences created between the pipeline metal and local soil.

Power system interference on pipeline can result in damage to the pipeline and its protective coating. Excessive coating stress voltage can result in degradation of the coating material, leading to accelerated corrosion.

The initial efforts to analyze power line effects on gas pipelines were concentrated on modeling the inductive coupling between the power line and the pipeline during normal power system load conditions. The paper by Carson [1] outlines the fundamental theory of coupling between parallel conductors in the presence of a uniform half space conductive medium, earth. Sunde [2] expands Carson's work to include effect of point sources of current on conductors. Sunde's work also investigates the effects of earth layering on the inductive coupling problem. Recently, studies undertaken by EPRI/AGA [3] have yielded computerized techniques for the analysis of power load current coupling to gas pipelines.

The combined inductive and conductive effects of fault current on pipelines are influenced by a multitude of physical parameters. Sunde [3] provided the groundwork for this complicated analysis. Experimental investigation of combined inductive and conductive interference on conductors was performed by Favez [4]. There are a number of published analytical works describing the theory of conductive coupling between point sources and pipelines. Prominent among these are AGA's research projects on HVDC effects on pipelines [5,6]. Dawalibi et al. [7] introduced the generalized theory of conductive coupling between power installations and buried metallic structures and later expanded it to include effects on coated conductors [8]. The issue of power line fault current coupling to nearby natural gas pipelines is discussed comprehensively in the EPRI/AGA Report [9] by the same name. The report provides analysis tools as well as graphical techniques for estimating the magnitude of electrical interference.

The computerized modeling of pipelines in complex power transmission line corridors can be performed using ECCAPP, a software developed by EPRI. This powerful program can be used to analyze the combined effects of inductive and conductive coupling and can be used to calculate fault currents in the power line and ground wires based on a physical description of the system.

2. Inductive Interference

Inductive coupling is the dominant interference mechanism under normal power line conditions. The induced potentials on unmitigated pipelines are especially high at power line transposition locations or at locations where the pipeline and power line veer away from each other. The presence of pipeline coating with high electrical resistance causes the induced steady-state pipeline potentials to be more severe, however coating may be required for cathodic protection of the pipeline.

During single-phase-to-ground conditions on the power line such as when a single energized phase wire is shorted to a transmission line structure, the intense magnetic field caused by the large current flowing in the faulted wire can cause extremely high induced voltage on unmitigated pipelines.

3. Conductive Interference

When a single-phase-to-ground fault occurs at a power line structure, the large currents injected into the soil raises the local soil potential. The pipeline in the vicinity of the structure will remain at a relatively lower potential due to the resistance of the coating and grounding at points distant from the fault locations. The potential rise will be particularly small in the case of a pipeline with high-resistance coating. In such cases the surrounding soil will be at a relatively high potential with respect to the pipeline steel potential.

The magnitude of the conductive interference is a function of several factors:

- The magnitude of the current injected into the ground, which determines the potential rise of the transmission line structure grounding system.
- The separation between the faulted structure and the pipeline.
- Size of the transmission structure grounding system. The decreased in soil potentials with distance is steeper for smaller grounding system than for large grounding system.
- The rate of potential decay away from a faulted structure depends on the soil structure and layering characteristics.
- Pipeline coating resistance plays a major role in determining the interference level on the pipeline. If the coating resistance is small, the potential rise in the pipeline is high and correspondingly the local earth potential diminishes. The potential difference between the earth and the pipe is consequently reduced.

Unless the pipeline is perpendicular to the power line, it will be simultaneously subjected to inductive and conductive interference. In most cases, the change in pipeline potential due to inductive interference will be opposite in sign to the change in earth potential due to conduction. This results in a substantial increase in the coating stress voltage.

4. Mitigation Techniques

The AC mitigation system must ensure that pipeline coating stress voltages remain within acceptable limits to prevent damage to the coating or even to the pipeline steel. Coating damage can occur at voltages on the order of 1000-2000 V for bitumen coated pipelines and 3000-5000 V for fusion bonded epoxy coatings. In addition the mitigation system should ensure acceptable touch voltage at exposed pipeline sites, such as valves and metering stations. Excessive touch voltages due to conductive interference can be reduced by lowering earth surface potentials in the vicinity of the pipeline or by raising

the pipeline potential near the faulted structure. The effective mitigation systems perform both these actions simultaneously.

a. Cancellation Wires

The technique consists of burying long wires parallel to the power transmission line, often on the side opposite to the pipeline. The wire is subjected to interference from the transmission line. However, by carefully locating each wire, the voltages induced on the wire can be out-of-phase with the voltage in the pipeline. Connecting one end of the wire to the pipe causes the out-of-phase voltages to cancel out each other. The other end of the wire is left free.

This technique for AC mitigation suffers from several serious drawbacks:

- Only induced interferences are mitigated by this method.
- The free end transports excessive potential to locations where such potentials are not expected, posing a safety hazard.
- The cancellation wire also increases exposure of the pipeline to direct energization from a fallen power line or during fault conditions from unknown grounding system components.

b. Gradient Control Wires

This is a relatively new interference control technique. Gradient control wires consist of one or more bare zinc conductors buried parallel and near the pipeline and connected at regular intervals to it. In the case of inductive interference, gradient control wires act as additional grounding for the pipeline, lowering the pipeline induced potentials and correspondingly increasing the local earth potential. This results in dramatically reduced touch and coating stress voltages.

In a conductive interference situation, gradient control wires dampen the soil potential rise in the neighborhood of the pipe while simultaneously increasing the pipe potential. Again the potential difference between the earth and the pipe is reduced causing smaller coating stress voltages.

The gradient control wires are made of zinc and consequently act as sacrificial anodes providing cathodic protection to the segments of pipe to which they are connected.

5. Conclusions

The current flowing in transmission lines in the vicinity of buried metallic conductors (pipelines) causes interference in the conductors. The magnitude of this interference is heightened by long, parallel exposures and power fault conditions. In such cases, high currents and voltages may be induced along the conductors' length. Energy may also flow directly from power installations to buried conductors through conductive paths (soil). This direct flow of energy can cause severe voltage stresses on the pipeline and its coating.

The interference caused on the pipeline due to the transmission line can be mitigated using gradient control wires. These wires (zinc anodes) reduce the potential difference between the pipeline and the surrounding soil thereby reducing stress voltages.

The analysis of power line coupling to pipelines can be performed using sophisticated computer techniques. These programs can also be utilized to evaluate the various mitigation techniques.

6. References for Analogies with Other Systems

1. J.R.Carson, " Wave Propagation in overhead wires with ground return", Bell System Technical Journal, Volume 5, October 1926, pp. 539-554.
2. E.D. Sunde, " Earth conduction effects on transmission systems", 2nd edition, Dover Publications, New York, 1968.
3. "Power line - Induced AC potential on natural gas pipelines for complex right-of-way configurations", EPRI/AGA Project 742-2, EL-3106/PR-151-127, May/November, 1983.
4. B. Favez, J.G. Gougeuil, "Contribution to studies on problems resulting from the proximity of power lines with underground metal lines", CIGRE, 1966, Paper No. 336.
5. "Analysis of the effects of high-voltage direct-current transmission systems on buried pipelines", American Gas Association Project PR-3-41, Catalog No. 30500, January 1967.
6. "Earth current effects on buried pipelines - computer programs and mathematical models for analysis of effects", American Gas Association on Research Project, Catalog No. L30570, 1970.
7. F.Dawalibi, D. Mukhedkar, "Transferred earth potentials in power systems", IEEE Transactions, Vol. PAS-97, No.1, January/February 1978, PP. 90-101.
8. F. Dawalibi, " Ground fault current distribution between soil and neutral conductors", IEEE Transactions, Volume PAS-99, March/April 1980, pp. 452-461.
9. "Power line fault current coupling to nearby natural gas pipelines - Volume 1: Analytic methods and graphical techniques", American Gas Association Research Project PR176-510, Catalog No. L51537, 1987.

3. SUMMARY

From the information provided by MIT regarding current induced in the rebar, we described whether, in our best estimate, these currents are likely to have any effect on the corrosion of the rebar based on the best available information about the conditions under which corrosion of rebar might be expected and whether such conditions are

credible in a maglev installation. We next evaluated whether deterioration of the rebar/concrete bond can be expected to occur based on the static and cyclic forces that MIT estimates the magnetic fields will produce on the rebar. In addition, we evaluated whether deterioration of the rebar/concrete bond can be expected given the expected temperature rises in the rebar due to induced currents, as calculated by MIT. Finally, we identified relevant analogous systems for which data might exist to support our conclusions.

Based on this work, we came to the following conclusions:

1. The currents induced by a maglev vehicle into the rebar in a reinforced concrete beam are not expected to influence the deterioration of the beam by affecting the corrosion behavior of the rebar.
2. High manganese steels appear to be an attractive alternative to conventional rebar when non-magnetic materials are needed.
3. The design concern about reduction of bond under high cycle fatigue loading from passing magnets is only relevant for those steel rebar incorporated in a guideway for flexure as well as for any pretension strands (they use bond for force transfer). Those rebar augment the section behavior under service loads, are usually in the top of the girder, and in the Bechtel design are of non-magnetic FRP and would provide no fatigue problem. Prestressed girders always have a mesh of transverse hoop rebar but whether of steel or FRP their bond condition is not critical to the flexural performance of the guideway. These are of FRP in the Bechtel design.
4. Rules are presently available for the design of reinforced concrete sections under high cycle fatigue loads which can be adopted for the prestressed guideway. These rules, in various international codes as well as the ACI, deal with the concrete or steel stress limits since bond is not a problem in structural fatigue. The design stress ranges, typically using 1,000,000 cycles, show substantial allowable stress levels in the concrete or steel far exceeding the 30 psi stress range caused by the magnetic fields. In light of this it seems the magnetic effects on the guideway rebar are not likely to create a problem for rebar bond. The transverse forces due to passing magnets will need to be assessed in magnitude relative to the specific steel rebar locations in order to determine if an additional design factor should be invoked to modify the design of any embedded steel.
5. In an analogous system, the current flowing in transmission lines in the vicinity of buried metallic conductors (pipelines) can and often does cause interference in the conductors. The magnitude of this interference is heightened by long, parallel exposures and power fault conditions. In such cases, high currents and voltages may be induced along the conductors' length. Energy may also flow directly from power installations to buried conductors through conductive paths (soil). This direct flow of energy can cause severe voltage stresses on the pipeline and its coating. It is not clear to us that the maglev based currents can be modelled solely by transmission line currents, however, since the transmission line currents typically do not contain the transients expected to dominate in a maglev system.

6. The interference caused on the pipeline due to the transmission line can be mitigated using gradient control wires. These wires (zinc anodes) reduce the potential difference between the pipeline and the surrounding soil thereby reducing stress voltages.

7. The analysis of power line coupling to pipelines can be performed using sophisticated computer techniques. These programs can also be utilized to evaluate the various mitigation techniques.

Power Dissipation and Magnetic Forces on MAGLEV Rebars

by

Markus Zahn and Rabi Karmacharya

1 Background

Concrete guideways for MAGLEV vehicles may be typically reinforced with steel rebars which are electrically conducting and magnetizable. In the presence of transient magnetic fields due to passing MAGLEV vehicles, transient currents will be induced in the rebars leading to electrical power dissipation and local temperature rise. The induced currents in the presence of magnetic field will also cause a transient Lorentz force on the rebar in the direction of weaker magnetic field and thus in the direction away from the vehicle. If the rebar is magnetizable there is also a magnetization force in the direction of stronger magnetic field and thus in the direction towards the vehicle. The relative strength of these opposing forces are time varying and depend on the magnetic permeability of the rebar, on the skin-depth, on the magnetic diffusion time, on the magnetic field gradient, and on the bar radius. The heating and transverse force make it necessary to study if the concrete strength is maintained over the usual life in the presence of time varying magnetic fields. In order to develop engineering guidelines the rebar magnetic problem was idealized to consider an infinitely long cylinder with constant ohmic conductivity and constant magnetic permeability with the imposed magnetic field having at most a weak gradient so that the magnetic field distribution can be taken as if the imposed field was uniform. The gradient field analysis is necessary to calculate the force on the rebar due to field gradients. In a purely uniform magnetic field there is no net force on the rebar either due to the Lorentz force on the induced currents or due to magnetization. The analysis separately considers the imposed magnetic field to be purely axial or purely transverse to the cylinder axis. The analysis also separately considers the sinusoidal steady state, applicable when many sinusoidal cycles occur, and to step and impulse time transients. The analysis is specifically applied to representative rebar materials listed in Table I.

2 Governing Magnetoquasistatic Equations

2.1 Maxwell's Equations

Maxwell's field equations in the magnetoquasistatic limit for constant magnetic permeability μ and constant ohmic conductivity σ are:

$$\nabla \times \vec{E} = -\mu \frac{\partial \vec{H}}{\partial t} \quad (\text{Faraday's Law}) \quad (1)$$

$$\nabla \times \vec{H} = \vec{J} = \sigma \vec{E} \quad (\text{Ampere's Law with Ohmic Conduction}) \quad (2)$$

$$\nabla \cdot (\mu \vec{H}) = 0 \quad (\text{Gauss' Law}) \quad (3)$$

These can be combined into diffusion equations for the magnetic field \vec{H} or the current density \vec{J}

$$\nabla^2 \vec{H} = \mu \sigma \frac{\partial \vec{H}}{\partial t} \quad (4)$$

$$\nabla^2 \vec{J} = \mu \sigma \frac{\partial \vec{J}}{\partial t} \quad (5)$$

2.2 Boundary Conditions

Boundary conditions are the continuity of tangential \vec{H}

$$\vec{n} \times [\vec{H}_1 - \vec{H}_2] = 0 \quad (6)$$

and continuity of normal $\vec{B} = \mu \vec{H}$

$$\vec{n} \cdot [\mu_1 \vec{H}_1 - \mu_2 \vec{H}_2] = 0 \quad (7)$$

Table 1: Electrical properties of various metals at 20° C

Material	$\frac{\mu}{\mu_o}$	$\rho = 1/\sigma$ ($\mu ohm - m$)	δ at 60 Hz (mm)
Copper	1	0.01724	8.5
Aluminum	1	0.0283	10.9
Steel: mild	5000	0.118	0.316
stainless	1	0.910	62.0
13 Mn	1.01	0.711	54.5
Grade 50 Rebar	3800	0.224	0.499
Grade 60 Rebar	3800	0.230	0.505

2.3 Dissipated Power

The power dissipated per unit axial length, P , in the lossy cylinder of radius R is

$$P = \int_{r=0}^R \int_{\phi=0}^{2\pi} \frac{|\vec{J}|^2}{\sigma} r dr d\phi \quad (8)$$

2.4 Force per unit axial length

2.4.1 Lorentz Force

The magnetic force per unit axial length on the cylinder due to the Lorentz force on the induced currents in the magnetic field is

$$\vec{f}_L = \int_{r=0}^R \int_{\phi=0}^{2\pi} \vec{J} \times \mu \vec{H} r dr d\phi \quad (9)$$

2.4.2 Magnetization Force

The magnetization force on linear magnetizable material with magnetic permeability that depends on space is

$$\vec{f}_M = -\frac{1}{2} \int_{r=0}^R \int_{\phi=0}^{2\pi} |\vec{H}|^2 \nabla \mu(\vec{r}) r dr d\phi = -\frac{1}{2} \int_{r=0}^R \int_{\phi=0}^{2\pi} [H_\phi^2 + H_z^2] \nabla \mu(\vec{r}) - B_r^2 \nabla \left(\frac{1}{\mu(\vec{r})} \right) r dr d\phi \quad (10)$$

where we separate terms of tangential \vec{H} and normal \vec{B} at the cylindrical interface at $r = R$ because tangential components of \vec{H} , H_ϕ and H_z , are continuous, while the normal component of \vec{B} , B_r , is continuous. Since the magnetic permeability is constant everywhere except at the $r = R$ interface where $\mu(\vec{r})$ and $\frac{1}{\mu(\vec{r})}$ take steps we have that

$$\nabla \mu(\vec{r}) = (\mu_o - \mu) \delta(r - R) \vec{i}_r = (\mu_o - \mu) \delta(r - R) [\vec{i}_x \cos \phi + \vec{i}_y \sin \phi] \quad (11)$$

$$\nabla \left(\frac{1}{\mu(\vec{r})} \right) = \left(\frac{1}{\mu_o} - \frac{1}{\mu} \right) \delta(r - R) \vec{i}_r = \left(\frac{1}{\mu_o} - \frac{1}{\mu} \right) \delta(r - R) (\vec{i}_x \cos \phi + \vec{i}_y \sin \phi) \quad (12)$$

The spatial impulse at $r = R$, $\delta(r - R)$, indicates that the magnetization force is a surface force. With H_ϕ , H_z , and B_r continuous through the interface, (10) reduces to

$$\vec{f}_M = \frac{R}{2} \int_{\phi=0}^{2\pi} \left[(\mu - \mu_o) [H_\phi^2(r = R) + H_z^2(r = R)] + B_r^2(r = R) \left(\frac{1}{\mu_o} - \frac{1}{\mu} \right) \right] [\vec{i}_x \cos \phi + \vec{i}_y \sin \phi] d\phi \quad (13)$$

where it was convenient to replace the radial unit vector \vec{i}_r by its Cartesian components to explicitly show the ϕ dependence of \vec{i}_r . If $|\vec{H}(r = R)|^2$ is an even power trigonometric function of ϕ , the integration of (13) is zero. This will be the case if the applied magnetic field, whether axial or transverse, is uniform. To

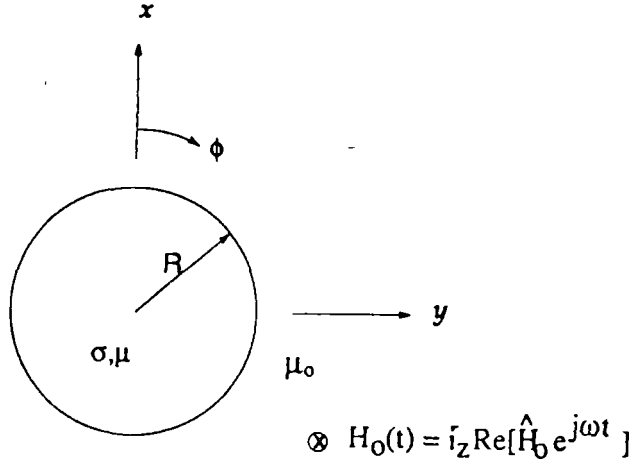


Figure 1: A cylinder of radius R , ohmic conductivity σ , and magnetic permeability μ is placed in a uniform z directed magnetic field that is parallel to the cylinder axis and varies sinusoidally with time at angular frequency ω .

approximate a realistic magnetic field configuration with a slight non-uniformity over the cylinder, we take the applied magnetic field to be of the form

$$\vec{H} = \vec{H}_0[1 + a \sin \phi] \quad (14)$$

where a is a measure of the magnetic field gradient. The magnetic field is $(1 + a)$ at $\phi = \pi/2$ and is $(1 - a)$ at $\phi = -\pi/2$. With a positive, the field is bigger for positive y than for negative y . If $a \ll 1$, the magnetic field and current density solutions are approximately correct if the imposed uniform field is replaced by (14). For our numerical case studies we take $a = 0.1$, corresponding to a maximum of $\pm 10\%$ magnetic field variation at the left and right hand cylinder edges compared to the top and bottom of the cylinder at $\phi = 0, \pi$ in Fig. (1).

3 Axial Magnetic Field In the Sinusoidal Steady State

3.1 Exact Solutions for Magnetic Field and Current Density

Figure 1 shows a uniform axial magnetic field in the z direction varying sinusoidally in time with angular frequency ω . The total magnetic field remains purely z directed and is of the form

$$\vec{H} = \text{Re}[\hat{H}_z(r)e^{j\omega t}]\vec{i}_z \quad (15)$$

The diffusion equation of (4) then becomes

$$\frac{1}{r} \frac{d}{dr} \left(r \frac{d\hat{H}_z}{dr} \right) = j\omega\mu\sigma\hat{H}_z \quad (16)$$

Defining the skin depth as

$$\delta = \sqrt{\frac{2}{\omega\mu\sigma}} \quad (17)$$

(16) becomes a Bessel equation

$$r^2 \frac{d^2 \hat{H}_z}{dr^2} + r \frac{d\hat{H}_z}{dr} - \frac{2jr^2}{\delta^2} \hat{H}_z = 0 \quad (18)$$

with solutions that satisfy the boundary condition

$$\hat{H}_z(r = R) = \hat{H}_0 \quad (19)$$

as

$$\hat{H}_z = \frac{\hat{H}_o J_o[(1-j)r/\delta]}{J_o[(1-j)R/\delta]} \quad (20)$$

The current density is obtained from Ampere's law as

$$\vec{J} = \nabla \times \vec{H} \Rightarrow \hat{J}_\phi = -\frac{d\hat{H}_z}{dr} = \frac{\hat{H}_o(1-j)}{\delta} \frac{J_1[(1-j)r/\delta]}{J_o[(1-j)R/\delta]} \quad (21)$$

3.2 Exact Solution for Dissipated Power per unit length

The time average power dissipation per unit length after integrating over ϕ in (8) is then

$$\langle P \rangle = \pi \int_{r=0}^R \frac{|\hat{J}_\phi|^2}{\sigma} r dr = \frac{2\pi |\hat{H}_o|^2}{\sigma \delta^2 |J_o[(1-j)R/\delta]|^2} \int_{r=0}^R J_1[(1-j)r/\delta] J_1[(1+j)r/\delta] r dr \quad (22)$$

The last integral is a Lommel integral which is exactly integral

$$\int_{r=0}^R r J_n[\sqrt{jp}r] J_n[\sqrt{-jp}r] dr = \frac{R}{2jp} \left[\sqrt{-jp} J_n[\sqrt{jp}R] J_{n-1}[\sqrt{-jp}R] - \sqrt{jp} J_n[\sqrt{-jp}R] J_{n-1}[\sqrt{jp}R] \right] \quad (23)$$

For our problem $n = 1$ and $p = 2/\delta^2$ so that (22) reduces to

$$\langle P \rangle = \frac{\pi |\hat{H}_o|^2 R}{2\sigma \delta |J_o[(1-j)R/\delta]|^2} [(j-1)J_1[\sqrt{-2j}R/\delta] J_o[\sqrt{2j}R/\delta] - (j+1)J_1[\sqrt{2j}R/\delta] J_o[\sqrt{-2j}R/\delta]] \quad (24)$$

3.3 Non-dimensional Solutions

It is convenient to non-dimensionalize variables to the applied magnetic field amplitude \hat{H}_o and to the cylinder radius R

$$\tilde{H}_z = \frac{\hat{H}_z}{\hat{H}_o}, \quad \tilde{J}_\phi = \hat{J}_\phi R / \hat{H}_o, \quad \tilde{r} = r/R, \quad \tilde{\delta} = \delta/R; \quad \langle \tilde{P} \rangle = \frac{\langle P \rangle \sigma}{\pi |\hat{H}_o|^2} \quad (25)$$

so that the solutions of (20), (21), and (24) are

$$\tilde{H}_z = \frac{\hat{H}_z}{\hat{H}_o} = \frac{J_o[(1-j)\tilde{r}/\tilde{\delta}]}{J_o[(1-j)/\tilde{\delta}]} \quad (26)$$

$$\tilde{J}_\phi = \frac{\hat{J}_\phi R}{\hat{H}_o} = \frac{(1-j)}{\tilde{\delta}} \frac{J_1[(1-j)\tilde{r}/\tilde{\delta}]}{J_o[(1-j)/\tilde{\delta}]} \quad (27)$$

$$\begin{aligned} \langle \tilde{P} \rangle &= \frac{\langle P \rangle \sigma}{\pi |\hat{H}_o|^2} \\ &= \int_0^1 |\tilde{J}_\phi|^2 \tilde{r} d\tilde{r} \\ &= \frac{[(j-1)J_1[\sqrt{-2j}/\tilde{\delta}] J_o[\sqrt{2j}/\tilde{\delta}] - (j+1)J_1[\sqrt{2j}/\tilde{\delta}] J_o[\sqrt{-2j}/\tilde{\delta}]]}{2\tilde{\delta} |J_o[\sqrt{2j}/\tilde{\delta}]|^2} \end{aligned} \quad (28)$$

Figure 2 plots the non-dimensional dissipated power in (28) versus non-dimensional skin-depth, $\tilde{\delta} = \delta/R$. Figure 3 applies (24) to the materials in Table 1 and plots dimensional dissipated power per unit length versus frequency f in hertz, $f = \omega/2\pi$, for cylinder radii of $R=0.5, 1.0,$ and 1.5 cm with an applied peak magnetic field strength of $|\mu_o \hat{H}_o| = 0.5$ tesla.

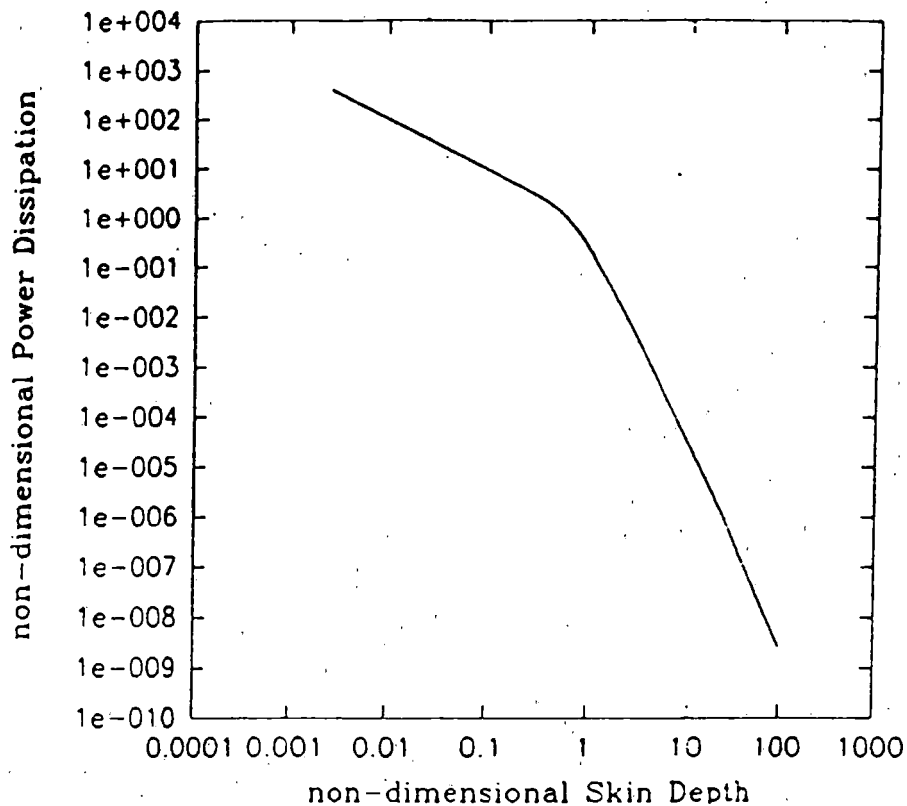


Figure 2: Non-dimensional dissipated power, $\langle \bar{P} \rangle = \langle P \rangle \sigma / [\pi | \hat{H}_o |^2]$ versus non-dimensional skin-depth, $\bar{\delta} = \delta/R$, in a lossy, magnetizable cylinder placed in a uniform axial magnetic field.

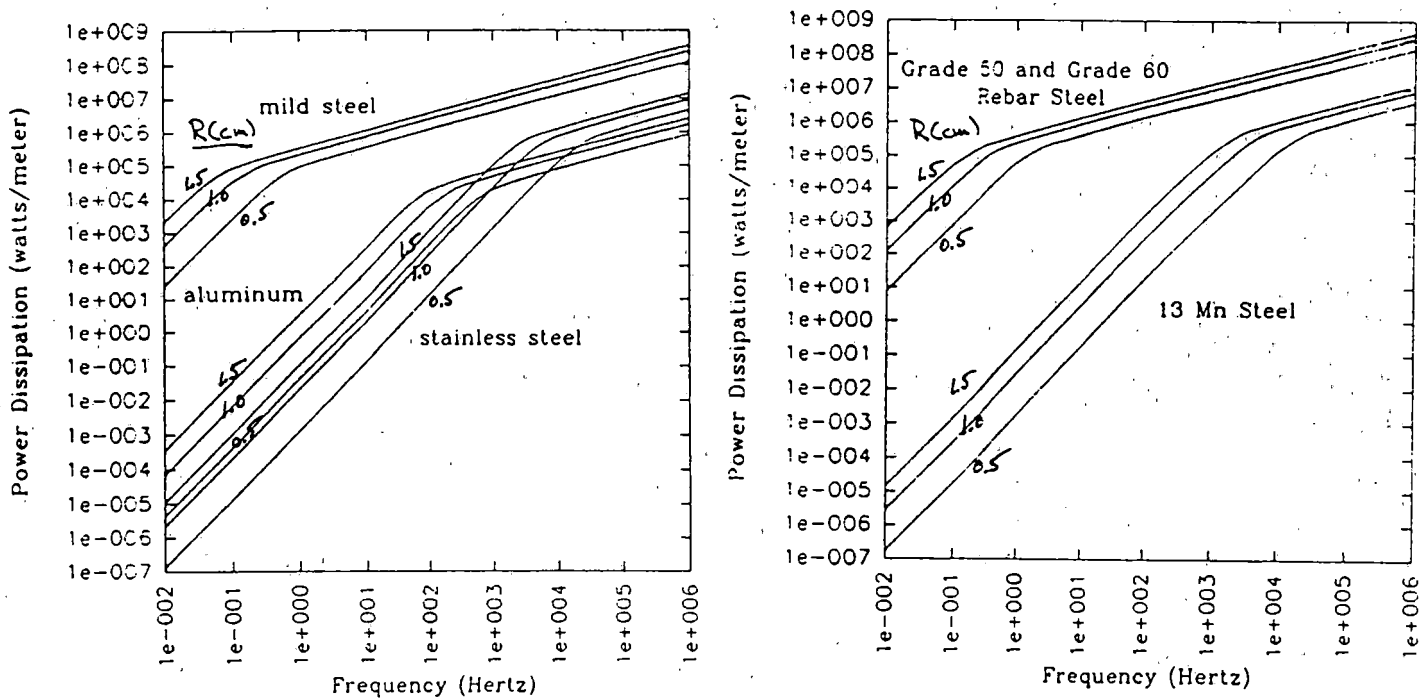


Figure 3: Dimensional dissipated power per unit length (watts/m) for an axial magnetic field versus frequency in Hertz for the materials in Table 1 for radius $R=0.5, 1.0,$ and 1.5 cm with peak magnetic field strength $|\mu_c \hat{H}_o| = 0.5$ tesla.

3.4 Force Per Unit Length

3.4.1 Lorentz force per unit length

In a perfectly uniform applied field the Lorentz force of (9) would integrate to zero. We thus assume that the applied magnetic field has the slight non-uniformity over the cylinders given by (14). The Lorentz volume force density [newtons/m³] is

$$\vec{F}_L = \vec{J} \times \mu \vec{H} = \mu J_\phi H_z \vec{i}_r = \mu J_\phi H_z [\cos \phi \vec{i}_x + \sin \phi \vec{i}_y] \quad (29)$$

where we convert to Cartesian coordinates to explicitly show the ϕ dependence of \vec{i}_r . Substituting (29) into (9) gives the time average Lorentz force per unit length as purely y directed.

$$\begin{aligned} \langle f_{Ly} \rangle &= \frac{1}{2} \text{Re} \int_{r=0}^R \int_{\phi=0}^{2\pi} \mu \vec{J}_\phi \hat{H}_z^* \sin \phi r dr d\phi \\ &= \frac{\mu |\hat{H}_o|^2}{2\delta |J_o[(1-j)R/\delta]|^2} \text{Re}(1-j) \int_{r=0}^R \int_{\phi=0}^{2\pi} \sin \phi [1 + a \sin \phi]^2 J_o[(1+j)r/\delta] J_1[(1-j)r/\delta] r dr d\phi \\ &= \frac{\pi a \mu |\hat{H}_o|^2}{\delta |J_o[(1-j)R/\delta]|^2} \text{Re} \int_{r=0}^R (1-j) J_1[(1-j)r/\delta] J_o[(1+j)r/\delta] r dr \end{aligned} \quad (30)$$

It is also convenient to non-dimensionalize all forces per unit length as

$$\langle \bar{f} \rangle = \frac{\langle f \rangle}{\pi a \mu R |\hat{H}_o|^2} \quad (31)$$

so that (30) becomes

$$\langle \bar{f}_{Ly} \rangle = \frac{\langle f_{Ly} \rangle}{\pi a \mu R |\hat{H}_o|^2} = \frac{1}{\delta |J_o[(1-j)/\delta]|^2} \text{Re}(1-j) \int_0^1 J_1[(1-j)\bar{r}/\delta] J_o[(1+j)\bar{r}/\delta] \bar{r} d\bar{r} \quad (32)$$

The integration over \bar{r} is done numerically and gives the non-dimensional plots in Fig. 4.

3.5 Magnetization Force per unit length

The time average of the magnetization force in (13) is

$$\langle \bar{f}_M \rangle = \frac{1}{4} (\mu - \mu_o) |\hat{H}_o|^2 R \int_{\phi=0}^{2\pi} [1 + a \sin \phi]^2 [\vec{i}_x \cos \phi + \vec{i}_y \sin \phi] d\phi \quad (33)$$

which has $\langle f_{Mx} \rangle = 0$ and

$$\langle f_{My} \rangle = \frac{1}{2} (\mu - \mu_o) |\hat{H}_o|^2 \pi a R \quad (34)$$

Fig. (5) plots the dimensional y component of the total time average force per unit axial length, $\langle f_y \rangle = \langle f_{Ly} \rangle + \langle f_{My} \rangle$, versus frequency for the materials in Table 1 taking R to be 0.5, 1.0, and 1.5 cm, $a = 0.1$, and $|\mu_o \hat{H}_o| = 0.5$ teslas. Note that for non-magnetic materials and for magnetic steel materials at high frequency the force is always $-y$ directed, that is, in the direction of decreasing magnetic field. For magnetic steel materials, the force is $+y$ directed at low frequencies due to the cylinder magnetization being attracted to strong magnetic field regions. The dips in the force curves show the force passing through zero on the log-log plots.

3.6 Approximate Limits

It is clear from the breakpoints in dissipated power and force plots of Figs. (2)-(5) that the solutions have approximate limiting expressions for skin-depth large or small compared to cylinder radius.

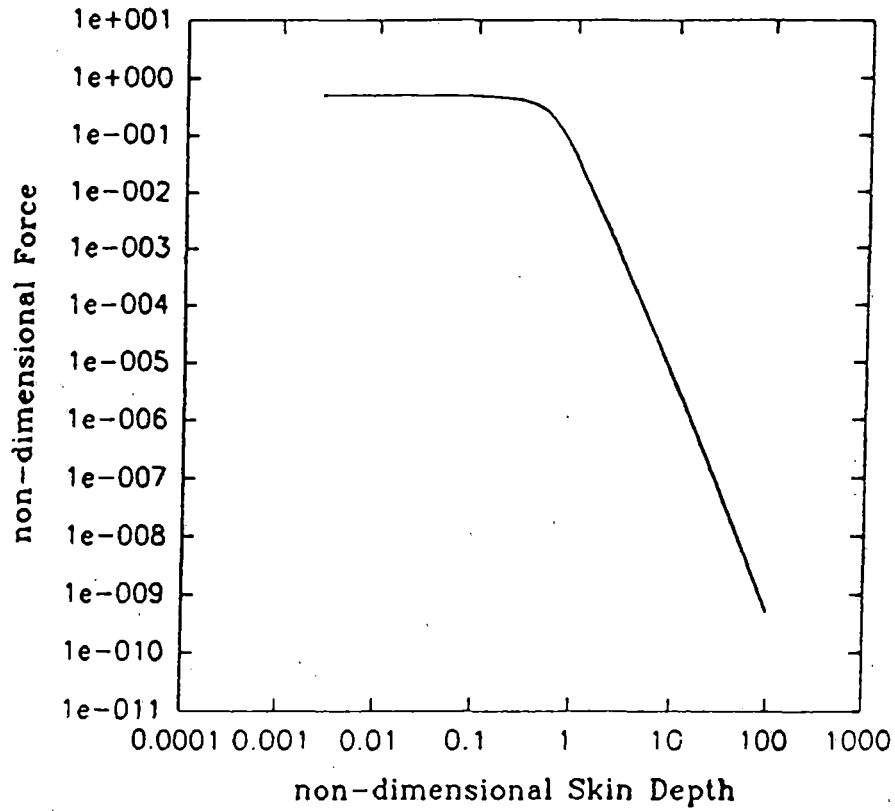


Figure 4: Non-dimensional y directed Lorentz force per unit length, $\langle \tilde{f}_y \rangle = \langle f_y \rangle / [\pi a \mu R |\hat{H}_o|^2]$, versus non-dimensional skin-depth, $\tilde{\delta} = \delta/R$, of a lossy, magnetizable cylinder placed in a uniform axial magnetic field.

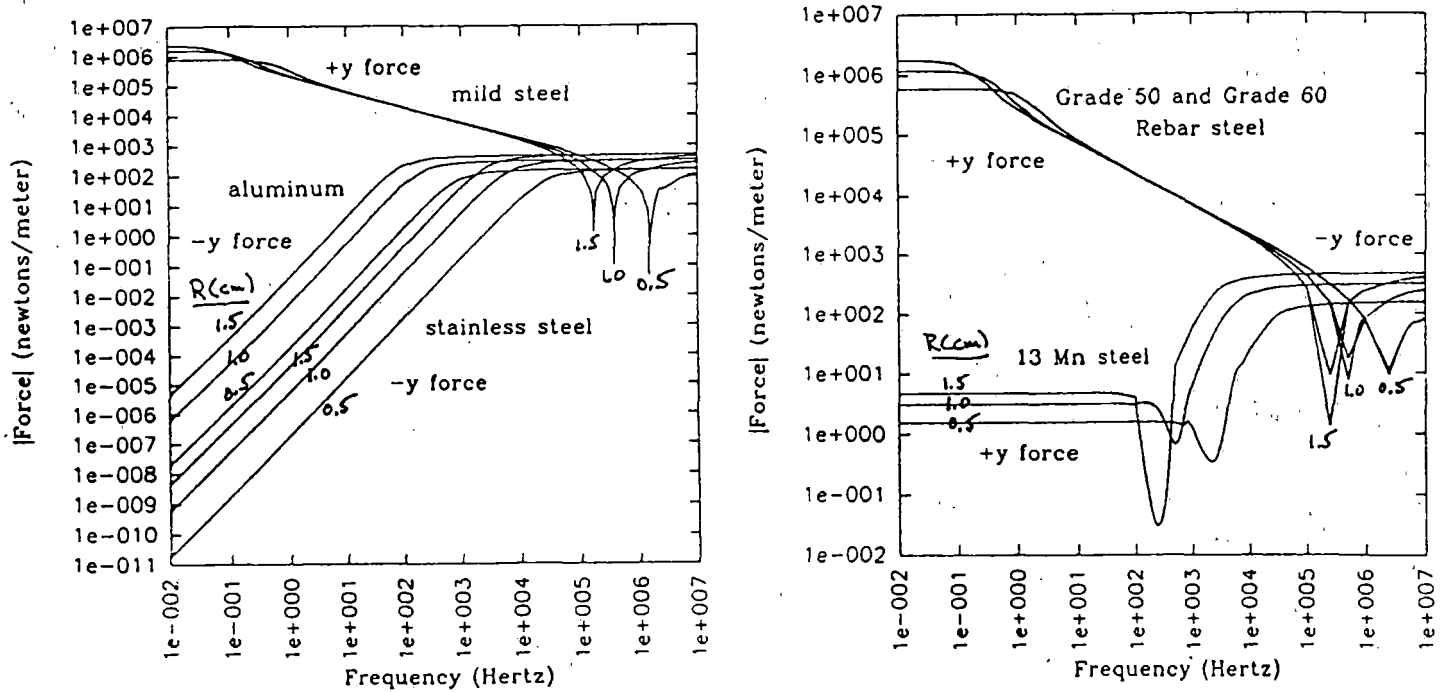


Figure 5: Total dimensional force per unit length (newtons/m) in the y direction versus frequency in Hertz due to the sum of Lorentz and magnetization forces from an axial magnetic field with a weak gradient, $a=0.1$, in the y direction for radius $R=0.5, 1.0$, and 1.5 cm with peak magnetic field strength of $|\mu_o \hat{H}_o| = 0.5$ tesla.

3.6.1 Small Skin-depth Limit, $\delta/R \ll 1$

When $\delta/R \ll 1$, the zero and first order Bessel functions approximately reduce to

$$J_0[(1-j)r/\delta] \approx \sqrt{\frac{\delta(1-j)}{\pi r}} \frac{e^{(1+j)r/\delta}}{2}; \quad J_1[(1-j)r/\delta] \approx -j \sqrt{\frac{\delta(1-j)}{\pi r}} \frac{e^{(1+j)r/\delta}}{2} \quad (35)$$

Then the dimensional and non-dimensional magnetic field and current density distributions approximately reduce to

$$\begin{aligned} \hat{H}_z &\approx \hat{H}_o \sqrt{\frac{R}{r}} e^{(1+j)(r-R)/\delta}; & \bar{H}_z &\approx \frac{\hat{H}_z}{\hat{H}_o} = \frac{1}{\sqrt{\bar{r}}} e^{(1+j)(\bar{r}-1)/\delta} \\ \hat{J}_\phi &\approx -\frac{\hat{H}_o(1+j)}{\delta} \sqrt{\frac{R}{r}} e^{(1+j)(r-R)/\delta}; & \bar{J}_\phi &\approx \frac{\hat{J}_\phi R}{\hat{H}_o} = -\frac{(1+j)}{\delta \sqrt{\bar{r}}} e^{(1+j)(\bar{r}-1)/\delta} \end{aligned} \quad (36)$$

The dimensional and non-dimensional dissipated power per unit length and total force per unit length in a weak gradient magnetic field of (14) are then

$$\langle P \rangle \approx \frac{\pi R |\hat{H}_o|^2}{\sigma \delta}; \quad \langle \bar{P} \rangle = \frac{\langle P \rangle \sigma}{\pi |\hat{H}_o|^2} \approx \frac{1}{\delta} \quad (37)$$

$$\langle f_y \rangle \approx -\frac{\mu_o \pi a R}{2} |\hat{H}_o|^2; \quad \langle \bar{f}_y \rangle = \frac{\langle f_y \rangle}{\pi a \mu R |\hat{H}_o|^2} \approx -\frac{\mu_o}{2\mu} \quad (38)$$

To approximately verify (37) we realize that for small skin-depth, all the current is approximately confined to a skin-depth thick layer at the $r = R$ surface. With the magnetic field outside equal to \hat{H}_o dropping to approximately zero within a distance δ away from the interface, the surface current density which equals the discontinuity in tangential \hat{H} at the interface is $\hat{K}_\phi \approx -\hat{H}_o$. Then the volume current density magnitude within this skin-depth thick layer is $|\hat{J}_\phi| \approx |\hat{K}_\phi/\delta| \approx |\hat{H}_o|/\delta$. The power dissipated per unit length is then approximately

$$\langle P \rangle \approx \frac{1}{2} \frac{|\hat{J}_\phi|^2}{\sigma} 2\pi R \delta \approx \frac{|\hat{H}_o|^2 \pi R}{\sigma \delta} \quad (39)$$

in agreement with (37).

3.6.2 Large Skin-depth Limit, $\delta/R \gg 1$

When $\delta/R \gg 1$, the zero and first order Bessel functions approximately reduce to

$$\begin{aligned} J_0 \left[\frac{(1-j)r}{\delta} \right] &\approx 1 + \frac{j r^2}{2\delta^2} \\ J_1 \left[\frac{(1-j)r}{\delta} \right] &\approx \frac{(1-j)r}{2\delta} \left[1 + \frac{j r^2}{4\delta^2} \right] \end{aligned} \quad (40)$$

It is necessary to expand to order $1/\delta^3$ in order to properly calculate the first order force per unit axial length which varies as $1/\delta^4$, as in some cases the higher order terms integrate to zero. The dimensional and non-dimensional magnetic field and current density distributions then reduce to

$$\hat{H}_z \approx \hat{H}_o \frac{[1 + \frac{j r^2}{2\delta^2}]}{[1 + j \frac{R^2}{2\delta^2}]}; \quad \bar{H}_z = \frac{\hat{H}_z}{\hat{H}_o} \approx \frac{1 + \frac{j \bar{r}^2}{2\delta^2}}{1 + \frac{j}{2\delta}} \quad (41)$$

$$\hat{J}_\phi \approx -\frac{j \hat{H}_o}{\delta^2} r \left[1 - \frac{j R^2}{2\delta^2} \right] \left[1 + \frac{j r^2}{4\delta^2} \right]; \quad \bar{J}_\phi = \frac{\hat{J}_\phi R}{\hat{H}_o} \approx -\frac{j \bar{r}}{\delta^2} \left[1 - \frac{j}{2\delta^2} \right] \left[1 + \frac{j \bar{r}^2}{4\delta^2} \right] \quad (42)$$

The approximate dimensional and non-dimensional power per unit length and force per unit length in a weak gradient magnetic field are then

$$\langle P \rangle \approx \frac{\pi R^4 |\hat{H}_o|^2}{4\sigma \delta^4}; \quad \langle \bar{P} \rangle = \frac{\langle P \rangle \sigma}{\pi |\hat{H}_o|^2} \approx \frac{1}{4\delta^4} \quad (43)$$

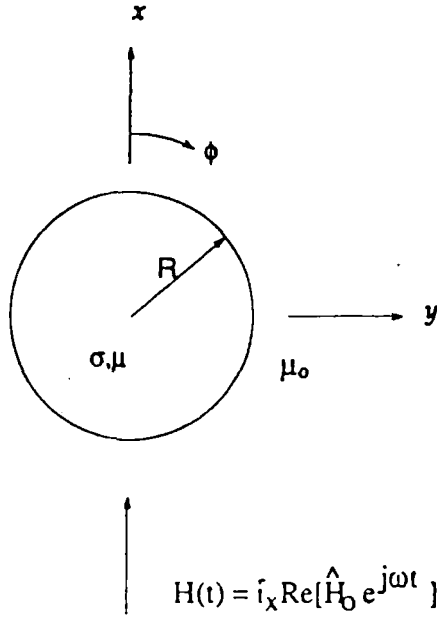


Figure 6: A cylinder of radius R , ohmic conductivity σ , and magnetic permeability μ is placed in a uniform x directed magnetic field that is transverse to the cylinder axis and varies sinusoidally with time at angular frequency ω .

$$\langle f_y \rangle \approx \left[\frac{1}{2}(\mu - \mu_0) - \frac{\mu R^4}{20\delta^4} \right] \pi a R |\hat{H}_o|^2; \quad \langle \bar{f}_y \rangle = \frac{\langle f_y \rangle}{\pi a \mu R |\hat{H}_o|^2} \approx \frac{1}{2} \left(1 - \frac{\mu_0}{\mu} \right) - \frac{1}{20\delta^4} \quad (44)$$

These results can also be checked with a simple approximate model. If the skin-depth is much larger than the cylinder radius, the internal magnetic field approximately equals the imposed field, $\hat{H}_z \approx \hat{H}_o$, and the induced magnetic field due to induced eddy currents is small. Applying the integral form of Faraday's Law to a circular contour of radius r approximately gives

$$\oint_C \vec{E} \cdot d\vec{l} = -\frac{d}{dt} \int_S \vec{B} \cdot d\vec{a} \Rightarrow E_\phi 2\pi r = -\pi r^2 \mu \frac{dH_z}{dt} \quad (45)$$

which can be solved for the induced current density as

$$\hat{J}_\phi = \sigma \hat{E}_\phi = -\frac{\sigma \mu r}{2} j\omega \hat{H}_o = -\frac{j r}{\delta^2} \hat{H}_o \quad (46)$$

which approximately agrees with the predominant term in (42). The time average power dissipated per unit length is then

$$\langle P \rangle = \frac{1}{2} \int_{r=0}^R \frac{|\hat{J}_\phi|^2}{\sigma} 2\pi r dr = \frac{\pi |\hat{H}_o|^2}{\sigma \delta^4} \int_0^R r^3 dr = \frac{\pi |\hat{H}_o|^2 R^4}{4\sigma \delta^4} \quad (47)$$

in agreement with (43).

4 Transverse Magnetic Field in the Sinusoidal Steady State

4.1 Exact Solution for Magnetic Field and Current Density

Figure (6) shows a uniform transverse magnetic field in the x direction varying sinusoidally in time with angular frequency ω . The resulting magnetic field then has r and ϕ components while the induced current has only a z component. Because the direction of \vec{H} varies with position, the vector Laplacian in cylindrical coordinates in (4) is different and more complicated than the scalar Laplacian. However, with the direction of \vec{J} constant with position the vector Laplacian in (5) equals the simpler scalar Laplacian, so we choose to solve (5) for the current density. We take the current density to be of the form

$$J_z(r, \phi, t) = \text{Re}[\hat{J}_z(r) \sin \phi e^{j\omega t}] \quad (48)$$

so that (5) becomes

$$\frac{d^2 \hat{J}_z}{dr^2} + \frac{1}{r} \frac{d\hat{J}_z}{dr} - \hat{J}_z \left[\frac{1}{r^2} + \frac{2j}{\delta^2} \right] = 0 \quad (49)$$

with solution of the form

$$\hat{J}_z = C J_1 \left[\frac{(1-j)r}{\delta} \right] \quad (50)$$

where C is a constant to be determined from boundary conditions. The magnetic field distribution inside the cylinder is found from (50) using Faraday's law

$$\nabla \times \left(\frac{\vec{J}}{\sigma} \right) = -\mu \frac{d\vec{H}}{dt} \quad (51)$$

while outside the cylinder the magnetic field is the uniform applied field plus a line dipole field due to the induced current which results from solutions to Laplace's equation for a scalar magnetic potential or a z directed vector potential

$$\vec{H} = \begin{cases} \frac{jC\delta^2}{2} \left[\vec{i}_r \frac{1}{r} J_1 \left[\frac{(1-j)r}{\delta} \right] \cos \phi - \vec{i}_\phi \left[\frac{(1-j)}{\delta} J_0 \left[\frac{(1-j)r}{\delta} \right] - \frac{1}{r} J_1 \left[\frac{(1-j)r}{\delta} \right] \right] \sin \phi & 0 < r < R \\ [H_o + \frac{D}{r^2}] \cos \phi \vec{i}_r - [H_o - \frac{D}{r^2}] \sin \phi \vec{i}_\phi & r > R \end{cases} \quad (52)$$

where C and D are found from the boundary conditions of continuity of tangential \vec{H} and normal \vec{B} at $r = R$

$$H_\phi(r = R_-) = H_\phi(r = R_+); \quad \mu H_r(r = R_-) = \mu_o H_r(r = R_+) \quad (53)$$

The solutions for the constants C and D are

$$C = \frac{2\mu_o R [H_o + D/R^2]}{j\mu\delta^2 J_1[(1-j)R/\delta]} \quad (54)$$

$$\frac{D}{R^2} = H_o \frac{J_1 \left[\frac{(1-j)R}{\delta} \right] - \frac{\mu_o}{\mu} \left[\frac{(1-j)R}{\delta} J_0 \left[\frac{(1-j)R}{\delta} \right] - J_1 \left[\frac{(1-j)R}{\delta} \right] \right]}{J_1 \left[\frac{(1-j)R}{\delta} \right] + \frac{\mu_o}{\mu} \left[\frac{(1-j)R}{\delta} J_0 \left[\frac{(1-j)R}{\delta} \right] - J_1 \left[\frac{(1-j)R}{\delta} \right] \right]} \quad (55)$$

4.2 Exact Solution for Dissipated Power Per Unit Length

The time average power dissipation per unit length is then

$$\begin{aligned} \langle P \rangle &= \pi \int_{r=0}^R \frac{|\hat{J}_z|^2}{\sigma} r dr = \frac{\pi |C|^2}{\sigma} \int_{r=0}^R J_1 \left[\frac{(1-j)r}{\delta} \right] J_1 \left[\frac{(1+j)r}{\delta} \right] r dr \\ &= \frac{\pi |C|^2 R \delta}{\sigma 4j} \left[\sqrt{-2j} J_1 \left[\frac{\sqrt{2j}R}{\delta} \right] J_0 \left[\frac{\sqrt{-2j}R}{\delta} \right] - \sqrt{2j} J_1 \left[\frac{\sqrt{-2j}R}{\delta} \right] J_0 \left[\frac{\sqrt{2j}R}{\delta} \right] \right] \end{aligned} \quad (56)$$

where we use the Lommel integral formula of (23). Using the non-dimensional definitions of (25), Fig. (7) plots (56) versus $\delta = \delta/R$ for various values of μ/μ_o while Fig. (8) plots the dimensional dissipated power per unit length versus frequency for the materials in Table 1 for cylinder radii of $R = 0.5, 1.0,$ and 1.5 cm with an peak applied magnetic field strength of $|\mu_o \hat{H}_o| = 0.5$ tesla.

4.3 Force per unit length

4.3.1 Lorentz Force per unit length

For the Lorentz force density, it is convenient to write cylindrical unit vectors in terms of Cartesian unit vectors

$$\vec{F}_L = \vec{J} \times \mu \vec{H} = \mu J_z [H_r \vec{i}_\phi - H_\phi \vec{i}_r] = \mu J_z [H_r (-\sin \phi \vec{i}_x + \cos \phi \vec{i}_y) - H_\phi (\cos \phi \vec{i}_x + \sin \phi \vec{i}_y)] \quad (57)$$

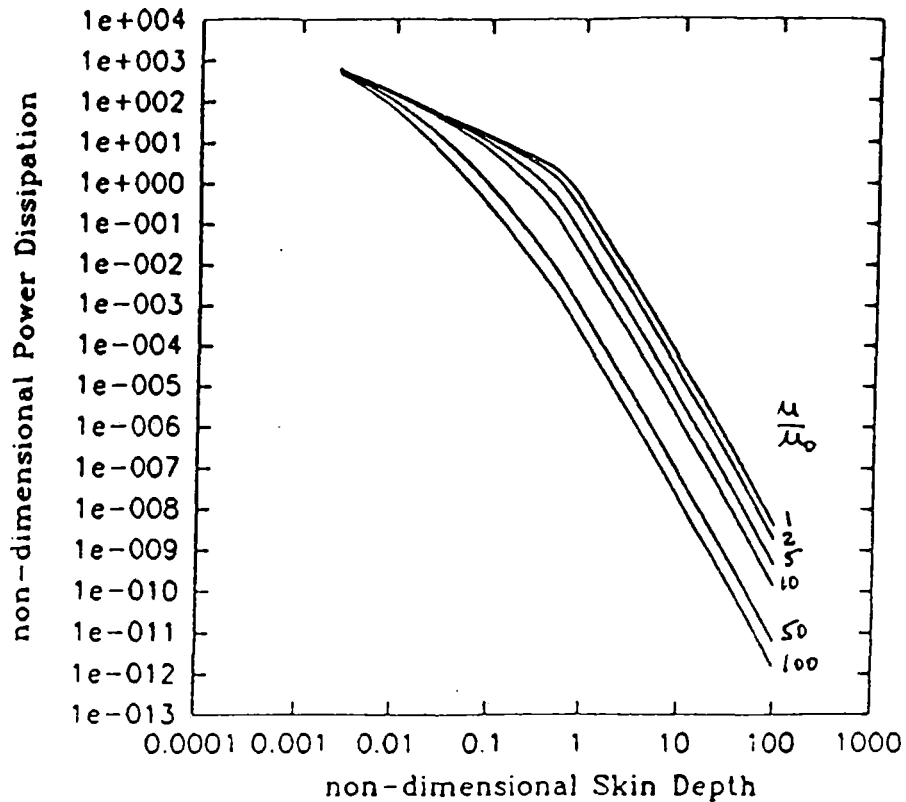


Figure 7: Non-dimensional dissipated power, $\langle \bar{P} \rangle = \langle P \rangle \sigma / \pi | \hat{H}_o |^2$, versus non-dimensional skin-depth, $\delta = \delta/R$, and magnetic permeability in a lossy, magnetizable cylinder placed in a uniform transverse magnetic field.

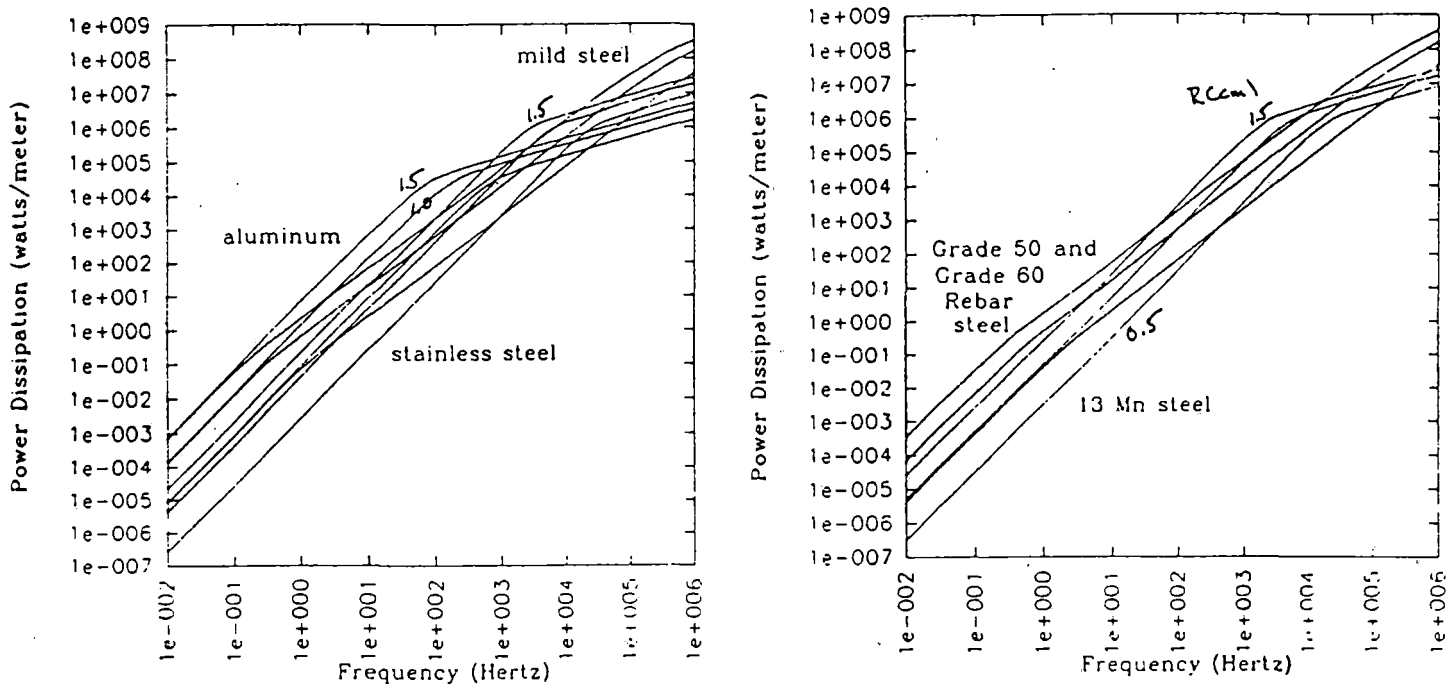


Figure 8: Dimensional dissipated power per unit length (watts/m) in a transverse magnetic field versus frequency in Hertz for the materials in Table 1 for radius $R=0.5, 1.0,$ and 1.5 cm and peak magnetic field strength $|\mu_o \hat{H}_o| = 0.5$ tesla.

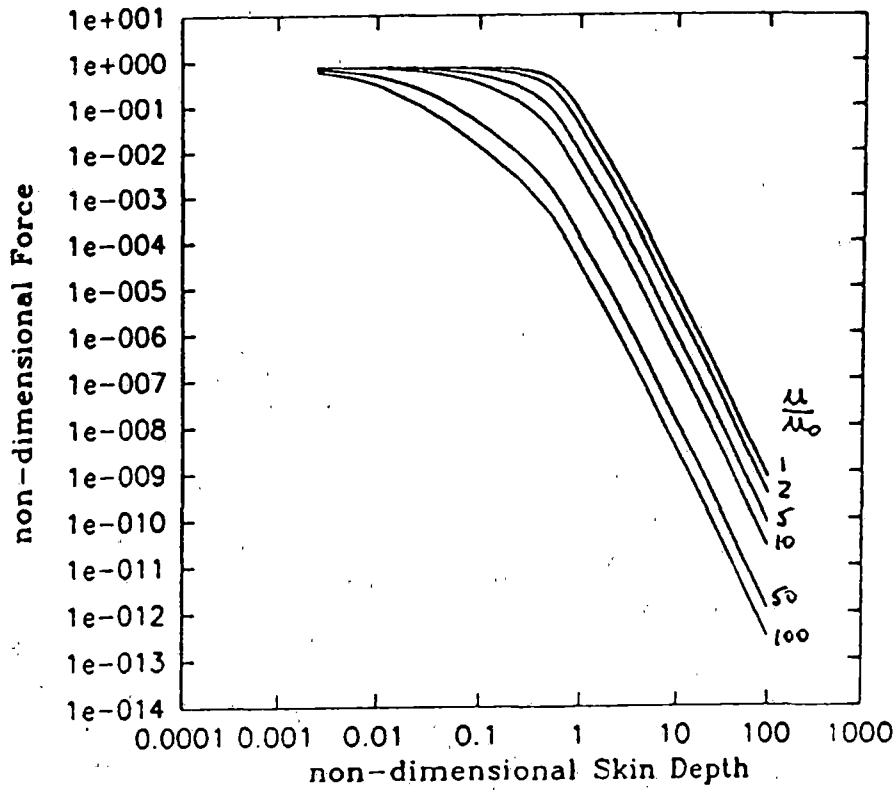


Figure 9: Non-dimensional y directed Lorentz force per unit length, $\langle \tilde{f}_y \rangle = \langle f_y \rangle / [\pi a \mu R |\hat{H}_o|^2]$, versus non-dimensional skin-depth, $\tilde{\delta} = \delta/R$, and magnetic permeability of a lossy, magnetizable cylinder placed in a uniform transverse magnetic field.

The total Lorentz force per unit length is obtained from (9) by integrating (57) over the cylinder cross-sectional area. Again using the weak-gradient approximation of (14), the non-dimensional time average Lorentz force per unit length becomes after integration over ϕ

$$\langle \tilde{f}_{Ly} \rangle = \frac{\langle f_{Ly} \rangle}{\pi a \mu R |\hat{H}_o|^2} = Re \int_{\tilde{r}=0}^1 \frac{1}{4} \tilde{J}_z^* [\tilde{H}_r - 3\tilde{H}_\phi] \tilde{r} d\tilde{r} \quad (58)$$

Evaluating by numerical integration for various values of μ results in the plots in Fig. 9.

4.4 Magnetization Force per unit length

The time average magnetization force per unit length is obtained by substituting (52), (54) and (55) into (13) to yield $\langle f_{Mz} \rangle = 0$ and

$$\langle \tilde{f}_{My} \rangle = \frac{\langle f_{My} \rangle}{\pi a \mu R |\hat{H}_o|^2} = \frac{1}{8} \left[\frac{3(\mu - \mu_o)}{\mu} |\tilde{H}_\phi|^2 + \frac{\mu_o}{\mu} \left(1 - \frac{\mu_o}{\mu}\right) |\tilde{B}_r|^2 \right]_{r=R} \quad (59)$$

The total dimensional magnetic force per unit axial length, the sum of (58) and (59) are plotted in Fig. (10) for the materials in Table 1 for radii of $R = 0.5, 1.0$ and 1.5 cm in a peak magnetic field of $|\mu_o \hat{H}_o| = 0.5$ tesla with $a = 0.1$. Note that for the non-magnetic materials the total force is $-y$ directed, that is in the direction of decreasing magnetic field, while for the highly magnetizable mild steel and Grades 50 and 60 steel over the frequency range of 10^{-2} to 10^6 Hertz, the force is $+y$ directed. This is because the magnetization force which is in the direction of increasing magnetic field exceeds in magnitude the Lorentz force which is in the direction of decreasing magnetic field. For the very weakly magnetic Mn steel, the force is $+y$ directed at low frequencies where the magnetization force dominates and is $-y$ directed at high frequencies where the Lorentz force dominates.

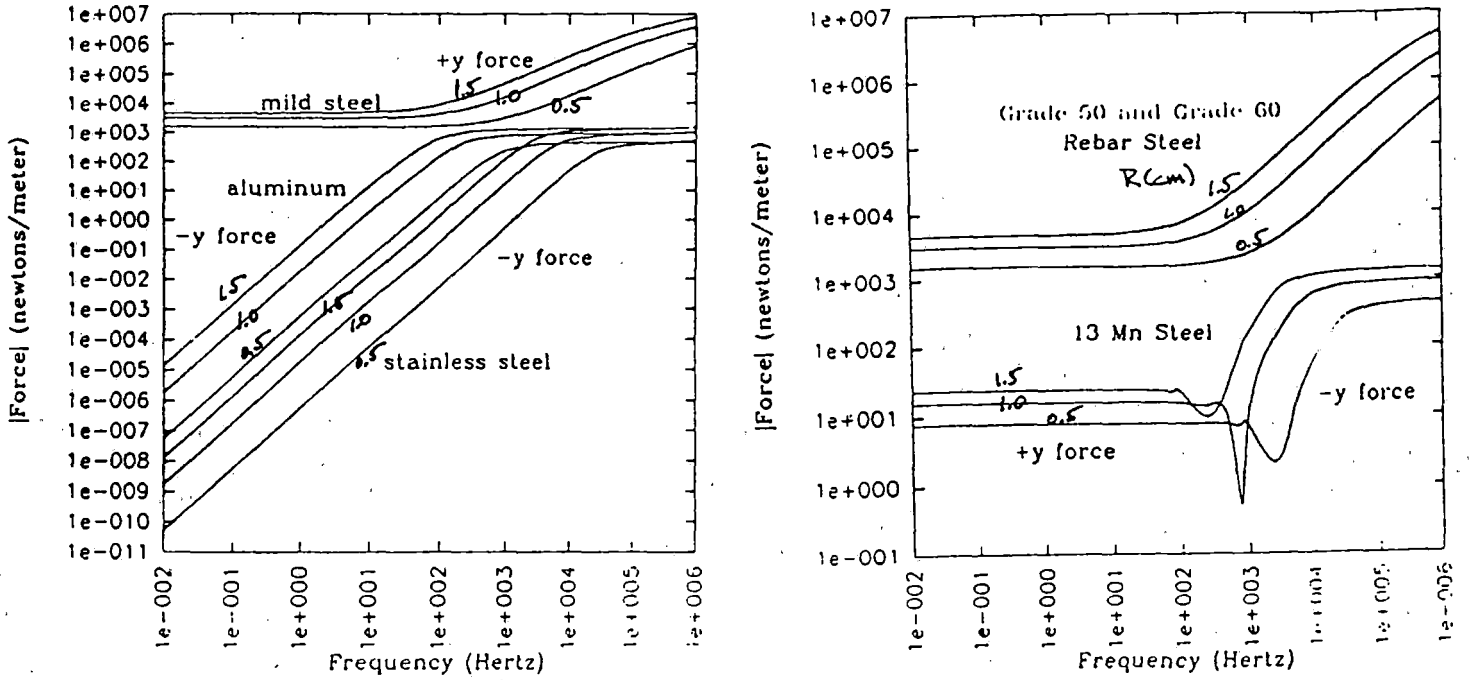


Figure 10: Total dimensional force per unit length (*newtons/m*) in the *y* direction versus frequency in Hertz due to the sum of Lorentz and magnetization forces from a transverse magnetic field with a weak gradient, $a=0.1$, in the *y* direction for radius $R=0.5, 1.0$, and 1.5 cm with peak magnetic field strength of $|\mu_0 \hat{H}_o| = 0.5$ tesla.

4.5 Approximate Limits

We again see breakpoint in the non-dimensional plots of Figs. (7) and (9).

4.5.1 Small Skin-depth Limit, $\delta/R \ll 1$

Using the approximate small skin-depth forms in (35), the non-dimensional transverse field solutions approximately reduce to

$$\begin{aligned}
 \bar{C} &= \frac{CR}{\hat{H}_o} \approx \frac{-8je^{-(1+j)/\delta}}{(1-j)\delta\sqrt{\frac{(1-j)\delta}{\pi}}} \\
 \bar{D} &= \frac{D}{\hat{H}_o R^2} \approx -1 \\
 \bar{H} &= \frac{\bar{H}}{\hat{H}_o} \approx \frac{2\delta}{(1-j)\bar{r}^{3/2}} e^{(1+j)(\bar{r}-1)/\delta} \left[-\frac{(1-j)r}{\delta} \sin \phi \bar{i}_\phi - j \cos \phi \bar{i}_r \right] \quad 0 < r < R \\
 \bar{J}_z &= \frac{\bar{J}_z R}{\hat{H}_o} \approx -\frac{4 \sin \phi}{(1-j)\delta\sqrt{\bar{r}}} e^{(1+j)(\bar{r}-1)/\delta} \quad 0 < r < R \\
 \langle \bar{P} \rangle &= \frac{\langle P \rangle \sigma}{\pi |\hat{H}_o|^2} \approx \frac{2}{\delta} \\
 \langle \bar{f}_{Ly} \rangle &= \frac{\langle f_{Ly} \rangle}{\pi a \mu R |\hat{H}_o|^2} \approx -\frac{3}{2} \\
 \langle \bar{f}_{My} \rangle &= \frac{\langle f_{My} \rangle}{\pi a \mu R |\hat{H}_o|^2} \approx \frac{3(\mu - \mu_o)}{2\mu} \\
 \langle \bar{f}_y \rangle &= \langle \bar{f}_{Ly} \rangle + \langle \bar{f}_{My} \rangle \approx -\frac{3\mu_o}{2\mu}
 \end{aligned} \tag{60}$$

We can approximately check these results by realizing that for small skin-depth, the magnetic field just outside the cylinder is approximately the same as if the cylinder were perfectly conducting. Then the predominant magnetic field should be tangential

$$\vec{H}(r = R) \approx -2\hat{H}_o \sin \phi \vec{i}_\phi \quad (61)$$

and the current density is

$$|\hat{J}_z| \approx \left| \frac{\hat{H}_\phi}{\delta} \right| = \frac{2|\hat{H}_o| \sin \phi}{\delta} \quad (62)$$

The time average dissipated power unit length is then

$$\langle P \rangle \approx \frac{1}{2} \int \frac{|J_z|^2 \delta R d\phi}{\sigma} \approx \frac{2\pi R |\hat{H}_o|^2}{\sigma \delta} \quad (63)$$

in agreement with (60).

4.5.2 Large Skin-depth Limit, $\delta/R \gg 1$

Using the approximate large skin-depth forms in (40), the non-dimensional transverse field solutions approximately reduce to

$$\begin{aligned} \tilde{C} &= \frac{CR}{\hat{H}_o} \approx -\frac{8j\mu_o}{\delta(1-j)(\mu + \mu_o)} \left[1 - \frac{j(3\mu_o + \mu)}{4\delta^2(\mu + \mu_o)} \right] \\ \tilde{D} &= \frac{D}{\hat{H}_o R^2} \approx \frac{(\mu - \mu_o)}{(\mu + \mu_o)} - \frac{j\mu\mu_o}{\delta^2(\mu + \mu_o)^2} \\ \tilde{H}_r &= \frac{\hat{H}_r}{\hat{H}_o} \approx \frac{2\mu_o}{(\mu + \mu_o)} \left[1 + \frac{j}{4\delta^2} \left(\tilde{r}^2 - \frac{3\mu_o + \mu}{(\mu_o + \mu)} \right) \right] \cos \phi \\ \tilde{H}_\phi &= \frac{\hat{H}_\phi}{\hat{H}_o} \approx -\frac{\mu_o}{(\mu + \mu_o)} \left[2 + \frac{j}{2\delta^2} \left(3\tilde{r}^2 - \frac{3\mu_o + \mu}{(\mu_o + \mu)} \right) \right] \sin \phi \\ \tilde{J}_z &= \frac{\hat{J}_z R}{\hat{H}_o} \approx \frac{-2j\mu_o \tilde{r}}{\delta^2(\mu + \mu_o)} \left[2 + \frac{j}{2\delta^2} \left(\tilde{r}^2 - \frac{3\mu_o + \mu}{(\mu_o + \mu)} \right) \right] \sin \phi \\ \langle \tilde{P} \rangle &= \frac{\langle P \rangle \sigma}{\pi |\hat{H}_o|^2} \approx \frac{2\mu_o^2}{\delta^4(\mu + \mu_o)^2} \\ \langle \tilde{f}_{Ly} \rangle &= \frac{\langle f_{Ly} \rangle}{\pi a \mu R |\hat{H}_o|^2} \approx -\frac{3\mu_o^2}{5\delta^4(\mu + \mu_o)^2} \\ \langle \tilde{f}_{My} \rangle &= \frac{\langle f_{My} \rangle}{\pi a \mu R |\hat{H}_o|^2} \approx \frac{3\mu_o^2(\mu - \mu_o)}{\mu(\mu + \mu_o)^2} \end{aligned} \quad (64)$$

These results can be checked by realizing that when $\delta/R \gg 1$ the predominant \vec{H} field in the cylinder is just due to the applied magnetic field. Then applying the integral form of Faraday's law to a z directed rectangular contour at r and angle ϕ we obtain

$$\hat{J}_z = \sigma \hat{E}_z(r) = \frac{-2j\omega\mu\sigma\mu_o r}{\mu + \mu_o} \sin \phi \hat{H}_o = -\frac{4j}{\delta^2} \frac{\mu_o}{\mu + \mu_o} r \sin \phi \hat{H}_o \quad (65)$$

which is the dominant current density term in (64). The dissipated power per unit axial length is then

$$\begin{aligned} \langle P \rangle &= \frac{1}{2} \int_{r=0}^R \int_{\phi=0}^{2\pi} \frac{|\hat{J}_z|^2}{\sigma} r dr d\phi \\ &= \frac{8\mu_o^2 |\hat{H}_o|^2}{\sigma \delta^4 (\mu + \mu_o)^2} \int_{r=0}^R \int_{\phi=0}^{2\pi} r^3 \sin^2 \phi dr d\phi \\ &= \frac{2\pi\mu_o^2 R^4 |\hat{H}_o|^2}{\sigma \delta^4 (\mu + \mu_o)^2} \end{aligned} \quad (66)$$

in agreement with (64).

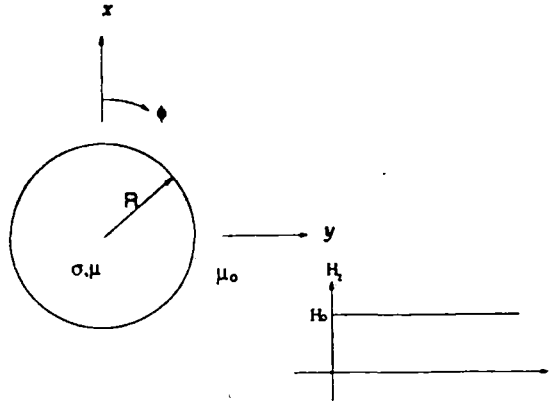


Figure 11: A cylinder of radius R , ohmic conductivity σ , and magnetic permeability μ is placed in a uniform z directed magnetic field that is parallel to the cylinder axis and stepped on at $t = 0$.

5 Step Change in Axial Magnetic Field

5.1 Turn-on Transient

Figure (11) shows an axial magnetic field that is instantaneously stepped on at time $t = 0$ to an amplitude H_o . The magnetic field in the cylinder is also axially directed for all time and can be expressed in the form

$$H_z(r, t) = H_o + \hat{H}(r)e^{-\alpha t} \quad (67)$$

where we recognize that in the steady state the magnetic field in the cylinder approaches the applied magnetic field. The magnetic field diffusion rate α is not yet known. Substituting the assumed form of solution of (67) into the magnetic diffusion equation of (4) gives

$$r^2 \frac{d^2 \hat{H}}{dr^2} + r \frac{d\hat{H}}{dr} + \alpha \sigma \mu r^2 \hat{H} = 0 \quad (68)$$

with solution that is finite at $r = 0$

$$\hat{H}(r) = A J_o(\sqrt{\alpha \sigma \mu} r) \quad (69)$$

At $r = R$, the tangential component of \vec{H} must be continuous so that $H_z(r = R, t) = H_o$, which then requires that $\hat{H}(r = R) = 0$. This requires that

$$\sqrt{\alpha \sigma \mu} R = \beta_n \quad (70)$$

where β_n is a zero of the zeroth order Bessel function, $J_o(\beta_n) = 0$, for which values are given in Table 2. Thus there are an infinite number of α 's and we can write the most general form of solution as

$$H_z(r, t) = H_o + \sum_{n=1}^{\infty} A_n J_o(\beta_n r/R) e^{-\alpha_n t} \quad (71)$$

where

$$\alpha_n = \beta_n^2 / (\sigma \mu R^2) \quad (72)$$

To find the amplitudes A_n , we use the initial condition at $t = 0$ that the magnetic field in the cylinder is zero

$$H_z(r, t = 0) = 0 = H_o + \sum_{n=1}^{\infty} A_n J_o(\beta_n r/R) \quad (73)$$

Table 2: Zeroes of the Zeroth Order Bessel Function, $J_0(\beta_n) = 0$.

n	β_n	n	β_n	n	β_n	n	β_n
1	2.40482	6	18.07106	11	33.77582	16	49.48261
2	5.52008	7	21.21164	12	36.91710	17	52.62405
3	8.65373	8	24.35247	13	40.05843	18	55.76551
4	11.79153	9	27.49348	14	43.19979	19	58.90698
5	14.93092	10	30.63461	15	46.34119	20	62.04847

$$\lim_{n \text{ large}} \beta_n \approx (n - 0.25)\pi$$

Using the orthogonality condition for Bessel functions that

$$\int_0^R r J_0(\beta_m r/R) J_0(\beta_n r/R) dr = \begin{cases} 0 & m \neq n \\ \frac{R^2}{2} J_1^2(\beta_m) & m = n \end{cases} \quad (74)$$

we solve (73) for A_n as

$$A_n = \frac{-2H_o}{\beta_n J_1(\beta_n)} \quad (75)$$

so that the magnetic field and current density are

$$\begin{aligned} H_z(r, t) &= H_o \left[1 - 2 \sum_{n=1}^{\infty} \frac{J_0(\beta_n r/R)}{\beta_n J_1(\beta_n)} e^{-\beta_n^2 t/\tau} \right] \\ J_\phi(r, t) &= -\frac{\partial H_z}{\partial r} = -\frac{2H_o}{R} \sum_{n=1}^{\infty} \frac{J_1(\beta_n r/R)}{\beta_n J_1(\beta_n)} e^{-\beta_n^2 t/\tau} \end{aligned} \quad (76)$$

where $\tau = \sigma \mu R^2$. The dissipated power per unit length is then

$$P = \int_0^R \frac{J_\phi^2}{\sigma} 2\pi r dr = \frac{8\pi H_o^2}{\sigma R^2} \int_0^R \left[\sum_{n=1}^{\infty} \frac{J_1(\beta_n r/R)}{J_1(\beta_n)} e^{-\beta_n^2 t/\tau} \right]^2 r dr \quad (77)$$

and the total dissipated energy per unit length is

$$W = \int_0^{\infty} P dt \quad (78)$$

The magnetization and Lorentz forces per unit length for a slightly non-uniform magnetic field as given by (14) are obtained from (9) and (13) as

$$\vec{f}_M = \frac{1}{2} (\mu - \mu_o) H_o^2 R \int_{\phi=0}^{2\pi} [1 + a \sin \phi]^2 [\vec{i}_x \cos \phi + \vec{i}_y \sin \phi] d\phi = (\mu - \mu_o) H_o^2 \pi R a \vec{i}_y \quad (79)$$

$$\begin{aligned} \vec{f}_L &= \int_{r=0}^R \int_{\phi=0}^{2\pi} \mu J_\phi(r, t) H_z(r, t) [1 + a \sin \phi]^2 [\cos \phi \vec{i}_x + \sin \phi \vec{i}_y] r dr d\phi \\ &= \vec{i}_y \int_{r=0}^R 2\pi a \mu J_\phi(r, t) H_z(r, t) r dr \\ &= -\frac{4\pi a \mu H_o^2}{R} \vec{i}_y \int_{r=0}^R \left[\sum_{n=1}^{\infty} \frac{J_1(\beta_n r/R)}{J_1(\beta_n)} e^{-\alpha_n t} \right] \left[1 - 2 \sum_{n=1}^{\infty} \frac{J_0(\beta_n r/R)}{\beta_n J_1(\beta_n)} e^{-\alpha_n t} \right] r dr \end{aligned} \quad (80)$$

To evaluate (79) and (80) it is necessary to take a sufficient number of terms in the infinite series so that the remaining terms give a negligible contribution. To examine this convergence, Table 3 lists the non-dimensional dissipated energy per unit length, $\tilde{W} = W\sigma/(\pi H_o^2 \tau)$, versus the number of terms n taken in the infinite series. We see very little difference as n goes from 5 to 10 to 20.

Table 3: Non-dimensional dissipated energy per unit length, $\bar{W} = W\sigma/(\pi H_o^2\tau)$, versus the number of terms n taken in the infinite series.

n	\bar{W}
1	0.345829
2	0.411466
5	0.461528
10	0.480247
20	0.489995

5.2 Turn-off Transient

After a time T , the magnetic field is turned off. The initial and boundary conditions are then

$$\begin{aligned} H_z(r=R, t > T) &= 0 \\ H_z(r, t=T) &= H_o \left[1 - 2 \sum_{n=1}^{\infty} \frac{J_o(\beta_n r/R)}{\beta_n J_1(\beta_n)} e^{-\beta_n^2 T/\tau} \right] \end{aligned} \quad (81)$$

For $t > T$ we thus take a solution of the form

$$H_z(r, t) = \hat{H}(r) e^{-\alpha(t-T)} \quad (82)$$

where the solution form is again given by (69) and (70)

$$H_z(r, t) = \sum_{n=1}^{\infty} A_n J_o(\beta_n r/R) e^{-\alpha_n(t-T)} \quad (83)$$

The amplitudes A_n are found using (81) and the orthogonality of Bessel functions of (74)

$$A_n = \frac{2}{R^2 J_1^2(\beta_n)} \int_{r=0}^R H_z(r, t=T) J_o(\beta_n r/R) r dr \quad (84)$$

The current density is then

$$J_\phi(r, t) = -\frac{\partial H_z}{\partial r} = -\sum_{n=1}^{\infty} \frac{A_n \beta_n}{R} J_1(\beta_n r/R) e^{-\alpha_n(t-T)} \quad (85)$$

The dissipated power, energy, and Lorentz force per unit length are given by the general forms in (77)-(80). The magnetization force is zero for $t > T$ as the magnetic field at the $r = R$ interface is zero. If $T \gg \tau$, the magnetic field distribution in (76) has essentially reached the steady state distribution of $H_z(r, t \rightarrow \infty) = H_o$ so that $H_z(r, t=T) \approx H_o$ in (81). Then (84) becomes

$$A_n \approx \frac{2H_o}{R^2 J_1^2(\beta_n)} \int_{r=0}^R J_o(\beta_n r/R) r dr \approx \frac{2H_o}{\beta_n J_1(\beta_n)} \quad (86)$$

and the solutions for $t > T$ are

$$\begin{aligned} H_z(r, t) &= 2H_o \sum_{n=1}^{\infty} \frac{J_o(\beta_n r/R)}{\beta_n J_1(\beta_n)} e^{-\beta_n^2(t-T)/\tau} \\ J_\phi(r, t) &= -\frac{2H_o}{R} \sum_{n=1}^{\infty} \frac{J_1(\beta_n r/R)}{J_1(\beta_n)} e^{-\beta_n^2(t-T)/\tau} \\ P &= \frac{8\pi H_o^2}{\sigma R^2} \int_{r=0}^R \left[\sum_{n=1}^{\infty} \frac{J_1(\beta_n r/R)}{J_1(\beta_n)} e^{-\beta_n^2(t-T)/\tau} \right]^2 r dr \\ W &= \int_{t=0}^T P(0 < t < T) dt + \int_{t=T}^{\infty} P(t > T) dt \end{aligned} \quad (87)$$

5.3 Impulse Response

The other extreme limit is that the magnetic field has duration T much less than the magnetic relaxation time τ , $T \ll \tau$. The limiting case is that $T \rightarrow 0$ while $H_o T$ remains finite so that the imposed magnetic field can be considered a time impulse $H_o T \delta(t)$. Then the solutions for magnetic field and current distributions will be the time derivative of (76) replacing H_o by $H_o T$.

$$\begin{aligned} H_z(r, t) &= -\frac{2H_o T}{\tau} \sum_{n=1}^{\infty} \frac{\beta_n J_o(\beta_n r/R)}{J_1(\beta_n)} e^{-\beta_n^2 t/\tau} \\ J_\phi(r, t) &= \frac{2H_o T}{R\tau} \sum_{n=1}^{\infty} \frac{\beta_n^2 J_1(\beta_n r/R)}{J_1(\beta_n)} e^{-\beta_n^2 t/\tau} \end{aligned} \quad (88)$$

The dissipated power, energy, and Lorentz force per unit length are then given by the general forms in (77), (78), and (80). The magnetization force per unit length of (79) would then be an impulse.

6 Step Change In Transverse Magnetic Field

6.1 General Solutions

A transverse x directed electric field is instantaneously stepped on at time $t = 0$ to an amplitude H_o . The solutions have a steady state part and a transient part that dies out with time. The steady state current density is zero so the general form for the current density is

$$J_z(r, \phi, t) = \hat{J}_z(r, \phi) e^{-\alpha t} \quad (89)$$

which when substituted into (5) gives

$$\frac{1}{r} \frac{\partial}{\partial r} \left(r \frac{\partial \hat{J}_z}{\partial r} \right) + \frac{1}{r^2} \frac{\partial^2 \hat{J}_z}{\partial \phi^2} = -\alpha \mu \sigma \hat{J}_z \quad (90)$$

The general product solution that is finite at $r = 0$ is

$$J_z(r, \phi) = J_m(\sqrt{\alpha \mu \sigma} r) [A_1 \sin m\phi + A_2 \cos m\phi] \quad (91)$$

However, the uniform x directed magnetic field only excites the $m = 1$ solution with $A_2 = 0$ so that the current density is of the form

$$J_z(r, \phi, t) = A J_1(\sqrt{\alpha \mu \sigma} r) \sin \phi e^{-\alpha t} \quad (92)$$

The magnetic field solution in the cylinder for $r < R$ is obtained from Faraday's law

$$\frac{\partial \vec{H}}{\partial t} = -\frac{1}{\mu \sigma} \nabla \times \vec{J} \quad (93)$$

while the magnetic field outside the cylinder for $r > R$ is obtained from a scalar or z directed vector potential that obeys Laplace's equation. The radial and ϕ components of \vec{H} for steady state and transients are thus of the form

$$H_r(r, \phi, t) = \begin{cases} \left[\frac{A}{\alpha \mu \sigma} J_1(\sqrt{\alpha \mu \sigma} r) e^{-\alpha t} + \frac{2\mu_o H_o}{\mu + \mu_o} \right] \cos \phi & r < R \\ \left[\frac{C e^{-\alpha t}}{r^2} + H_o \left[1 + \frac{R^2(\mu - \mu_o)}{r^2(\mu + \mu_o)} \right] \right] \cos \phi & r > R \end{cases} \quad (94)$$

$$H_\phi(r, \phi, t) = \begin{cases} \left[-\frac{A}{\alpha \mu \sigma} \left[\sqrt{\alpha \mu \sigma} J_o(\sqrt{\alpha \mu \sigma} r) - \frac{1}{r} J_1(\sqrt{\alpha \mu \sigma} r) \right] e^{-\alpha t} - \frac{2\mu_o H_o}{\mu + \mu_o} \right] \sin \phi & r < R \\ \left[\frac{C e^{-\alpha t}}{r^2} - H_o \left[1 - \frac{R^2(\mu - \mu_o)}{r^2(\mu + \mu_o)} \right] \right] \sin \phi & r > R \end{cases} \quad (95)$$

6.2 Boundary Conditions

The steady state solutions already satisfy continuity of tangential \vec{H} and normal \vec{B} at $r = R$. The transient solutions must also obey these boundary conditions for which we obtain

$$\begin{aligned} H_\phi(r = R_+) = H_\phi(r = R_-) &\Rightarrow \frac{C}{R^2} = -\frac{A}{\alpha\mu\sigma} [\sqrt{\alpha\mu\sigma} J_0(\sqrt{\alpha\mu\sigma} R) - \frac{1}{R} J_1(\sqrt{\alpha\mu\sigma} R)] \\ \mu_o H_r(r = R_+) = \mu H_r(r = R_-) &\Rightarrow \frac{\mu_o C}{R^2} = \frac{A}{\alpha\sigma R} J_1(\sqrt{\alpha\mu\sigma} R) \end{aligned} \quad (97)$$

which for non-zero values of A and C require that

$$\mu_o \sqrt{\alpha\mu\sigma} R J_0(\sqrt{\alpha\mu\sigma} R) + (\mu - \mu_o) J_1(\sqrt{\alpha\mu\sigma} R) = 0 \quad (98)$$

This relation then determines allowed values of α which we denote as α_n with corresponding amplitudes A_n and C_n related through either of the relations in (97). Note that because

$$J_0(\beta) = \frac{dJ_1}{d\beta} + \frac{1}{\beta} J_1(\beta) \quad (99)$$

that (98) can be written as

$$\mu J_1(\beta) + \mu_o \beta \frac{dJ_1}{d\beta} = 0, \quad \beta = \sqrt{\alpha\mu\sigma} R \quad (100)$$

If the infinite number of solutions to (100) are denoted as β_n , then a Bessel function orthogonality relation is

$$\int_0^1 \left(\frac{r}{R}\right) J_1(\beta_n r/R) J_1(\beta_m r/R) \left(\frac{dr}{R}\right) = \begin{cases} 0 & m \neq n \\ \frac{1}{2\beta_n^2} \left[\frac{\mu^2}{\mu_o^2} + \beta_n^2 - 1\right] J_1^2(\beta_n) & m = n \end{cases} \quad (101)$$

The general form of solution for the current density of (93) is

$$J_z(r, \phi, t) = \sum_{n=1}^{\infty} A_n J_1(\beta_n r/R) e^{-\beta_n^2 t/R} \sin \phi \quad (102)$$

The coefficients A_n can be obtained using the orthogonality condition of (101) with the initial condition that at $t = 0$, all the current flows as a surface current at $r = R$ and is thus a spatial impulse at $r = R$

$$J_z(r, \phi, t = 0) = -2H_o \sin \phi \delta(r - R) = \sum_{n=1}^{\infty} A_n J_1(\beta_n r/R) \sin \phi \quad (103)$$

Multiplying both sides by $(r/R) J_1(\beta_m r/R)$ and integrating over $d(r/R)$ let's us solve for A_n

$$\int_0^1 -\frac{H_o r}{R} J_1(\beta_m r/R) \delta(r - R) \frac{dr}{R} = -H_o J_1(\beta_m) = \frac{A_m}{2\beta_m^2} \left[\frac{\mu^2}{\mu_o^2} + \beta_m^2 - 1\right] J_1^2(\beta_m) \quad (104)$$

as

$$A_n = -\frac{4\beta_n^2 H_o}{R \left[\frac{\mu^2}{\mu_o^2} + \beta_n^2 - 1\right] J_1(\beta_n)} \quad (105)$$

6.3 Dissipated Power per unit length

To summarize the procedure, β_n must be found by numerically solving (100). Then A_n is found from (105) and the current density is found from (102). The dissipated power per unit length is given by

$$\begin{aligned} P &= \int_{r=0}^R \int_{\phi=0}^{2\pi} \frac{J^2}{\sigma} r dr d\phi \\ &= \frac{1}{\sigma} \int_{r=0}^R \int_{\phi=0}^{2\pi} \left[\sum_{n=1}^{\infty} A_n J_1(\beta_n r/R) e^{-\beta_n^2 t/\tau} \right]^2 \sin^2 \phi r dr d\phi \\ &= \frac{\pi}{\sigma} \int_{r=0}^R \left[\sum_{n=1}^{\infty} A_n J_1(\beta_n r/R) e^{-\beta_n^2 t/\tau} \right]^2 r dr \end{aligned} \quad (106)$$

6.4 Magnetization Force per unit length

At the interface we have from (95) and (96)

$$\begin{aligned} H_\phi(r = R, \phi, t) &= \left[\sum_{n=1}^{\infty} \frac{C_n}{R^2} e^{-\beta_n^2 t / \tau} - \frac{2\mu_o H_o}{(\mu + \mu_o)} \right] \sin \phi = H_\phi(t) \sin \phi \\ B_r(r = R, \phi, t) &= \left[\sum_{n=1}^{\infty} \frac{\mu_o C_n}{R^2} e^{-\beta_n^2 t / \tau} + \frac{2\mu\mu_o H_o}{(\mu + \mu_o)} \right] \cos \phi = B_r(t) \cos \phi \end{aligned} \quad (107)$$

where we separate out the time and ϕ dependences and from (97)

$$C_n = \frac{\mu A_n R^3 J_1(\beta_n)}{\mu_o \beta_n^2} \quad (108)$$

From (13) and assumed weak gradient field of (14) the magnetization force per unit length is

$$\vec{f}_M = \frac{R}{2} \int_{\phi=0}^{2\pi} [(\mu - \mu_o) H_\phi^2(t) \sin^2 \phi + \left(\frac{1}{\mu_o} - \frac{1}{\mu} \right) B_r^2(t) \cos^2 \phi] [1 + a \sin \phi]^2 [\vec{i}_x \cos \phi + \vec{i}_y \sin \phi] d\phi \quad (109)$$

Performing the ϕ integration gives

$$f_{M_y} = \frac{\pi R a}{4} \left[3(\mu - \mu_o) H_\phi^2(t) + \left(\frac{1}{\mu_o} - \frac{1}{\mu} \right) B_r^2(t) \right] \quad (110)$$

6.5 Lorentz force per unit length

From (57), the Lorentz force per unit length is

$$\begin{aligned} \vec{f}_L &= \int_{r=0}^R \int_{\phi=0}^{2\pi} J_z(r, t) \sin \phi [B_r(r, t) \cos \phi (-\sin \phi \vec{i}_x + \cos \phi \vec{i}_y) - \mu H_\phi(r, t) \sin \phi (\cos \phi \vec{i}_x + \sin \phi \vec{i}_y)] [1 + a \sin \phi]^2 r dr d\phi \\ &= \frac{\pi a}{2} \int_{r=0}^R J_z(r, t) [B_r(r, t) - 3\mu H_\phi(r, t)] r dr \end{aligned} \quad (111)$$

Finite Element Modeling of Rebar For Electromagnetic Analyses

28 July 1994

J. R. Hale, J. Feng, R. D. Pillsbury, Jr.

This document and all reports and memoranda in this series are intended as a record of work in progress. They are for use in informal discussions of design, fabrication, and further computation alternatives. This material is subject to change and should not, therefore, be published or referred to in the open literature. Conclusions are preliminary and distribution should be strictly limited.

Massachusetts Institute of Technology
Plasma Fusion Center
Cambridge MA 02139

MEMORANDUM

Date: 28 July 1994
To: R. D. Thornton
From: J. R. Hale, J. Feng, R. D. Pillsbury, Jr.
Subject: Memo PFC-RM-001, rebar project

Finite Element Modeling of Rebar For Electromagnetic Analyses

One of the fundamental questions to be answered before preparing a finite element model for numeric calculation of eddy current losses in rebars was the extent to which the results might be compromised by modeling a single isolated bar only, rather than modeling an entire two or three dimensional grid of rebars. To answer this question, the computer code MAP[1] was employed to carry out a series of runs, calculating the flux density perturbations induced in a uniform applied field by the presence of a single isolated rebar, 0.625" in diameter. A uniform field was applied as a single-cycle sinusoid, with peak flux densities ranging from 0.05 T to 0.5 T. A non-linear $B-H$ curve for carbon steel is internal to the computer program.

Figure 1 is a plot of magnetic flux lines in and around the rebar for the case in which the applied field is perpendicular to the rebar. Note that the flux pattern within the rebar is different from what it would be in the static applied field case: induced eddy currents produce a flux pattern of their own that are summed with the induced magnetic moment in the material. Figure 2 is a plot of magnetic flux lines out to 20 rebar diameters, at the moment when the applied field wave form is at its peak. It is evident from this figure that beyond a few diameters, the presence of the rebar is not discernible in the uniformity of the flux lines.

Figure 3 is a plot of flux density vs distance along a radius, from which one can quantify the field perturbation: beyond five rebar diameters, the flux density is essentially undisturbed. Inasmuch as the spacing between rebars in maglev structures would typically be greater than five diameters, we believe that for the purposes of this project, calculations of eddy current losses can be carried out without the need to model two or three dimensional grids, for at the spacings typical of such grids, the field at any rebar will not be altered by perturbations due to its neighbors. A consequence of this result will be a significant saving of time and effort in further calculations.

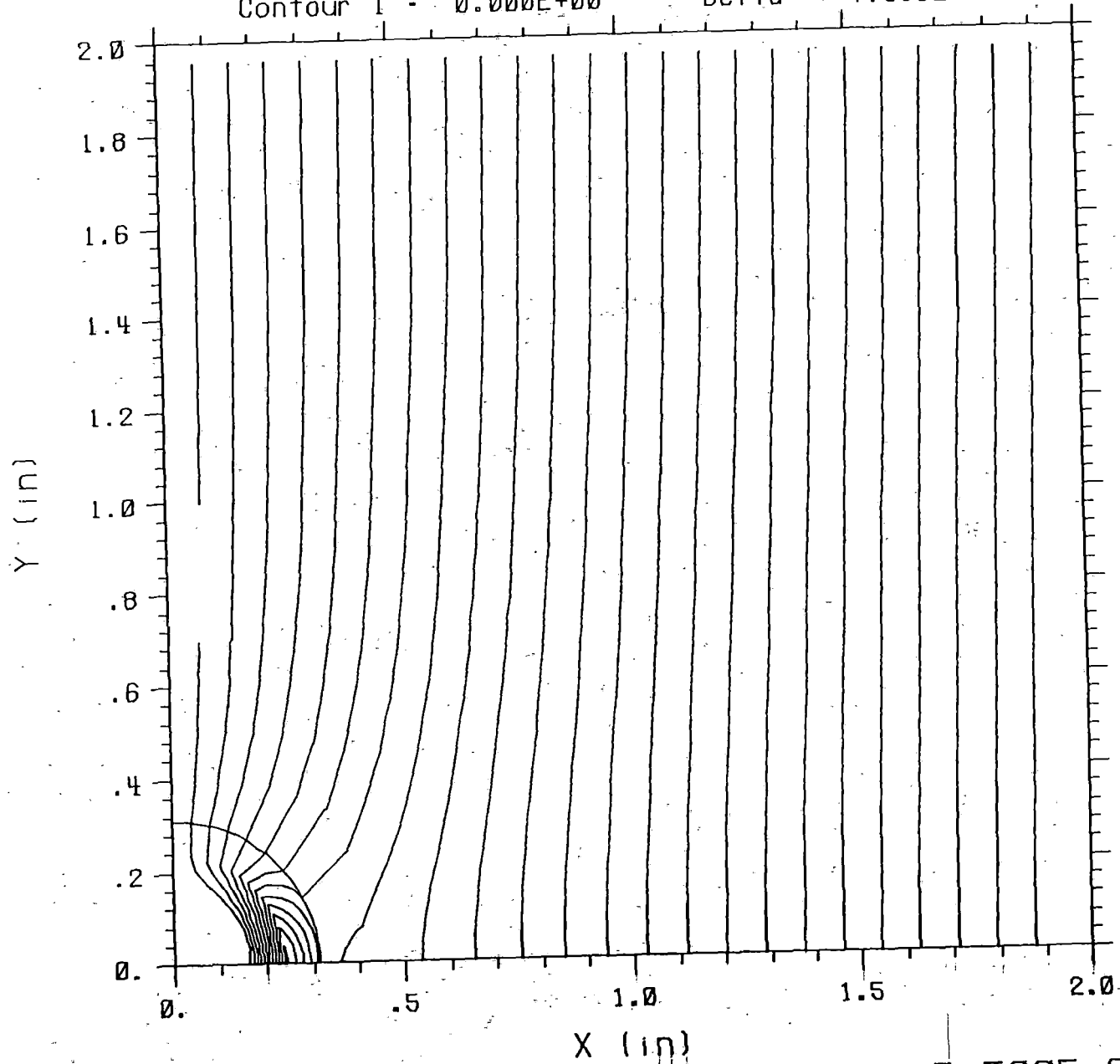
References

1. R. D. Pillsbury, Jr., "MAP User's Manual", PFC/RR-91-5, Plasma Fusion Center, MIT, December, 1991.

ISOLATED REBAR ANALYSIS - 62 Hz sine

MITMAP V1.0 6/16/94 11:12

Contour 1 - 0.000E+00 Delta - 7.818E-05



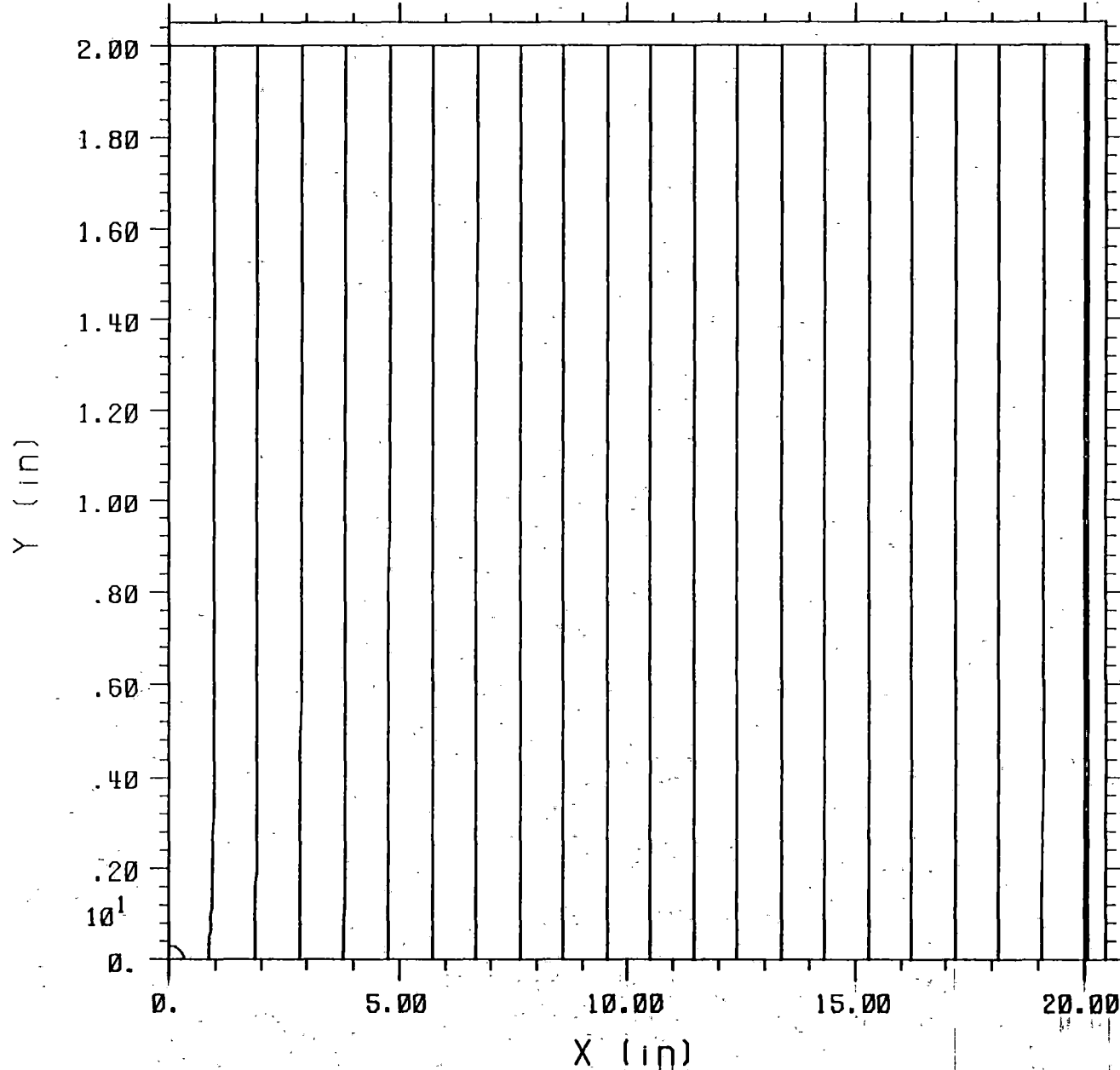
CONTOURS OF AZ

- TIME = 7.500E-03

ISOLATED REBAR ANALYSIS - 62 Hz sine

MITMAP V1.0 6/16/94 10: 1

Contour 1 - -1.595E-07 Delta - 4.853E-03



CONTOURS OF Az

- TIME - 4.000E-03

ISOLATED REBAR ANALYSIS - 62 Hz sine

MITMAP V1.0 6/20/94 14:53

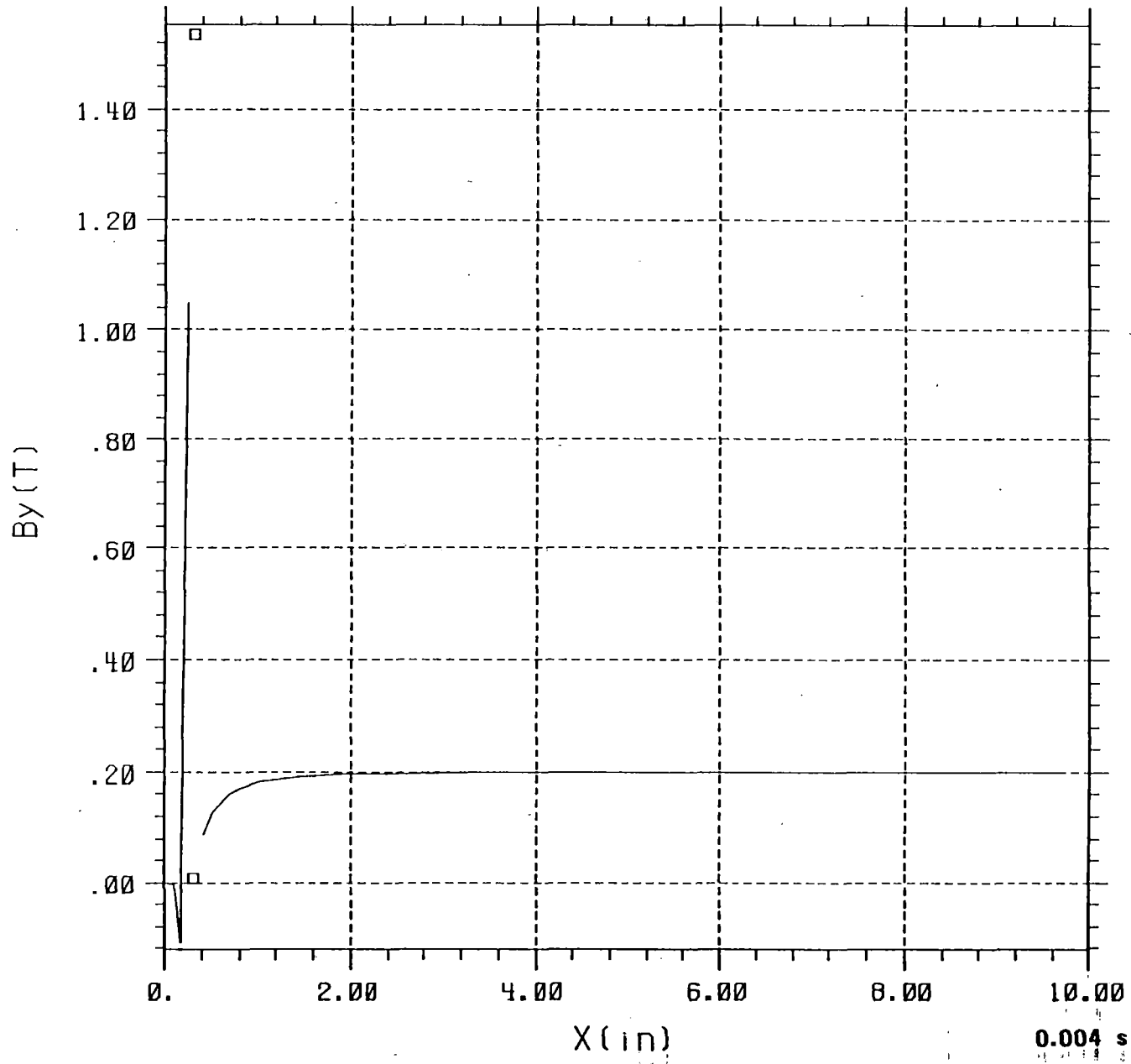


Figure 3

Eddy Current Losses in Rebar: Benchmarking Two Independent Methods

28 July 1994

J. R. Hale, J. Feng, R. D. Pillsbury, Jr.

This document and all reports and memoranda in this series are intended as a record of work in progress. They are for use in informal discussions of design, fabrication, and further computation alternatives. This material is subject to change and should not, therefore, be published or referred to in the open literature. Conclusions are preliminary and distribution should be strictly limited.

Massachusetts Institute of Technology
Plasma Fusion Center
Cambridge MA 02139

MEMORANDUM

Date: 28 July 1994
To: R. D. Thornton
From: J. R. Hale, J. Feng, R. D. Pillsbury, Jr.
Subject: Memo PFC-RM-002, Rebar Project

Eddy Current Losses in Rebar: Benchmarking Two Independent Methods

One of the collaborators in this project has derived a set of equations with which one can calculate eddy current losses in rebar. The methods in use at PFC, on the other hand, are based on finite element modeling, and numeric solutions by use of several computer codes available at PFC. In such a collaboration as this, it is prudent to benchmark the different methods against one another, first to cross check for accuracy, and second, to highlight differences in results, if any, that may arise because of limitations in scope inherent in a given method, or because of simplifying assumptions made in either one.

We have prepared finite element models of a single isolated rebar, using the same dimensions and material properties that were used for the examples presented by Zahn, et.al.[1]. Eddy current dissipation in a steady-state sinusoidal applied magnetic field was calculated. At the PFC, the code ACMAP[2] was utilized to run these cases. Table 1 summarizes the problem parameters:

Material	mild (carbon) steel
Diameter of cylindrical sample (m)	0.02
Electrical resistivity ($\Omega\text{-m}$)	1.18×10^{-7}
Relative magnetic permeability (constant)	5000
Peak applied field, $\mu_0 H_0$ (T)	0.5

Table 1

Figures 1 and 2 are reproductions of plots generated by our colleagues[1], in which they show eddy current dissipation in an isolated cylinder for the cases of an uniform axial and uniform perpendicular applied field, respectively. The results of our finite element numeric calculations are overplotted on these curves with x's: the agreement is excellent. We note that for the higher frequency points, it was necessary to make the finite element grid increasingly finer in order to better resolve the smaller skin depth.

- ◆ This demonstration of equivalent results, satisfactory though it is, must always be viewed within the context of any simplifying assumptions that have been made. One of the most vulnerable of which, we have since learned, is constant magnetic perme-

ability. This vulnerability will be described in a separate memorandum, in which we compare results calculated with ACMAP and a more general PFC code, MAP[2], that can take into account the true non-linear $B-H$ curve of a material.

Inasmuch as we will utilize MAP, rather than ACMAP, to calculate eddy current losses, one more benchmark exercise was carried out. We ran the same geometry as before with MAP, assuming a constant permeability and a steady-state sinusoidal applied field. The output duplicated that of the more limited and specialized ACMAP. Hence, we feel confident that MAP, too, could duplicate the results obtained from the formulations derived by Zahn, *for the same input conditions*.

References

1. M. Zahn, and R. Karmacharya, "Power Dissipation and Magnetic Forces on MAGLEV Rebars", Project Review Meeting, June 22, 1994.
2. R. D. Pillsbury, Jr., "MAP User's Manual", PFC/RR-91-5, Plasma Fusion Center, MIT, December, 1991.

Power Dissipation in Cylinder in Axial Magnetic Field

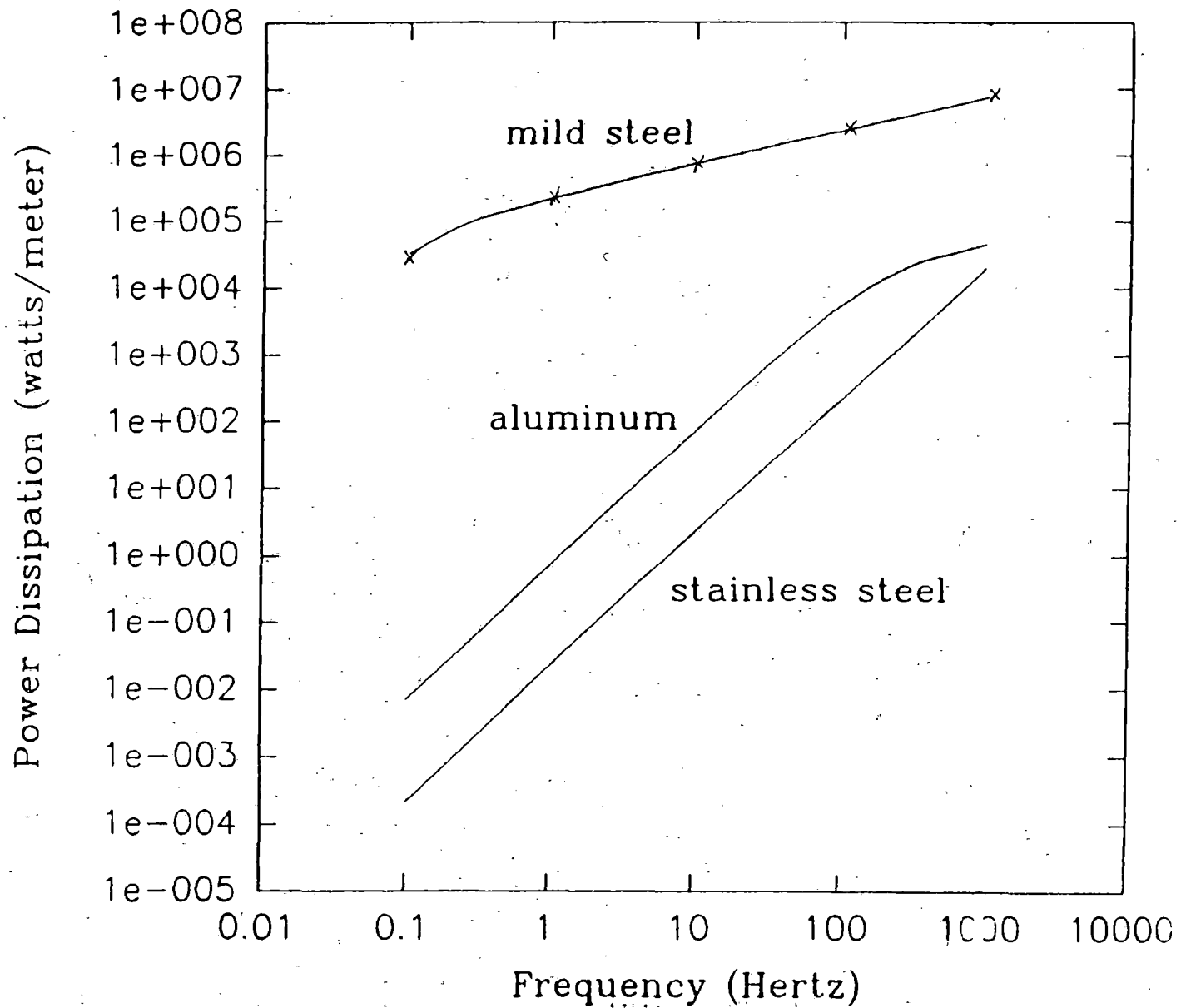


Figure 1

Power Dissipation in Cylinder in Transverse Magnetic Field

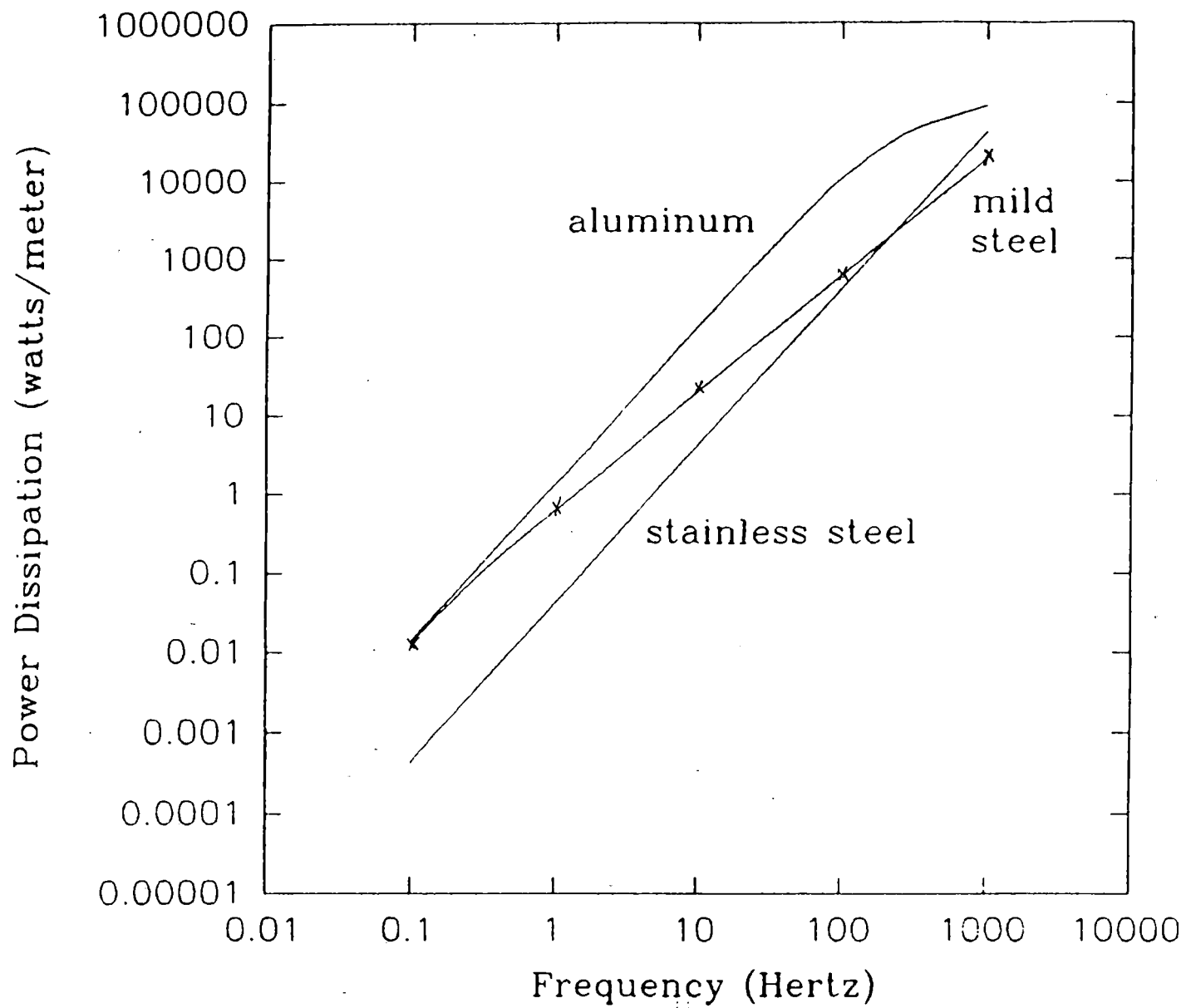


Figure 2

Eddy Current Losses: Comparison of Constant μ vs Non-Linear μ Results

28 July 1994

J. R. Hale, J. Feng, R. D. Pillsbury, Jr.

This document and all reports and memoranda in this series are intended as a record of work in progress. They are for use in informal discussions of design, fabrication and further computation alternatives. This material is subject to change and should not, therefore, be published or referred to in the open literature. Conclusions are preliminary and distribution should be strictly limited.

Massachusetts Institute of Technology
Plasma Fusion Center
Cambridge MA 02139

MEMORANDUM

Date: 28 July 1994
To: R. D. Thornton
From: J. R. Hale, F. Feng, R. D. Pillsbury, Jr.
Subject: Memorandum RM-003, Rebar Project

Eddy Current Losses: Comparison of Constant μ vs Non-Linear μ Results

In this memorandum, we will present a comparison of results generated by the finite element code MAP[1] for two classes of runs — constant μ , and non-linear μ . As described in a previous memo (PFC-RM-002), this code has been benchmarked against another PFC code, ACMAP[2], designed for use solely in steady-state a.c. problems, with constant permeability materials. MAP can duplicate these characteristics, and in addition can accommodate any non-linear $B-H$ material, and any applied field waveform, from d.c., to user-defined transient pulses, to intermittent and steady-state sinusoids. It was with MAP that the results described in this memorandum were generated.

Table 1 lists the physical parameters for the problem. Note that the value of 5000 was chosen for the constant μ calculations to be consistent with the discussion in an earlier memo (PCF-RM-002):

Material	mild (carbon) steel
Diameter of cylindrical rebar (m [in])	0.0159 [0.625]
Electrical resistivity (Ω -m)	1.0×10^{-7}
Relative magnetic permeability: For non-linear μ calculations For constant μ calculations	carbon steel $B-H$ curve 5000
Applied field	sinusoidal, 4 - 10 cycles

Table 1

Among the output data from the code are plots of total cumulative joule heating vs time. We have chosen to express the results in units of energy dissipated per unit length of rebar, per cycle of applied field. The total loss incurred during the passage of a single Maglev vehicle, then, could be computed on the basis of the configuration of the vehicle coils; a vehicle with many smaller coils would induce a greater number of cycles of loss, while a vehicle with fewer, but more intense field coils would produce fewer cycles of loss, but likely of greater magnitude each. Eddy current losses attributable to

leading and trailing transients would raise the total, to a greater or lesser amount depending upon the vehicle bogie/coil geometry. Table 2 summarizes these results:

$\mu_0 H_0$ (T)	f (Hz)	Perpend. Applied Field		Parallel Applied Field	
		const. μ	$\mu(H)$	const. μ	$\mu(H)$
0.05	15.5	0.0166	0.0132	557	33.5
0.05	64.0	0.0241	0.0272	287	25.2
0.50	15.5	1.66	7.52	55,700	152.7
0.50	64.0	2.41	23.6	28,700	313.4

Table 2. Eddy current losses comparison. Units are joules(m-cycle)⁻¹

The most apparent result is that, except for the low intensity perpendicular field cases, the calculated losses are quite different between the large constant μ and the non-linear μ cases. Note in particular:

- In the perpendicular field (higher intensity only) cases, the incorporation of non-linear permeability yields somewhat higher loss results than if a large constant μ is assumed.
- In the parallel field cases, the incorporation of non-linear permeability yields much lower loss rate than the large constant μ results would suggest.

For these examples (carbon steel), the use of a large constant value, 5000, for relative permeability yields a skin depth that is unrealistically small for most of the applied field waveform (in the high-field cases). Figure 1 shows the default $B-H$ curve for steel utilized by the code MAP over the range of magnetizing field appropriate for this project. Figure 2 plots the relative permeability characteristic of this material. It is apparent that in cases where the peak applied field is greater than a few tenths of a tesla, the material is near magnetic saturation for a significant fraction of the applied field waveform, and the relative permeability drops to less than 10.

To try to understand the apparent discrepancy shown in Table 2, consider the effect of permeability on skin depth. As an illustration, we'll make use of the example given by Zahn, et.al.[3]: relative permeability, $\mu/\mu_0 = 5000$; electrical conductivity, $\rho = 0.118 \mu\Omega\text{-m}$; rebar radius, $r = 0.01 \text{ m}$; frequency, $f = 60 \text{ Hz}$. Table 3 lists normalized skin depth, σ , as a function of different values of μ/μ_0 :

μ/μ_0	δ (mm)
5000	0.316
1000	0.707
100	2.23
10	7.07
5	10.0

Table 3. Variation of skin depth with permeability

Zahn presented two approximate limiting solutions, one for cases in which $\bar{\delta} = \delta/r \ll 1$, and one for $\bar{\delta} \gg 1$; in the former, the eddy current dissipation is proportional to $\bar{\delta}^{-1}$ and in the latter, it is proportional to $\bar{\delta}^{-4}$. But, for some of the field regimes of interest in this project, the data in Table 3 show that the skin depth is neither much smaller than, nor much larger than the radius (10 mm. in this example). Hence, a more accurate solution may lie somewhere between the two limiting solutions, but in all cases, a larger skin depth value in the calculation would yield smaller losses, in the direction toward closer agreement with the computer-generated results.

This finding presents us with a dilemma: the use of finite element computer codes will be less convenient for users of the final results of this project than the use of a few straight-forward equations that presume a constant permeability. And yet, such equations can lead to erroneous answers. Perhaps a "correction function" can be generated for use with the equations, to account for a variable μ . It likely would need to be a function of both the frequency and peak field for a given application, and of a given material's actual $B-H$ curve. The search for a compensating function such as this may be beyond the resources applicable to this project, but could be a topic for future work.

References

1. R. D. Pillsbury, Jr., "MAP User's Manual", PFC/RR-91-5, Plasma Fusion Center, MIT, December, 1991.
2. R. D. Pillsbury, Jr., Developmental code in use at Plasma Fusion Center, MIT.
3. M. Zahn, and R. Karmacharya, "Power Dissipation and Magnetic Forces on MAGLEV Rebars", Project Review Meeting, June 22, 1994.

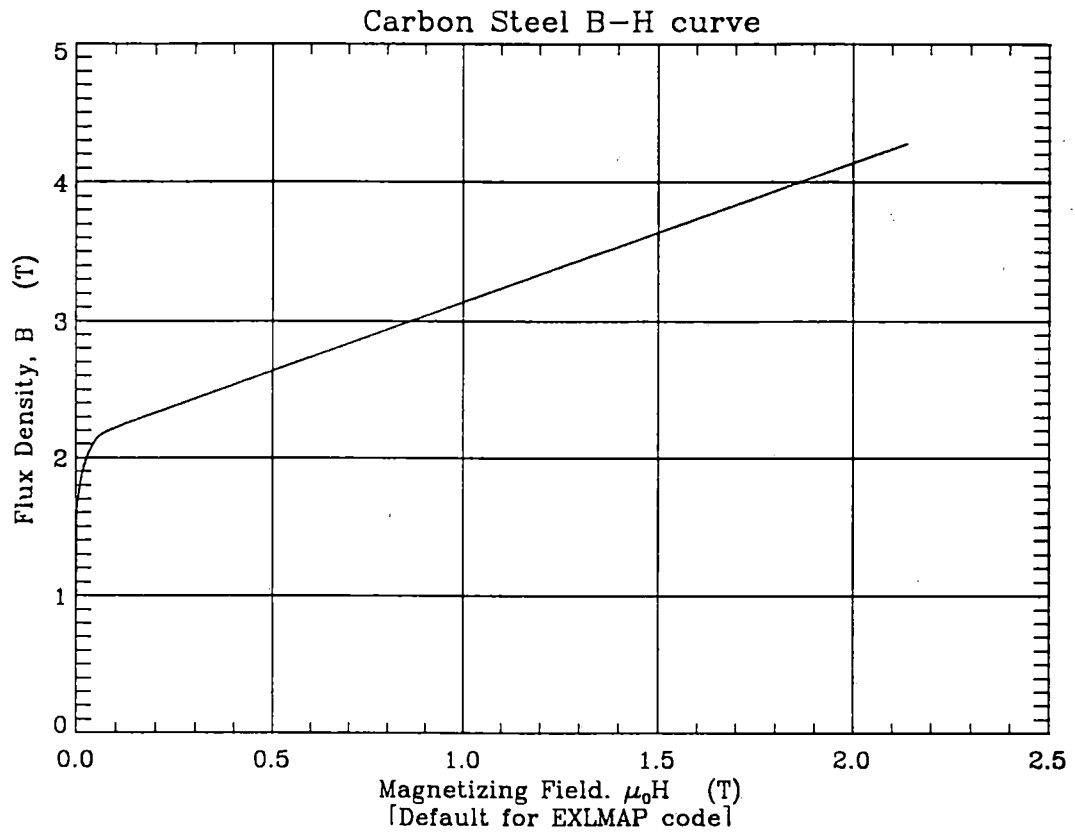


Figure 1. Default $B-H$ characteristic in MAP code; material: carbon steel

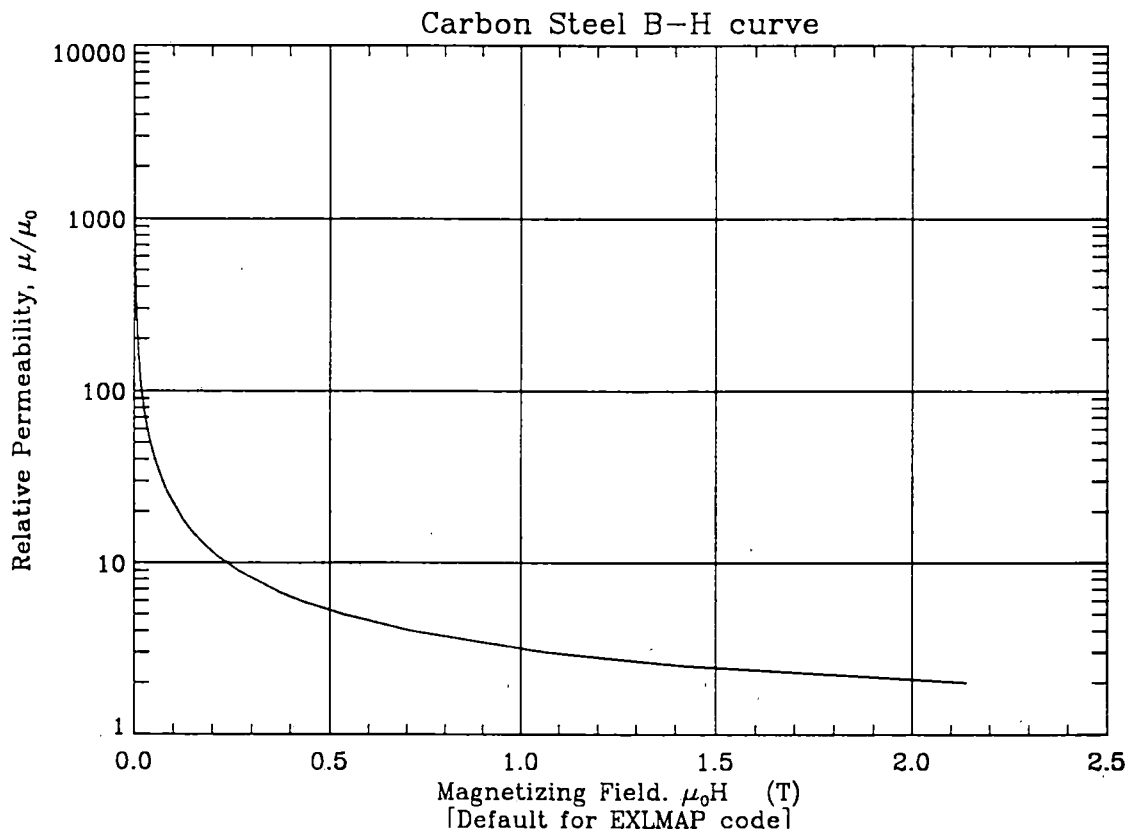


Figure 2. Relative permeability for carbon steel, from MAP *B-H* curve (see Figure 1)

Temperature Rise in Rebar Due to Eddy Current Dissipation

29 July 1994

J. R. Hale, J. Feng, R. D. Pillsbury, Jr.

This document and all reports and memoranda in this series are intended as a record of work in progress. They are for use in informal discussions of design, fabrication and further computation alternatives. This material is subject to change and should not, therefore, be published or referred to in the open literature. Conclusions are preliminary and distribution should be strictly limited.

Massachusetts Institute of Technology
Plasma Fusion Center
Cambridge MA 02139

MEMORANDUM

Date: 29 July 1994
To: R. D. Thornton
From: J. R. Hale, J. Feng, R. D. Pillsbury, Jr.
Subject: Memo PFC-RM-004, Rebar Project

Temperature Rise in Rebar Due to Eddy Current Dissipation

Having completed our comparison benchmark runs with our two finite element codes[1,2], we chose a rebar geometry typical of what would be utilized in concrete structures for Maglev guideways, a range of peak applied fields that we believe to be representative of the fields experienced by rebars in such structures, and a range of frequencies typical of the fundamental waveform generated by the coils in a passing maglev vehicle. Table 1 lists these physical parameters for use in our calculation of temperature rise:

Material	mild (carbon) steel
Diameter of cylindrical rebar (m [in])	0.0159 [0.625]
Mass per unit length (kg/m)	1.56
Specific heat (j/kg-K)	450
Electrical resistivity (Ω -m)	1.0×10^{-7}
Relative magnetic permeability:	carbon steel <i>B-H</i> curve
Applied field	sinusoidal

Table 1. Material Properties and Dimensions for Temperature Rise Calculations

The code MAP[3] was employed to generate data for twelve cases, with peak applied flux densities ranging from 0.05 T to 1.5 T, and frequencies ranging from 15.5 Hz to 64 Hz. Table 2 summarizes these results. Calculation of temperature rise per cycle presumes adiabatic conditions during the deposition of the energy: units are milli-kelvins per cycle. Figures 1 and 2 show loss per unit length plotted vs peak applied field, and against frequency, respectively.

$\mu_0 H_0$ (T)	f (Hz)	$\Delta E, \perp$ field (j/m per cycle)	$\Delta E, \parallel$ field (j/m per cycle)	$\Delta T, \perp$ field (mK per cycle)	$\Delta T, \parallel$ field (mK per cycle)
0.05	15.5	0.0132	33.5	0.0188	47.8
0.05	32	0.0182	32.0	0.026	45.7
0.05	64	0.0272	25.2	0.0388	35.9
0.10	15.5	0.0784	53.5	0.112	76.3
0.10	32	0.132	67.7	0.188	96.6
0.10	64	0.232	66.1	0.331	94.3
0.20	15.5	0.544	88.6	0.776	126
0.20	32	1.01	120.1	1.44	171
0.20	64	1.8	151.2	2.57	216
0.50	15.5	7.52	152.7	10.7	218
0.50	32	13.6	212.6	19.4	303
0.50	64	23.6	313.4	33.7	447
1.00	15.5	44.0	217.3	62.8	310
1.00	32	84.8	322.0	121	459
1.00	64	152.0	503.9	217	719
1.50	15.5	86.8	307.1	124	438
1.50	32	168.0	433.0	240	618
1.50	64	316.0	637.8	451	910

Table 2. Eddy current dissipation per unit length per cycle, and adiabatic temperature rise per cycle in carbon steel rebar.

For steel rebars with diameters only slightly different from this example case, which we understand would be typical for maglev guideway structures, loss per unit length should scale approximately as the square of the diameter. This being the case, the temperature rise results should not be diameter dependent, for both the loss per unit length and the mass per unit length scale with the square of the diameter. Figure 3 plots temperature rise vs peak applied field for both perpendicular and axial applied field components.

References

1. J. R. Hale, J. Feng, and R. D. Pillsbury, Jr., PFC-RM-002 (inter-project memorandum) July, 1994.
2. J. R. Hale, J. Feng, and R. D. Pillsbury, Jr., PFC-RM-003 (inter-project memorandum) July, 1994.
3. R. D. Pillsbury, Jr., "MAP User's Manual", PFC/RR-91-5, Plasma Fusion Center, MIT, December, 1991.

Eddy Current Dissipation in Rebar

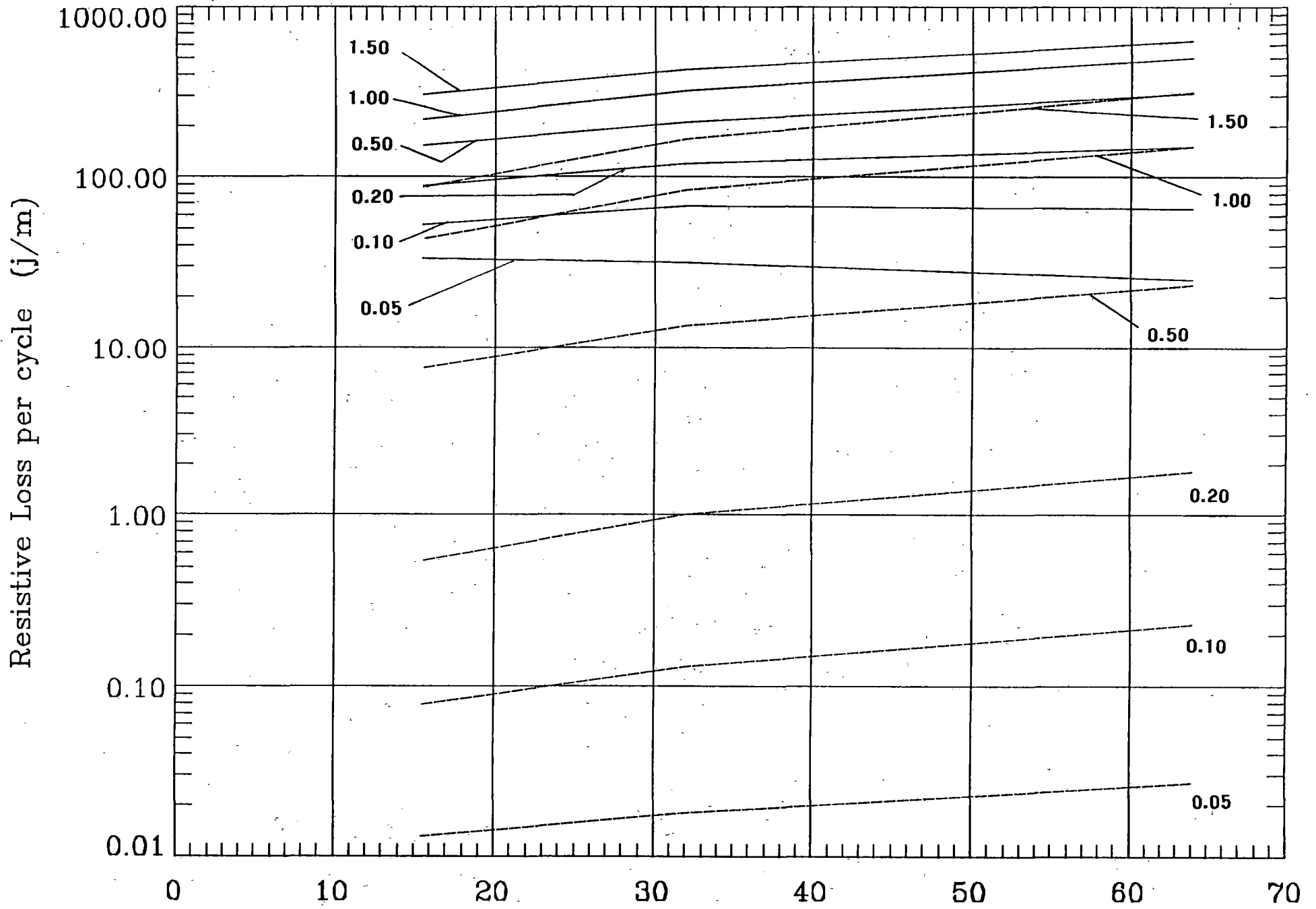


Figure 1

frequency (Hz)
(5/8" diameter steel)

Eddy Current Dissipation in Rebar

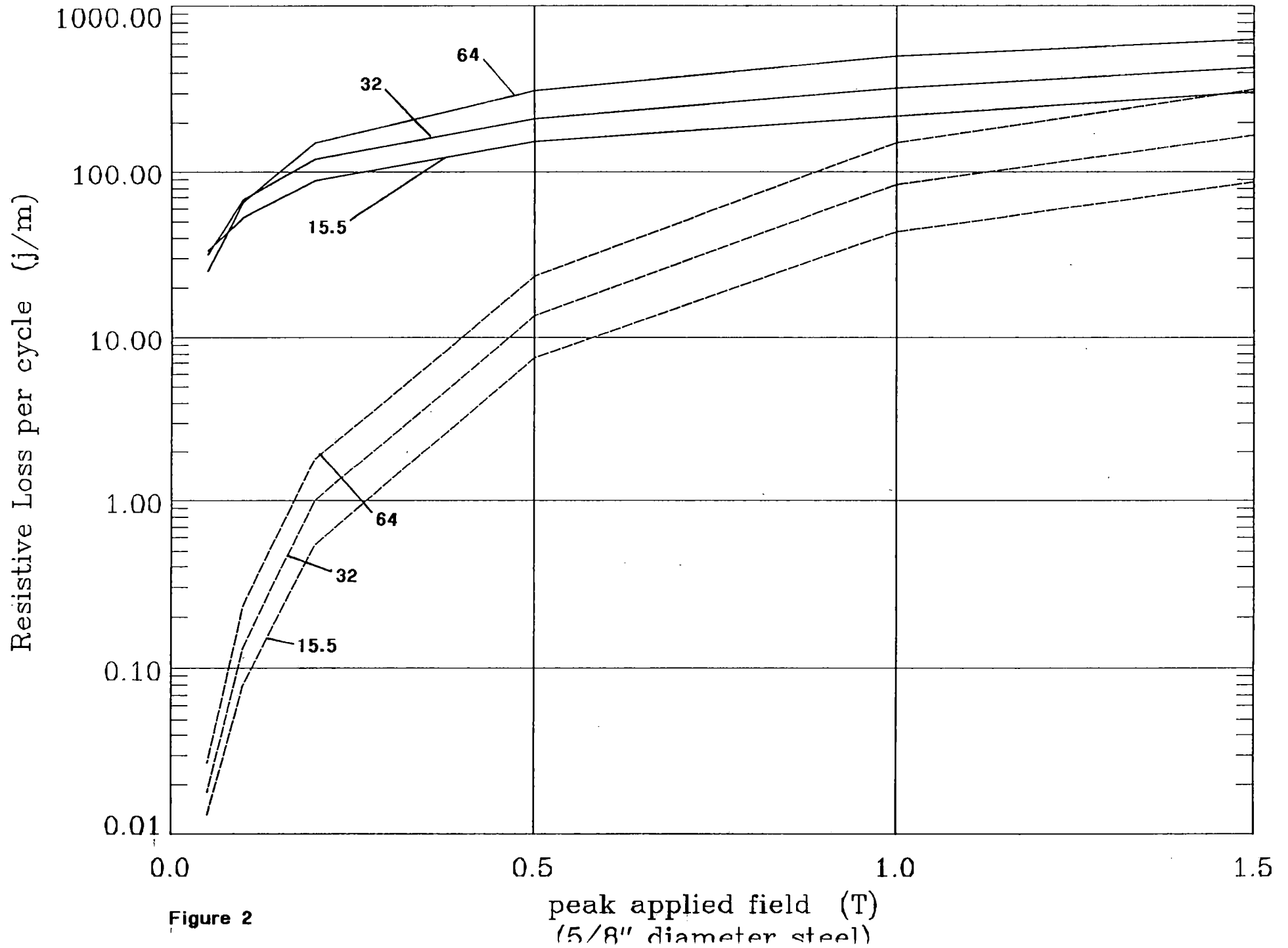


Figure 2

Temperature Rise per Cycle (mK)

1000.00

100.00

10.00

1.00

0.10

0.01

Eddy Current Dissipation in Rebar

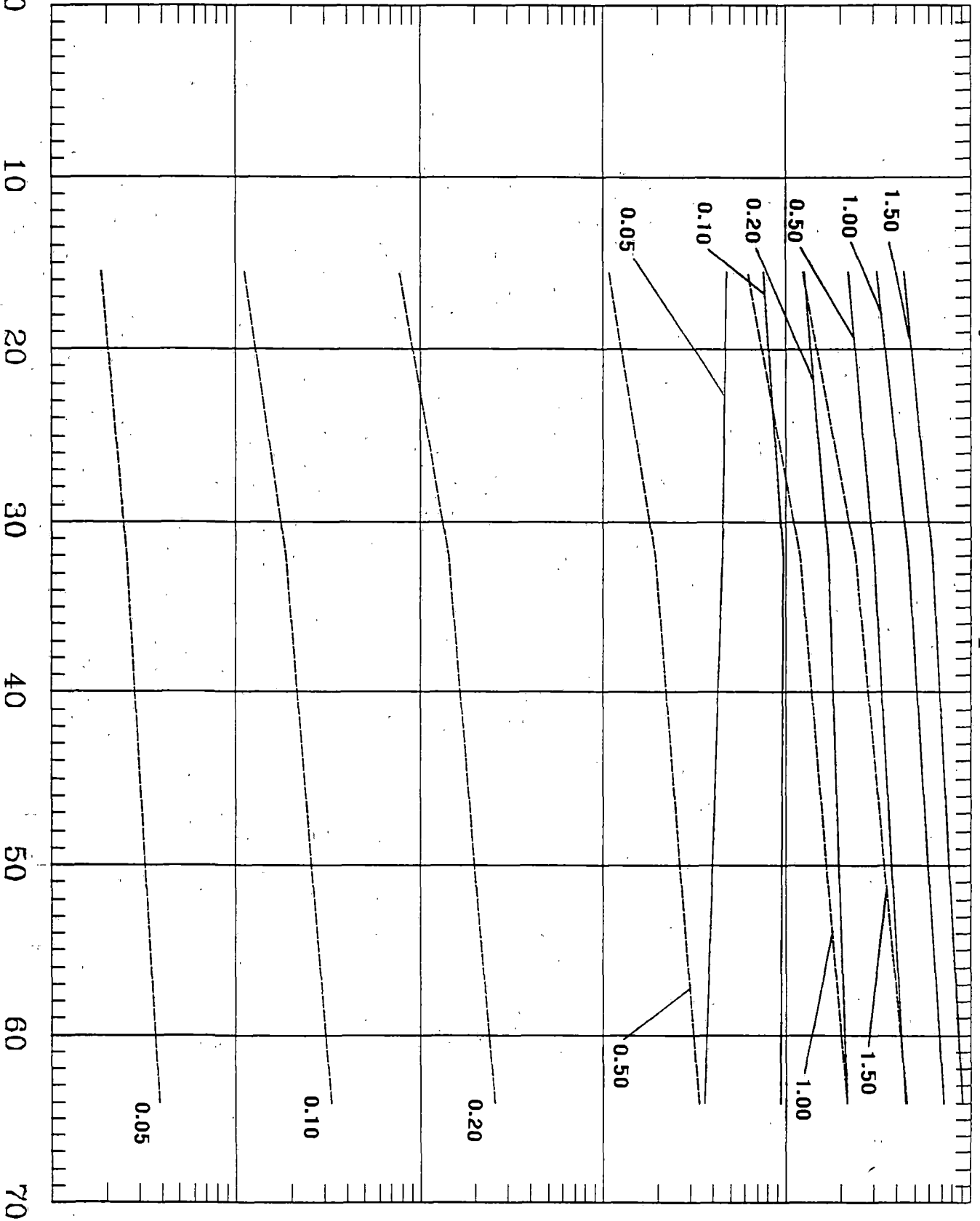


Figure 3

frequency (Hz)
15/R11 diameter steel

Rebar Hysteresis Loss

12 July 1994

J. Feng , J. R. Hale, and R. D. Pillsbury, Jr

This document and all reports and memoranda in this series are intended as a record of work in progress. They are for use in informal discussions of design, fabrication and further computation alternatives. This material is subject to change and should not, therefore, be published or referred to in the open literature. Conclusions are preliminary and distribution should be strictly limited.

Massachusetts Institute of Technology
Plasma Fusion Center
Cambridge MA 02139

MEMORANDUM

Date: 12 July 1994
To: R. D. Thornton
From: J. Feng, J. R. Hale, and R. D. Pillsbury, Jr.
Subject: Rebar Project Memo RM-005, Rebar Hysteresis Loss

Introduction[1]

The Law of Steinmetz is much used to evaluate the hysteresis loss in various materials exposed to an applied maximum magnetic field, B_m , within the range $500 < B_m < 15,000$ gauss.

Law of Steinmetz: $W_h = \eta B_m^{1.6}$

where W_h is the hysteresis loss in units of ergs/cm³, η is an empirically determined material properties constant, listed in Table 1, and B_m is in units of gauss.

For the case of less intense applied field (e.g. less than 200 gauss), the law of Rayleigh applies:

Law of Rayleigh: $W_h = \left(\frac{1}{3\pi}\right) \nu H_m^3 = \left(\frac{1}{3\pi}\right) B_m^3 \frac{\nu}{\mu^3}$

where ν is defined by $\mu = \mu_0 + \nu H$. Factors that can affect the hysteresis loss include gross composition, heat treatment, impurities, temperature, fabrication method, and stress, among others.

Results

Table 1 lists characteristics of several materials for which hysteresis loss was calculated.

No.	Materials	Composition %	Treatment	$\eta \times 10^6$
1	iron	99.9 Fe	annealed, 1400 C	45
2	iron	99.9 Fe	annealed, 900 C	1200
3	iron	99.9 Fe	50% cold work	4,000
4	chrome steel	96 Fe, 3 Cr, 1 C	quenched, 825 C	60,000

Table 1. List of Materials Evaluated for Hysteresis Loss

The relationship between the hysteresis loss per cycle and the applied maximum magnetic field, B_m , based on the Steinmetz law, is shown in Figure 1 for a rebar of radius 0.3125", made of the materials listed in Table 1.

The hysteresis losses plotted in Figure 1 are lower than eddy current losses[2] over the entire range of applied field strength of interest, even for material No. 4 in the table, chrome steel (which is not even a rebar material).

References

1. R. M. Bozorth, *Ferromagnetism*, IEEE press, QC753.B793, 1993.
2. J. R. Hale, J. Feng, and R. D. Pillsbury, Jr., PFC-RM-004 (inter-project memorandum) July, 1994.

Hysteresis Loss in Rebar, $r = 8$ mm

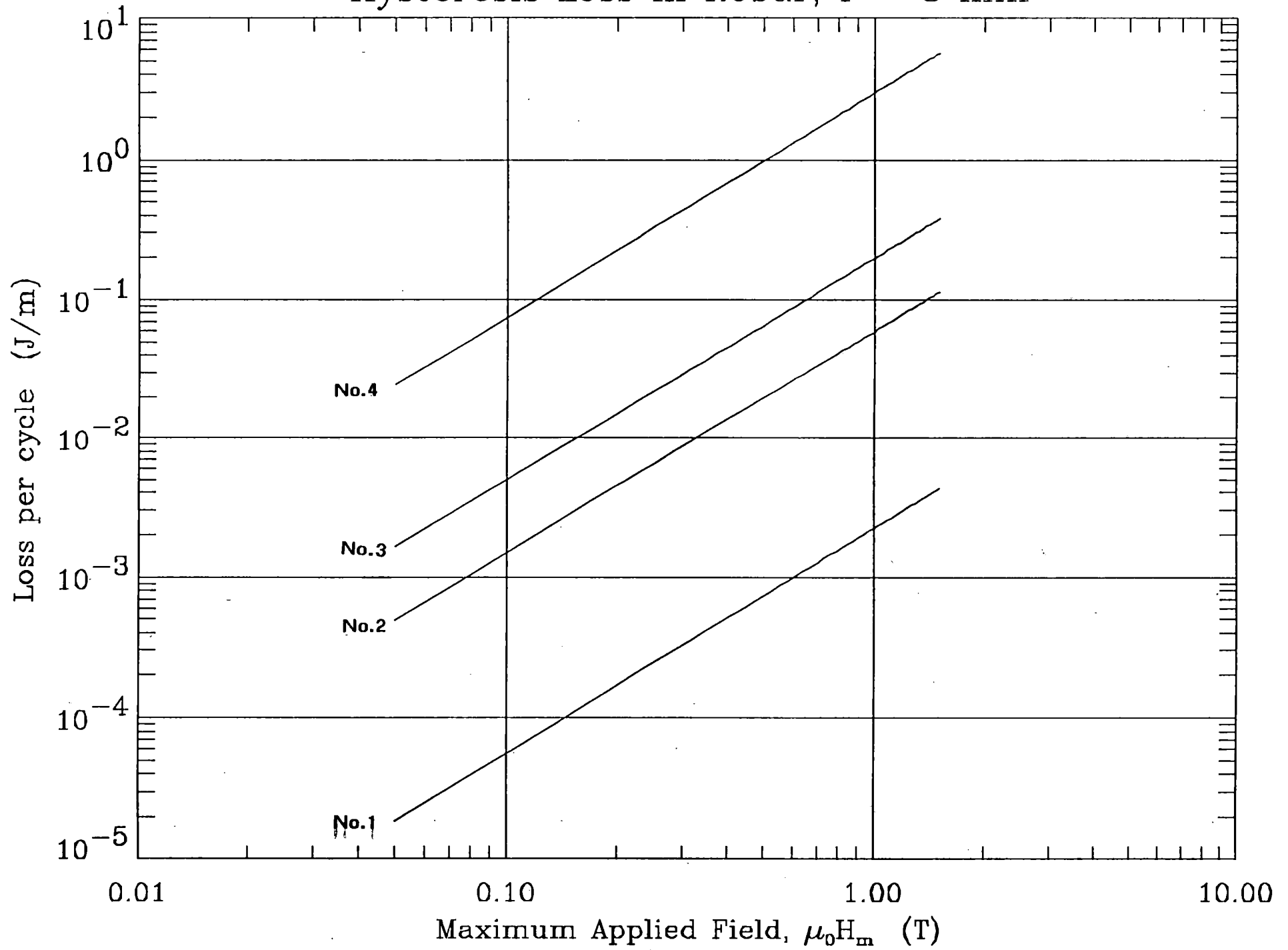


Figure 1

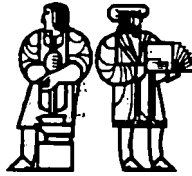
**Comments On The Need For Electrical
Insulation of Rebars**

J. R. Hale, J. Feng, and R. D. Pillsbury, Jr.

23 November 1994

This document and all reports and memoranda in this series are intended as a record of work in progress. They are for use in informal discussions of design, fabrication and further computation alternatives. This material is subject to change and should not, therefore, be published or referred to in the open literature. Conclusions are preliminary and distribution should be strictly limited.

Massachusetts Institute of Technology
Plasma Fusion Center
Cambridge MA 02139



Bldg/Rm NW22-227
Telephone 617/253-8161
Fax 617/253-0807
Internet hale@pfc.mit.edu

Plasma Fusion Center
Massachusetts Institute of Technology
Cambridge, Massachusetts 02139-4294

MEMORANDUM

Date: 23 November 1994
To: R. D. Thornton
From: J. R. Hale, J. Feng, and R. D. Pillsbury, Jr.
Subject: Memo PFC-RM-007, rebar project

Comments On The Need For Electrical Insulation of Rebars

Earlier memos have dealt with eddy currents induced in isolated rebars, and the concomitant heating and drag force. Although we have shown that for these calculations, rebars in a typical structural grid can be treated as magnetically isolated from one another, they are, after all, physically connected in order to form the grid and maintain its integrity until the concrete has cured. In order to complete our survey of potential effects of induced eddy currents, we broadened our scope to take into account the possibility that there could be electrical contact between rebars at the points where they are bound to one another. In such a grid of electrically communicating members, there will be induced loop currents, passing from rebar to rebar as a maglev vehicle passes.

To carry out a full three-dimensional analysis of all possible rebar-rebar current loops in a realistic grid would be prohibitively time-consuming. Instead, we elected to make use of a model of the Bechtel system in order to learn something about the scale of the potential problem such loop currents might present. A simple stick model was devised, including a vehicle bogie, the guideway ladder, and a simple rebar grid with reasonably realistic dimensions and spacings.

The calculation was carried out for a vehicle velocity of 150 m/s, and a vertical off-set (per the Bechtel concept) of 1.6 cm. The rebars in the grid were assumed to be in perfect electrical contact where they were touching, with a resistance per unit length of $5 \times 10^{-4} \Omega/\text{m}$ (corresponding to 0.375" diameter carbon steel bars.)

The results of this "scoping" study revealed that in this worst case scenario, circulating loop currents of more than 1% of the vehicle magnet current would be induced in the rebars. For this test case, that would be about 4 kA. The waveform would be a burst of alternating current (a.c.), qualitatively much the same as that described in earlier memos for the internal rebar eddy currents. These current density components would be additive to the local eddy currents. Moreover, there would be a transient burst of a.c. $I \times B$ force as the vehicle magnetic field interacted with the transient burst of a.c. current in the rebar. This force would be additive to the ferromagnetic forces on the rebars.

On the basis of this one example, we suggest that the prudent approach would be to preclude the possibility of electrical connectivity among neighboring rebars by specifying that if metallic rebars are to be used, they must be coated with electrically insulating material, or that the contact points must incorporate some sort of isolation fitting.

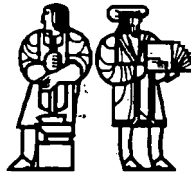
**Temperature Rise and Drag Force
Concomitant with Eddy Currents in Rebars:
Application of Project Results to Bechtel
and Foster-Miller Concept Systems**

J. R. Hale, J. Feng, and R. D. Pillsbury, Jr.

23 November 1994

This document and all reports and memoranda in this series are intended as a record of work in progress. They are for use in informal discussions of design, fabrication and further computation alternatives. This material is subject to change and should not, therefore, be published or referred to in the open literature. Conclusions are preliminary and distribution should be strictly limited.

Massachusetts Institute of Technology
Plasma Fusion Center
Cambridge MA 02139



Bldg/Rm NW22-227
Telephone 617/253-8161
Fax 617/253-0807
Internet hale@pfc.mit.edu

Plasma Fusion Center
Massachusetts Institute of Technology
Cambridge, Massachusetts 02139-4294

MEMORANDUM

Date: 23 November 1994
To: R. D. Thornton
From: J. R. Hale, J. Feng, and R. D. Pillsbury, Jr.
Subject: Memo PFC-RM-008, rebar project

Temperature Rise and Drag Force Concomitant with Eddy Currents in Rebars: Application of Project Results to Bechtel and Foster-Miller Concept Systems

One series of calculations carried out for this project was of the intensity of the magnetic field produced by maglev vehicle magnets at the locations of rebars in the guideway structure, modeling actual vehicle coil geometries for the two prescribed concept systems. The results showed, as might be expected for arrays of magnetic multipoles, complex spatial and time variant patterns of field within the guideway's reinforced concrete. The prospect of carrying out a rigorous study of eddy current induction, taking into account three time-varying components of field, and rebars arranged in a three-dimensional grid with non-uniform spacing and varying diameters, seemed to us to be beyond the scope of this project. Hence, we have chosen to apply our generic results to the calculation of worst case temperature rises and worst case drag forces to the two representative systems.

We have learned from the generic studies that eddy current heating induced by the field component parallel to a rebar's long axis is more severe than that induced by the perpendicular component. Thus, to form the worst case scenario, we refer to our system-specific field maps to find which of the three field components is largest, and then presume that the worst heating will occur in all rebars that are parallel to that component. Once the peak value is known, the temperature rise and loss rates can be read from the appropriate plots [1]. The concomitant worst case drag force can be calculated for each of the two systems by plugging their respective worst case loss rates into the drag force equation in [2]. Table 1 summarizes these results: symbols in column 1 refer to quantities defined in reference [2].

	Bechtel System	Foster-Miller System
Field component, i , with highest peak value ¹	y	z
B_i max [T]	0.45	1.15
N_b	1	2
N_m	24	4
$\mathcal{E} (B_i \text{max, } 150 \text{ m/s) [j/m/cycle]}$	280	572
ΔT [K/cycle]	0.40	0.82
ΔT [K/vehicle transit]	4.8	3.28
F_d/N_r [newtons/rebar]	3.36×10^3	2.28×10^3

¹ The X axis is along the direction of motion, Y is the vertical axis, and Z is horizontal and transverse to the guideway.

Table 1. Summary of Project Results Applied to Two Concept Systems

References

1. J. R. Hale, J. Feng, and R. D. Pillsbury, Jr., PFC-RM-004 (inter-project memorandum) July, 1994.
2. J. R. Hale and R. D. Pillsbury, Jr., PFC-RM-006 (inter-project memorandum) September, 1994.

**Static forces on Rebars
for the
Foster-Miller Magnet-Guideway Geometry**

R. D. Pillsbury, Jr.

7 December 1994

This document and all reports and memoranda in this series are intended as a record of work in progress. They are for use in informal discussions of design, fabrication and further computation alternatives. This material is subject to change and should not, therefore, be published or referred to in the open literature. Conclusions are preliminary and distribution should be strictly limited.

Massachusetts Institute of Technology
Plasma Fusion Center
Cambridge MA 02139

To: J. R. Hale
From: R. D. Pillsbury, Jr.
Subject: Static forces on Rebars for the Foster Miller Magnet-Guideway Geometry

REF: PFC-RM-010

The magnetostatic forces that would be experienced by magnetically permeable reinforcing bars that may be in the guideway proposed for the Foster-Miller Maglev system has been assessed. Rebars in a number of different locations were evaluated to ascertain the sensitivity of the forces to the location within the guideway. A parallel study was performed for the Bechtel guideway design¹.

The Foster-Miller onboard magnet system consists of 2 bogeys on each side of the vehicle with 4 coils in each bogey. The polarity of the coils changes in a from magnet to magnet. The coils on either side of the vehicle oppose each other, that is, they have the opposite sign of current.

A three dimensional, magnetostatic analysis was performed using the finite element program ANSYS². Therefore, the results presented in this memorandum correspond to the case of the vehicle at rest, *i.e.*, zero speed. It is assumed that there is no interaction with the levitation windings in the guideway. The fields from the LSM are also ignored. The analysis was performed on a single rebar at a time. There were fifteen separate runs of differing distances from the coils. There are six bar positions in the out vertical legs of the U-shaped guideway and nine positions along the bottom of the guideway.

Figure 1 shows four views of the model and the magnetic flux density vectors in a rebar in the vertical leg of the guideway that is centered on the coil and 40 cm away. Symmetries of the coils and rebar imply that these results are equally valid for bars in the negative y-direction.

In this analysis, the rebar is modeled from the center of one bogey a plane of symmetry 12.5 m away. The bogey is centered on $X = 0$. There are four elements in the cross-section of the rebar.

In the Stress Tensor approach, the surface tractions are calculated. Figure 2 shows the traction vectors acting on the surfaces of the rebar. The net force in a cross-section is the sum of all the tractions on elements in that cross-section. As can be seen, the forces are toward the magnets as would be expected. The variation along the bar is also evident.

The Figures 1 and 2 were for a case of the rebar 40 cm from the center of the magnets (in the -Z direction). The 40 cm. was chosen as the closest possible location for rebars due to the room required for the levitation windings in the guideway, *etc.* Additional analyses were performed for the rebar 50 and 60 cm. from the coils.

The components of the surface tractions were summed at each cross-section along the rebar (X direction). These force components per unit length are displayed in Figures 3 and 4 and show the X-, and Z-directed components for force per unit length as a

¹ PFC-RM-009, "Static forces on rebars for the Bechtel Magnet-Guideway geometry,"

² ANSYS 5.0A, Swanson Analysis Systems, Inc., Houston, PA.

function of distance along the rebar for the cases of the rebar at 40, 50 and 60 cm from the coils. The Y -directed force is zero since the rebar is centered on the coil. The fall-off of the force with distance is quite evident. Figures 5 and 6 replot the data with an X axis extent of 3 m. The truncation of some of the peaks is a result of the discreteness of the finite element mesh. It can be seen that peak localized forces can be on the order of 900 N/m which was approximately the same order of magnitude as in the Bechtel analysis. One major difference is the large X -directed component of load which has a peak local value of 220 N/m.

The components of the force per unit length acting on a rebar 0.5 m above the center of the coils as a function of position along the rebar for the three different Z direction distances from the coils is shown in Figures 7-9. The fall-off of the force with distance is evident, especially in the Z -directed component.

An additional nine locations were evaluated. These corresponded to the "floor" of the U-shaped channel. Positions in the Z direction of -1.0, -0.5, and 0.0 m were evaluated for Y distances of 60, 70 and 80 cm, respectively. Figures 10-12 show the three force components per unit length for the -1.0 m case. Figures 13-15 and 16-18 show the results for the -0.5 m and 0.0 m case, respectively. The later case corresponds to a rebar directly under the coils centers.

The individual components of the force per unit length can be integrated (summed) to get the net force of the rebar (over a half-span length which, because of the fall-off, is roughly equivalent to a half-bogey. Table I presents these sums.

Table I - Net Forces on a Rebar over a Length of One Half Span

Y Distance (m)	Z Distance (cm)	F_x (N)	F_y (N)	F_z (N)
0	40	18	0	-697
	50	10	0	-472
	60	6	0	-326
50	40	4	-201	-82
	50	3	-131	-89
	60	3	-87	-83
-60	-100	0	11	12
-70		1	36	30
-80		0	15	4
-60	-50	1	66	9
-70		3	152	19
-80		0	31	-9
-60	0	1	52	64
-70		0	9	-48
-80		1	33	13

PFC-RM-010: List of Figures

Figure 1. Magnetic Flux Density Vectors in the Rebar of the Foster-Miller Guideway.

Figure 2. Maxwell Stress Traction Vectors Acting on the Rebar of the Foster-Miller Guideway.

Figure 3. F_x versus x for the rebars 40 cm from the bogey.

Figure 4. F_z versus x for the rebars 40 cm from the bogey.

Figure 5. F_x versus x ($0 < x < 3$ m) for the rebars 40 cm from the bogey.

Figure 6. F_z versus x ($0 < x < 3$ m) for the rebars 40 cm from the bogey.

Figure 7. F_x versus x for the upper outboard rebar at various distances from the bogey.

Figure 8. F_y versus x for the upper outboard rebar at various distances from the bogey.

Figure 9. F_z versus x for the upper outboard rebar at various distances from the bogey.

Figure 10. F_x versus x for the inside rebar at various distances from the bogey.

Figure 11. F_y versus x for the inside rebar at various distances from the bogey.

Figure 12. F_z versus x for the inside rebar at various distances from the bogey.

Figure 13. F_x versus x for the middle rebar at various distances from the bogey.

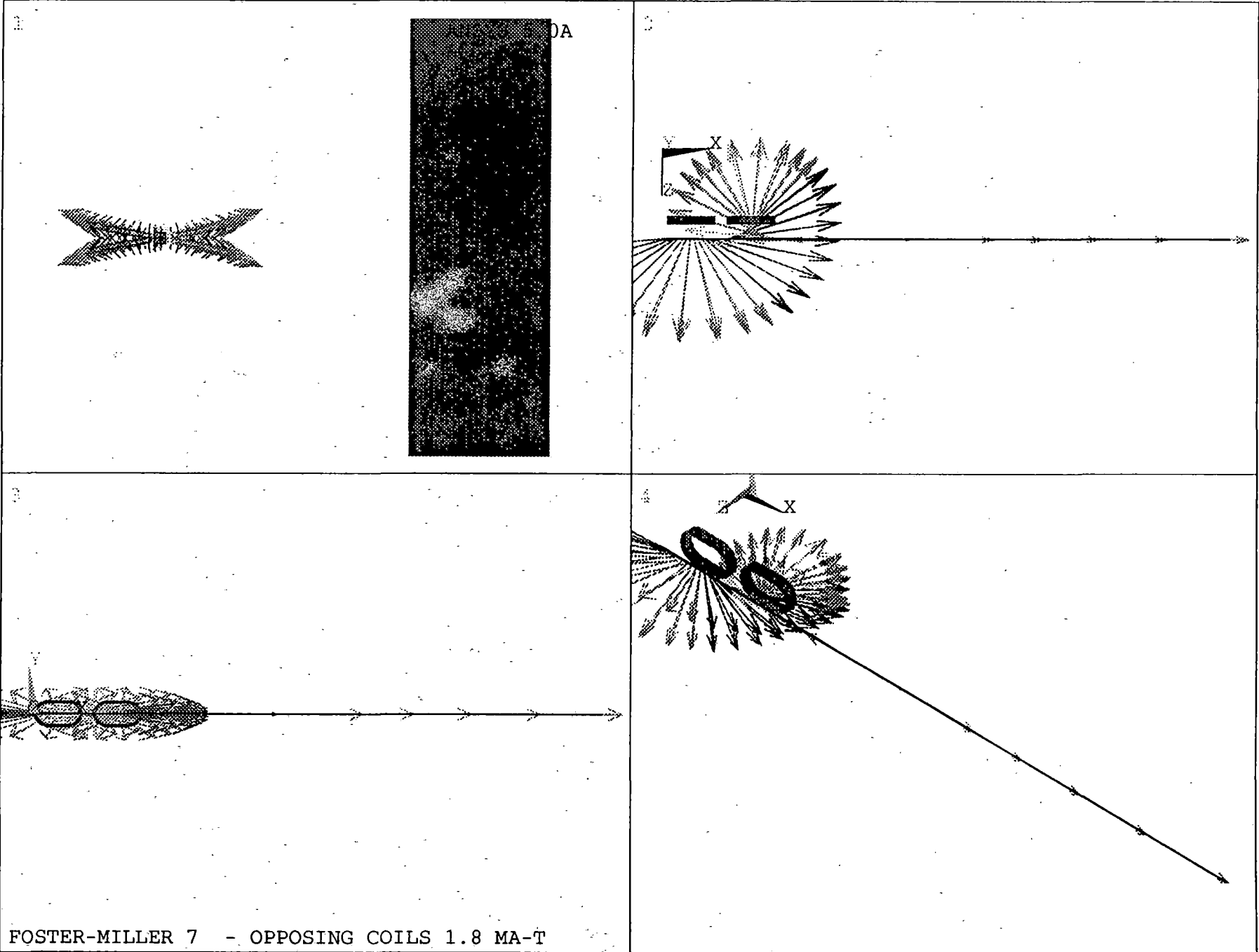
Figure 14. F_y versus x for the middle rebar at various distances from the bogey.

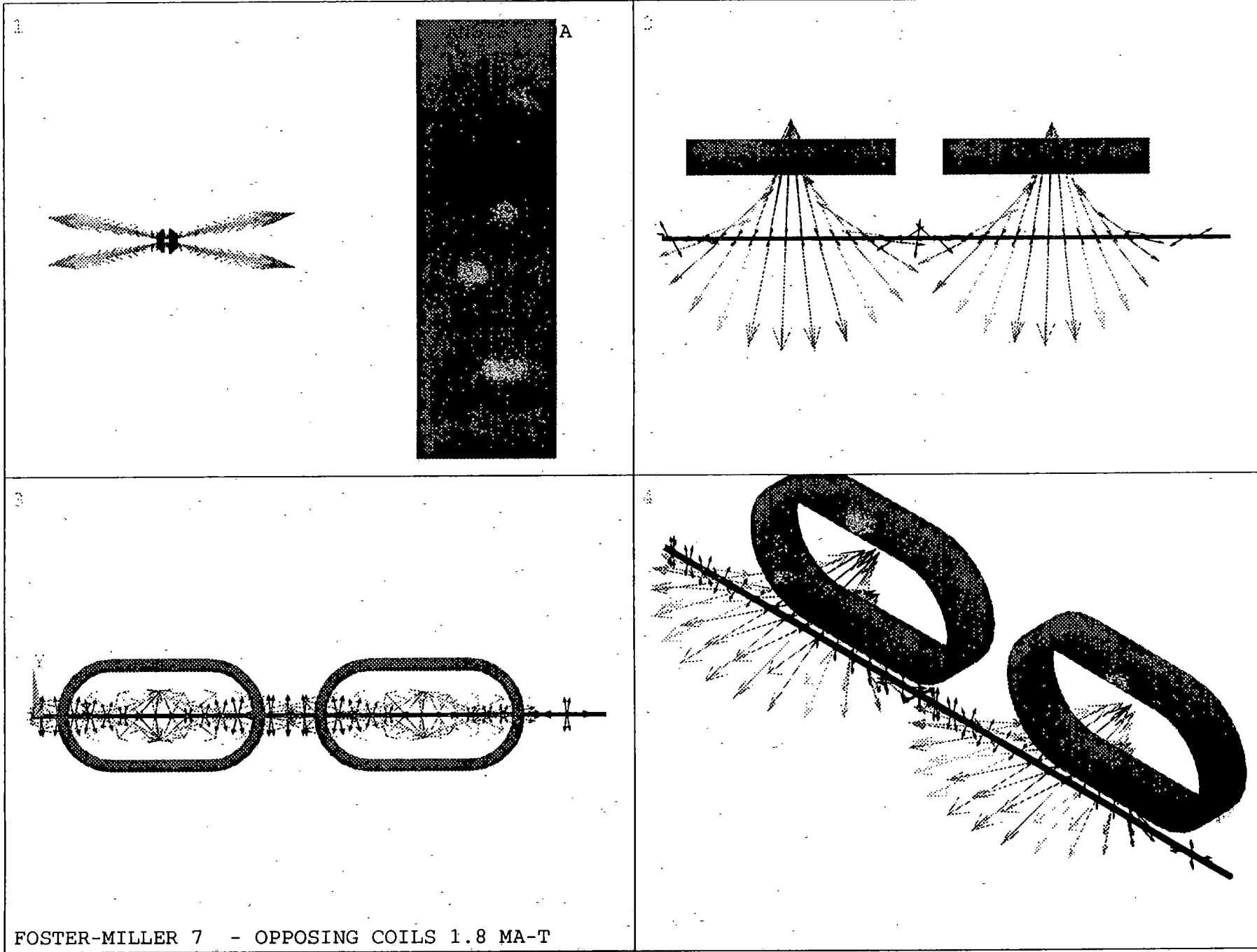
Figure 15. F_z versus x for the middle rebar at various distances from the bogey.

Figure 16. F_z versus x for the under rebar at various distances from the bogey.

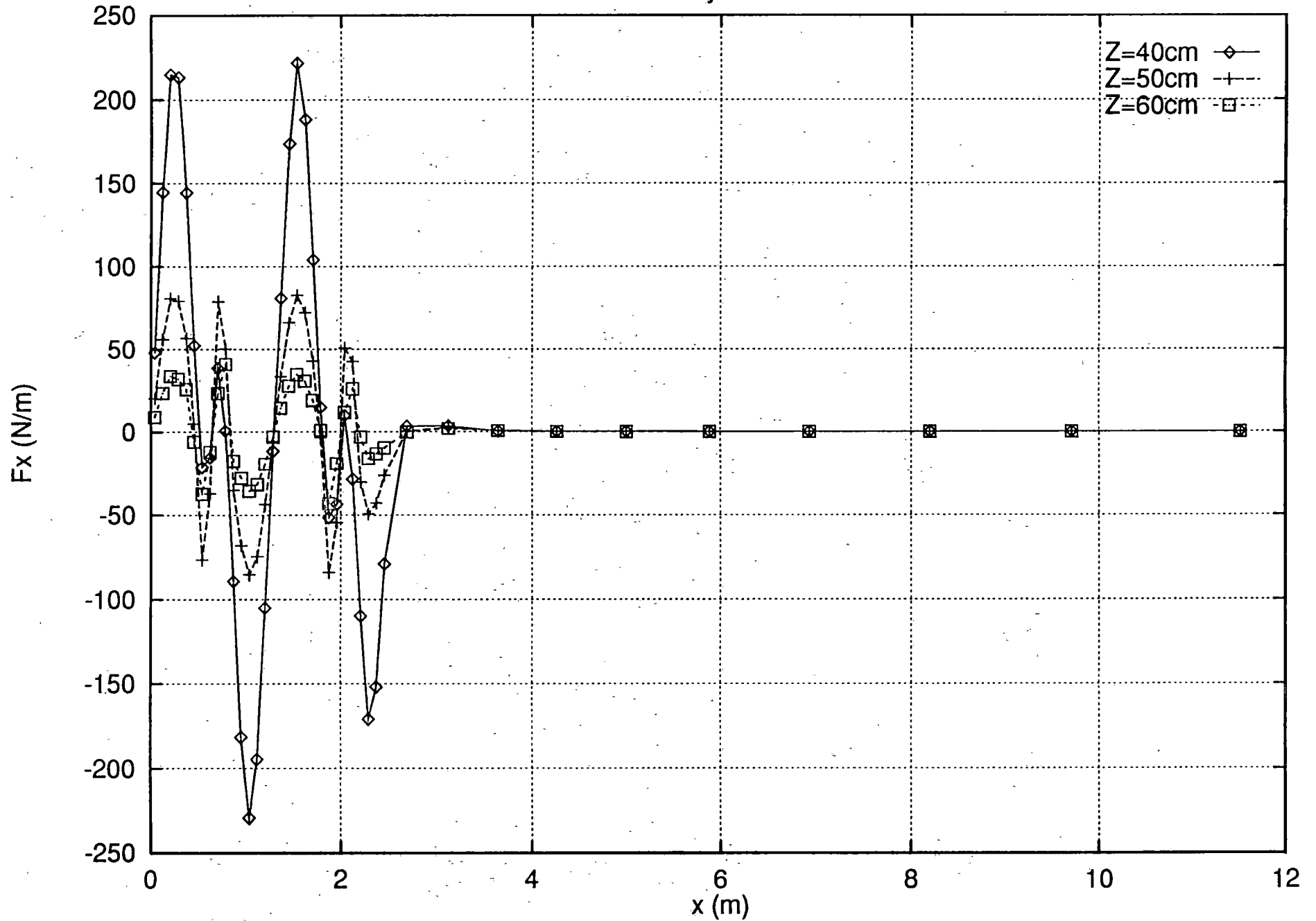
Figure 17. F_x versus x for the under rebar at various distances from the bogey.

Figure 18. F_z versus x for the under rebar at various distances from the bogey.

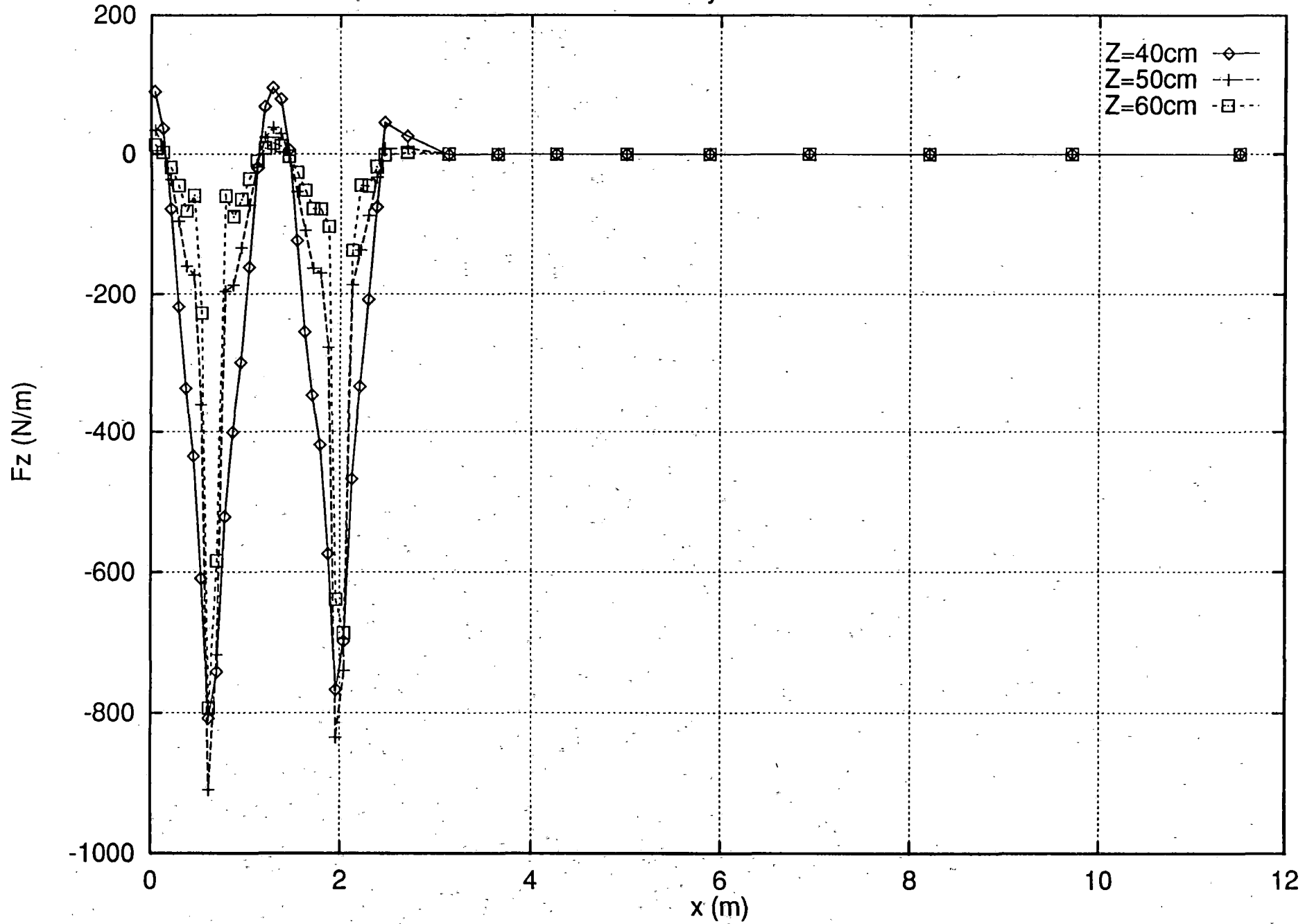




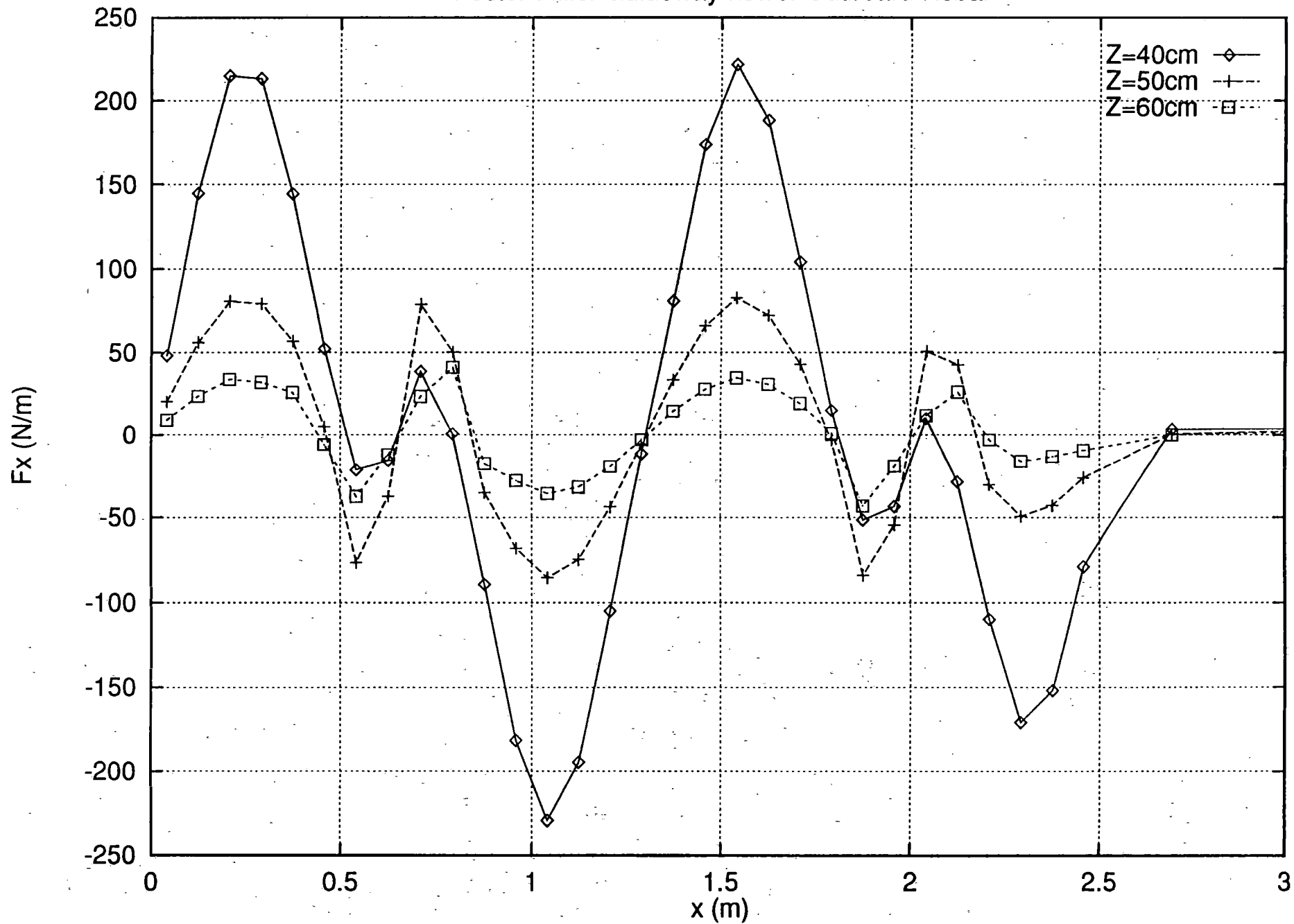
Foster-Miller Guideway Lower Outboard Rebar



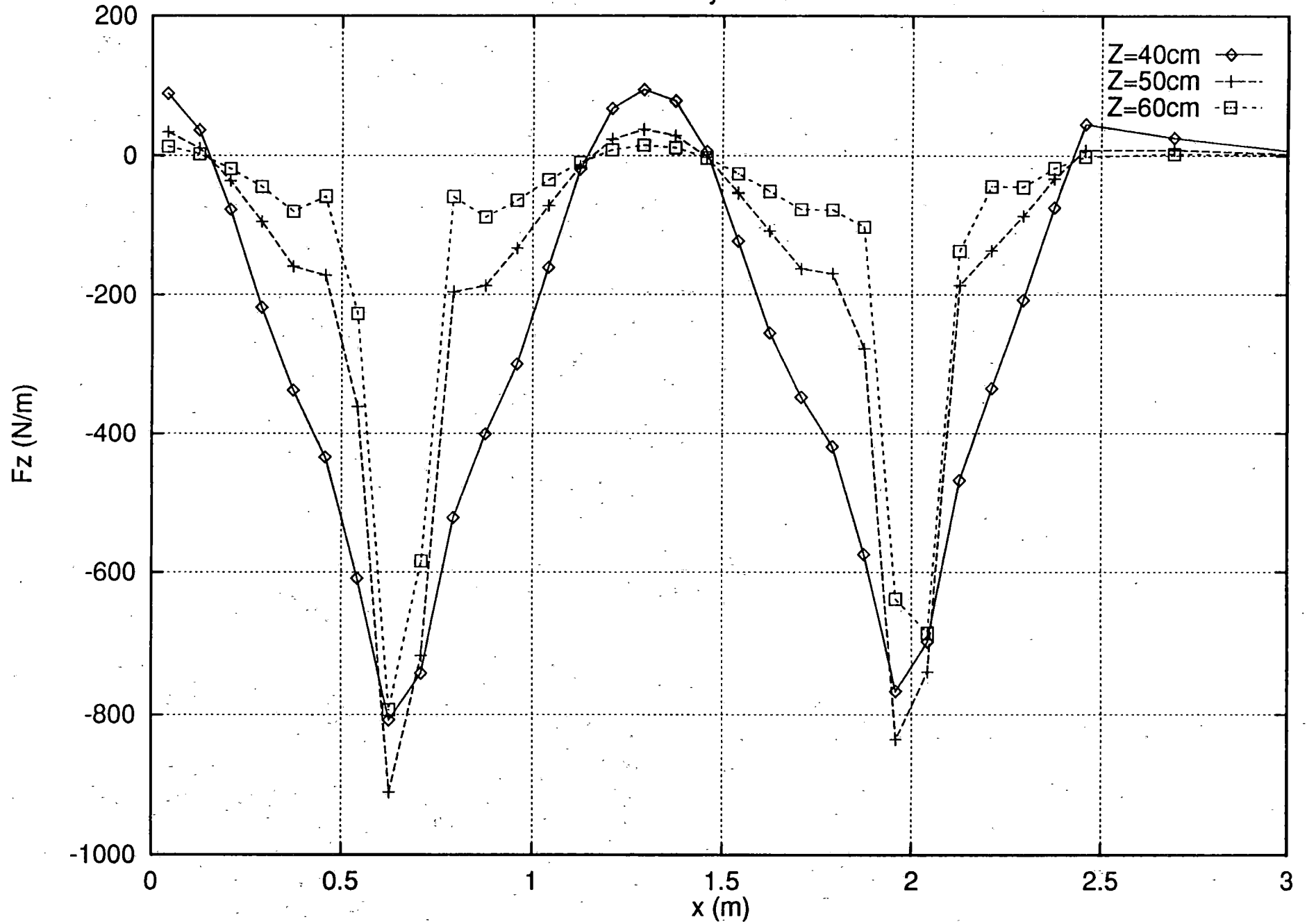
Foster-Miller Guideway Lower Outboard Rebar



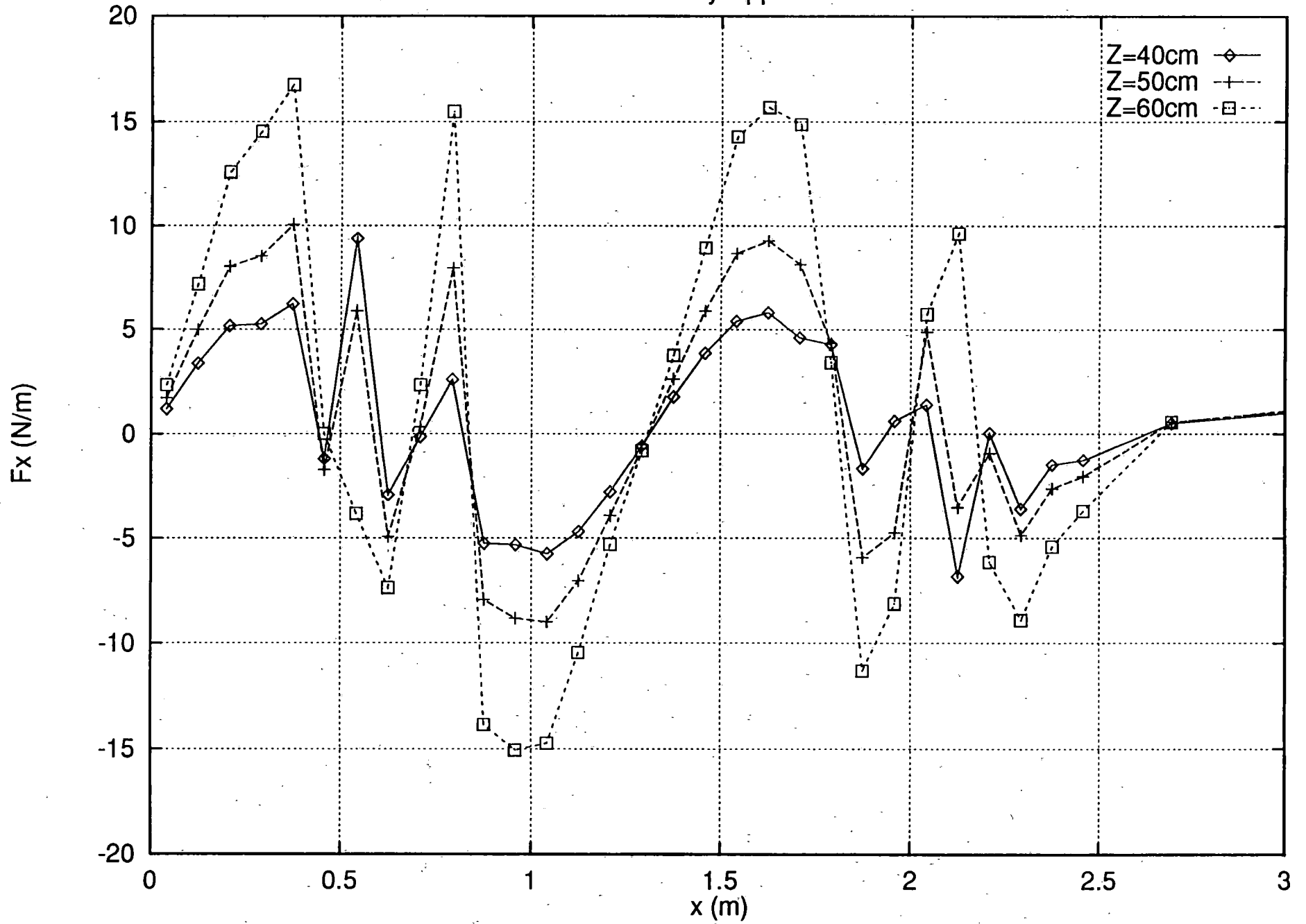
Foster-Miller Guideway Lower Outboard Rebar



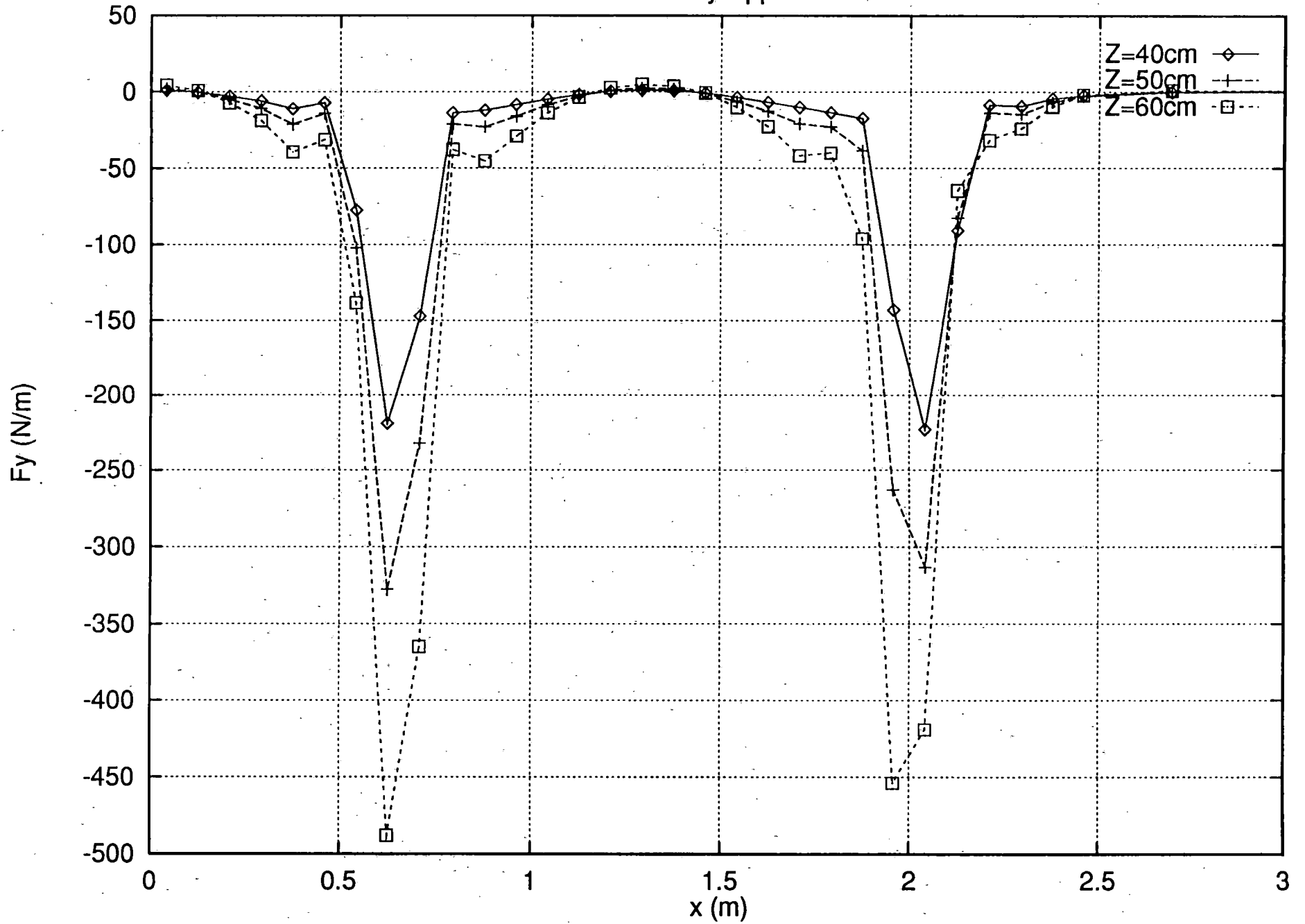
Foster-Miller Guideway Lower Outboard Rebar



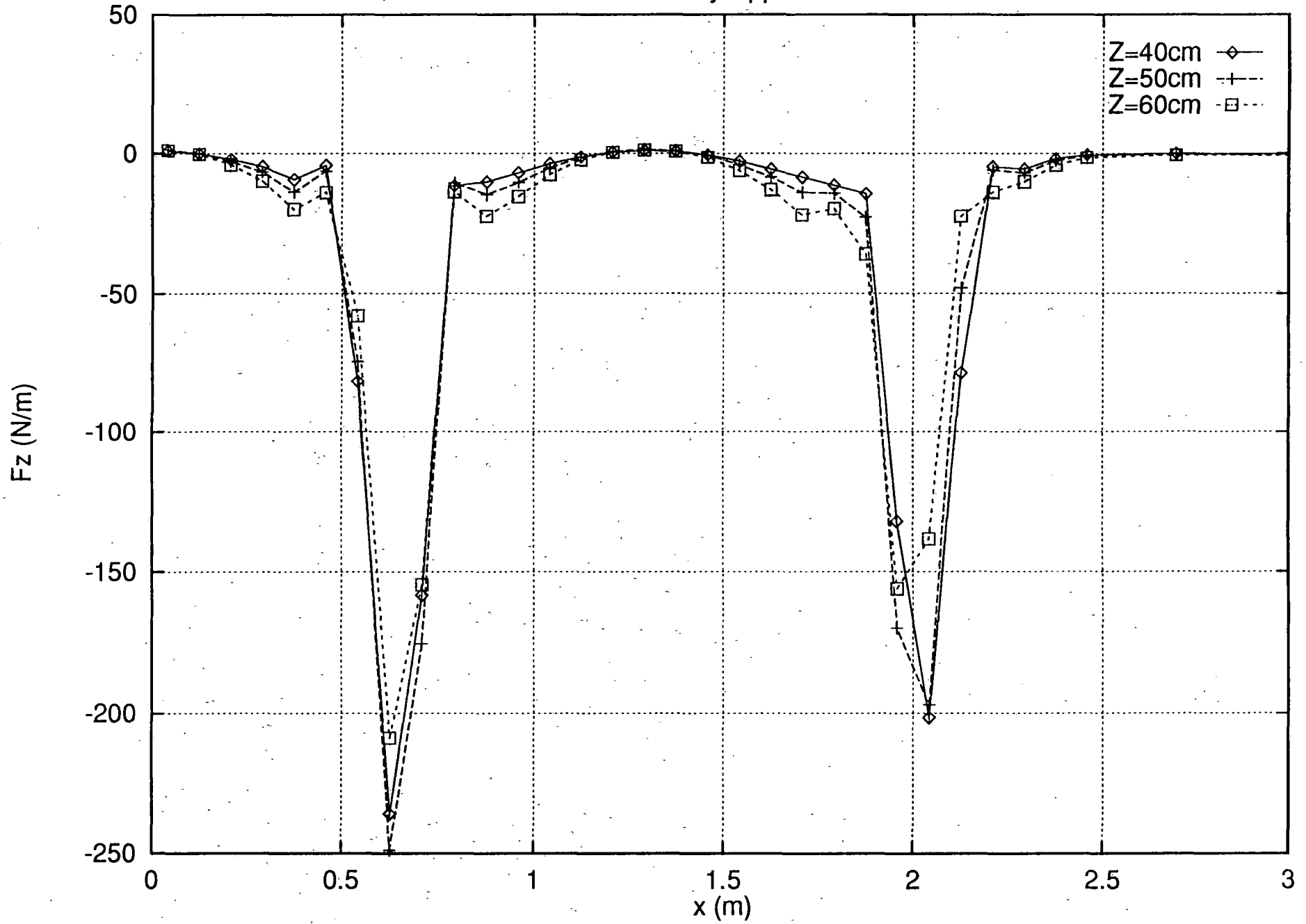
Foster-Miller Guideway Upper Outboard Rebar



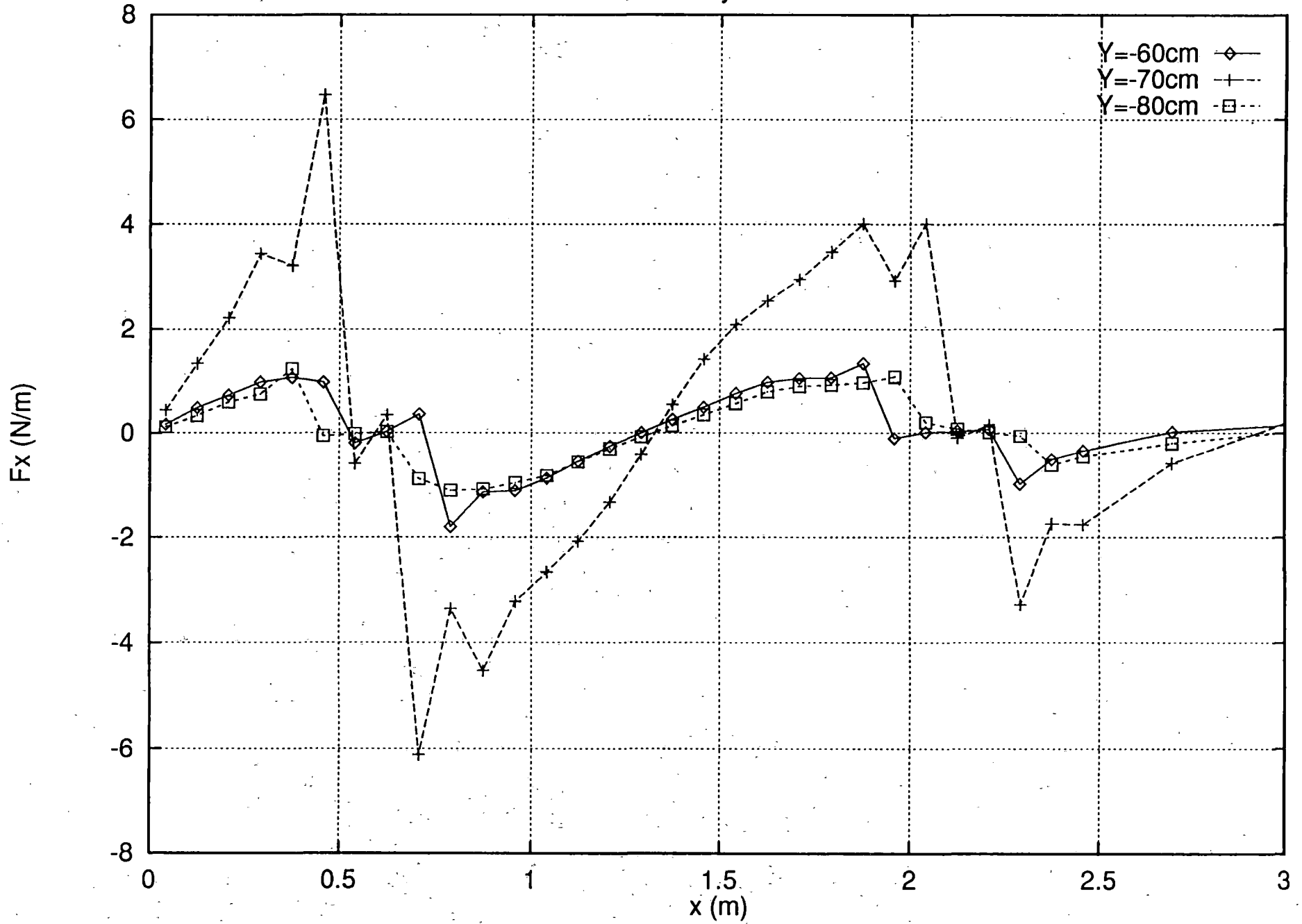
Foster-Miller Guideway Upper Outboard Rebar



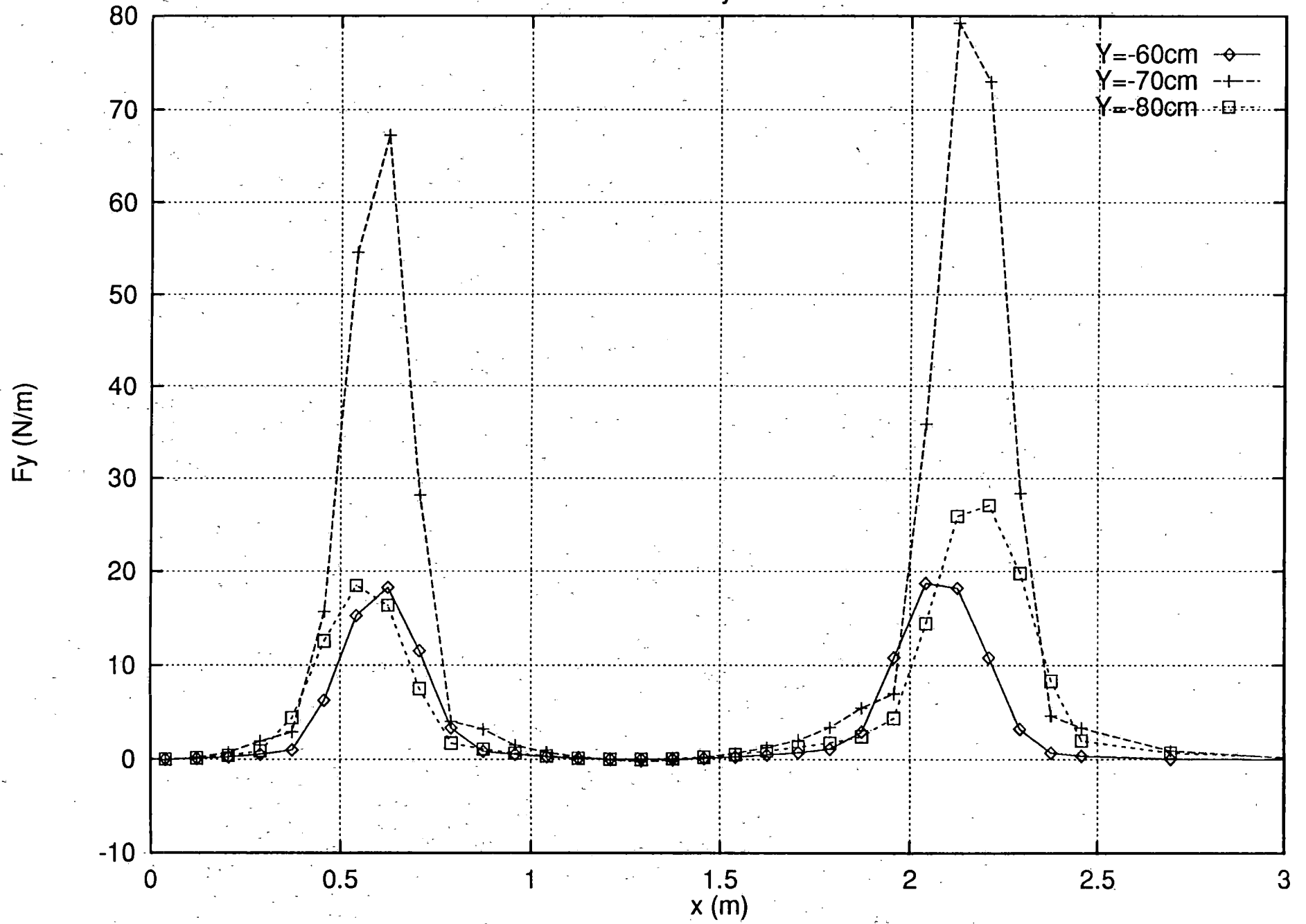
Foster-Miller Guideway Upper Outboard Rebar



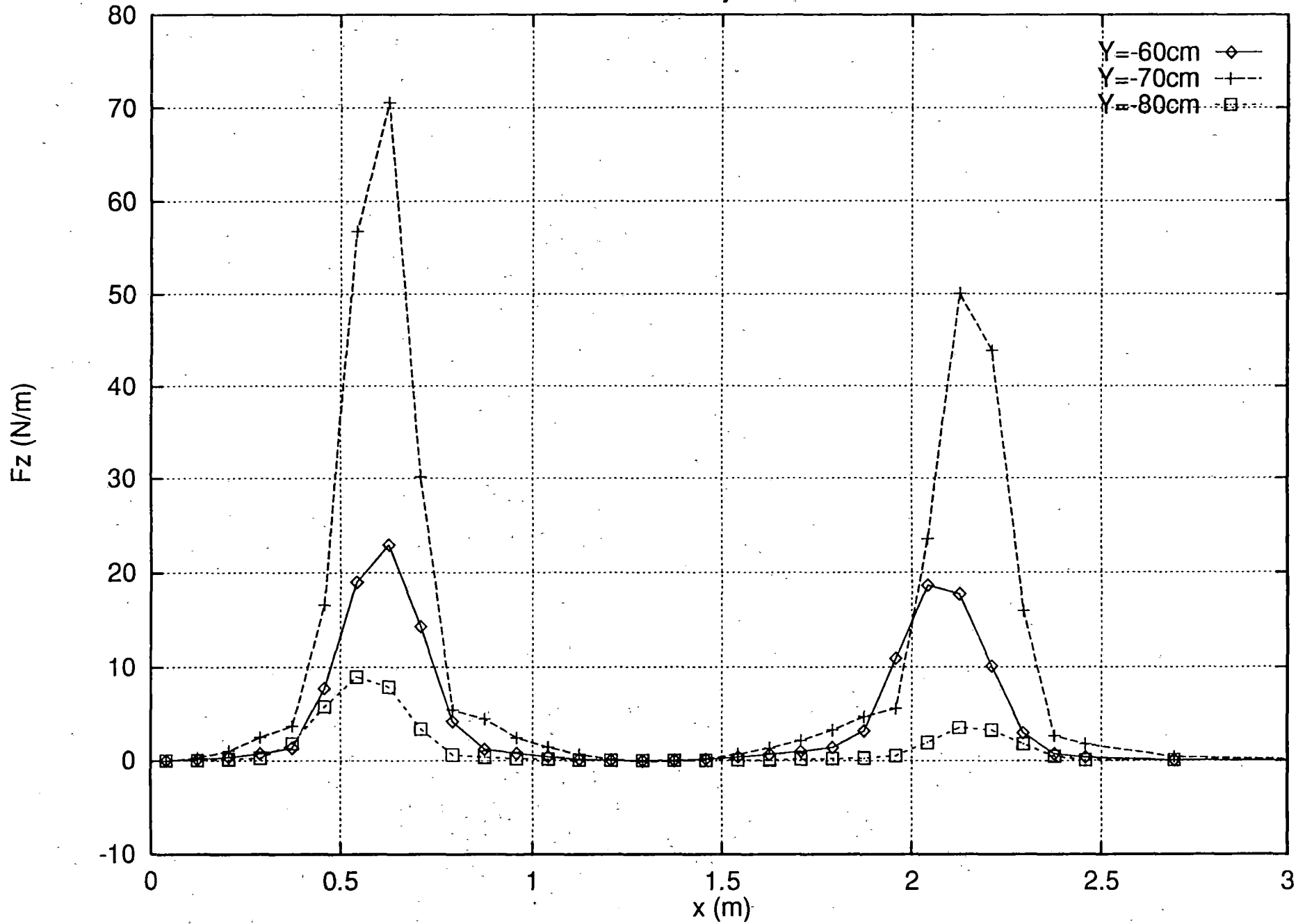
Foster-Miller Guideway Inside Rebars Z = -1



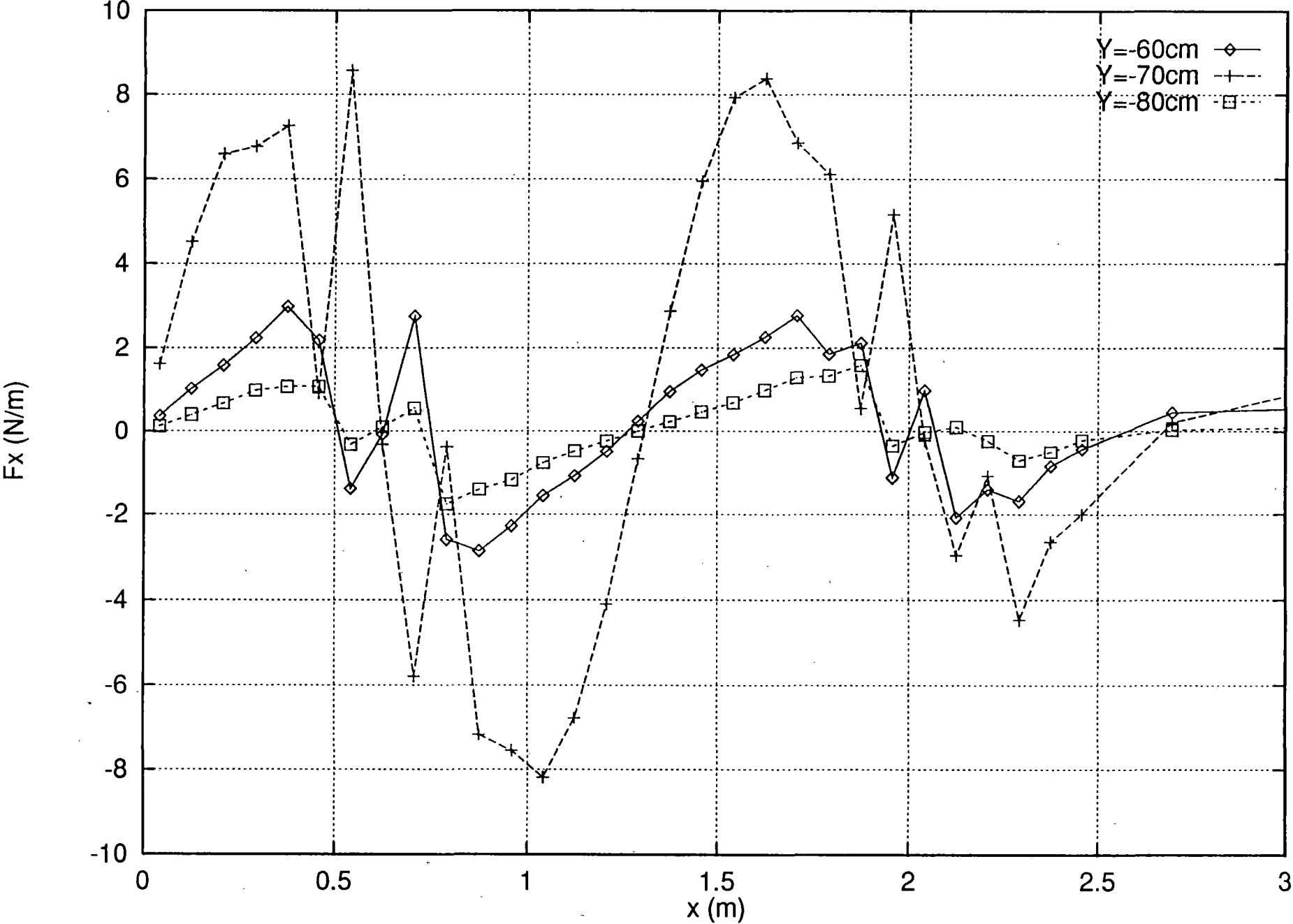
Foster-Miller Guideway Inside Rebars Z = -1



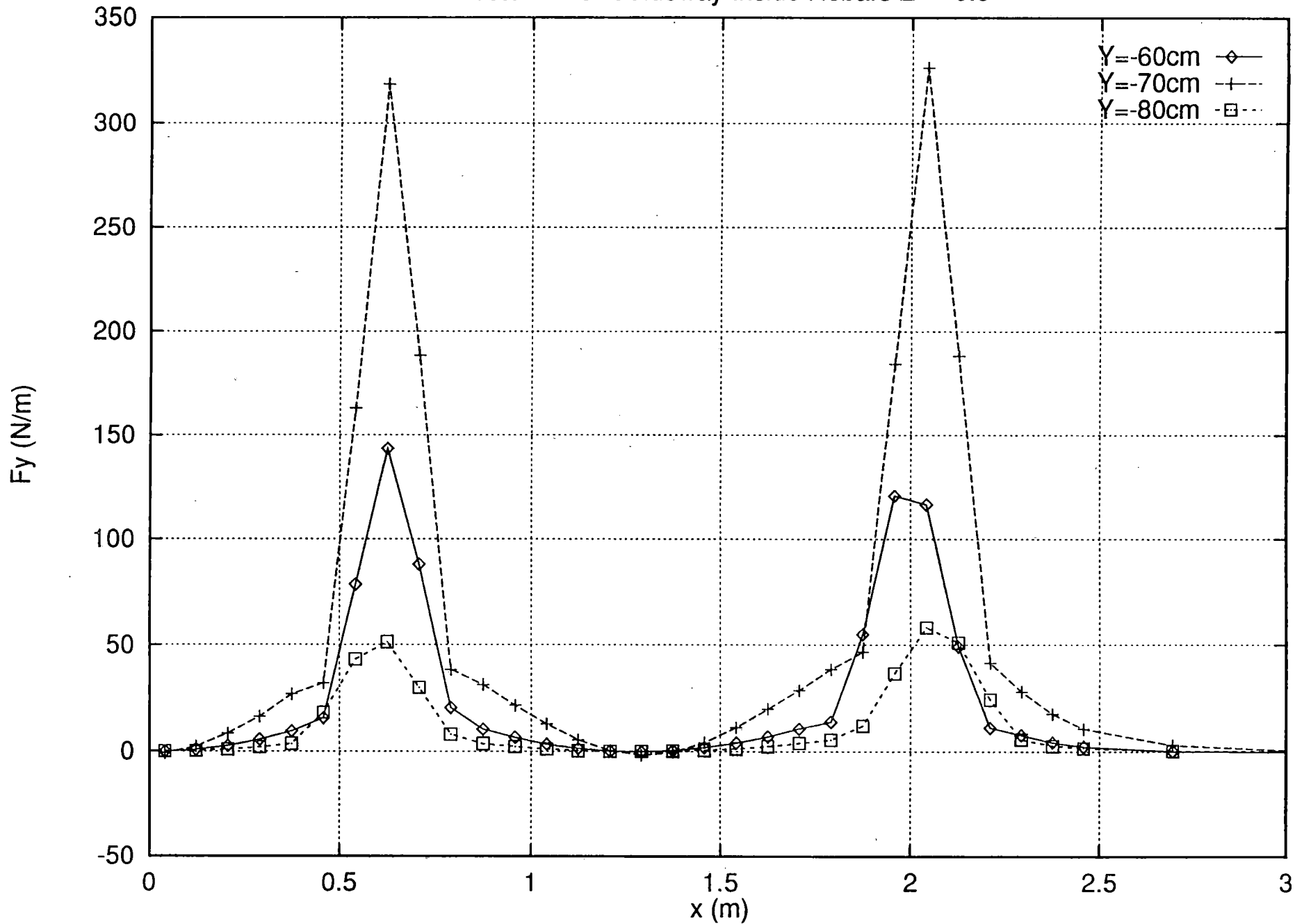
Foster-Miller Guideway Inside Rebars Z = -1



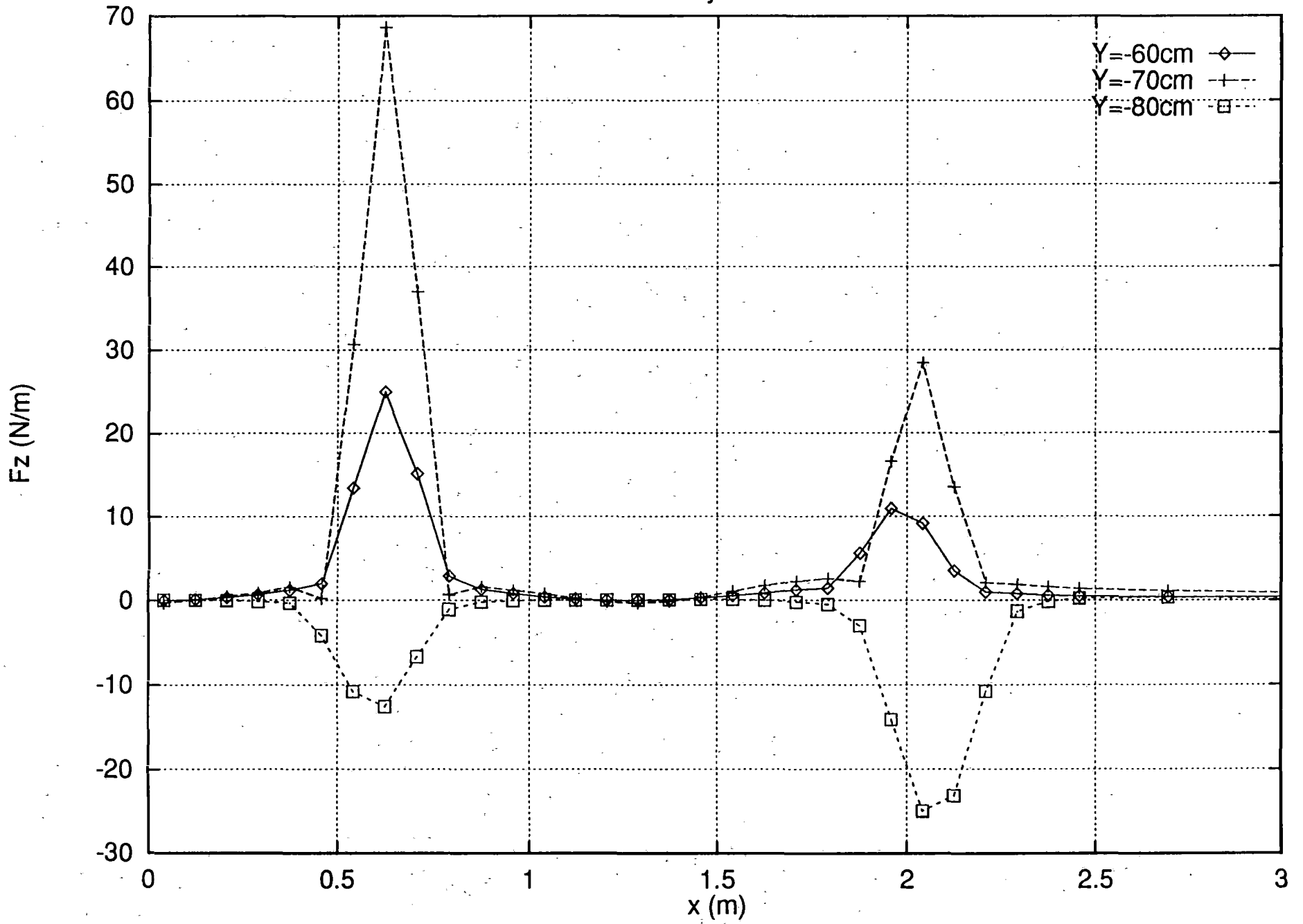
Foster-Miller Guideway Inside Rebars Z = -0.5



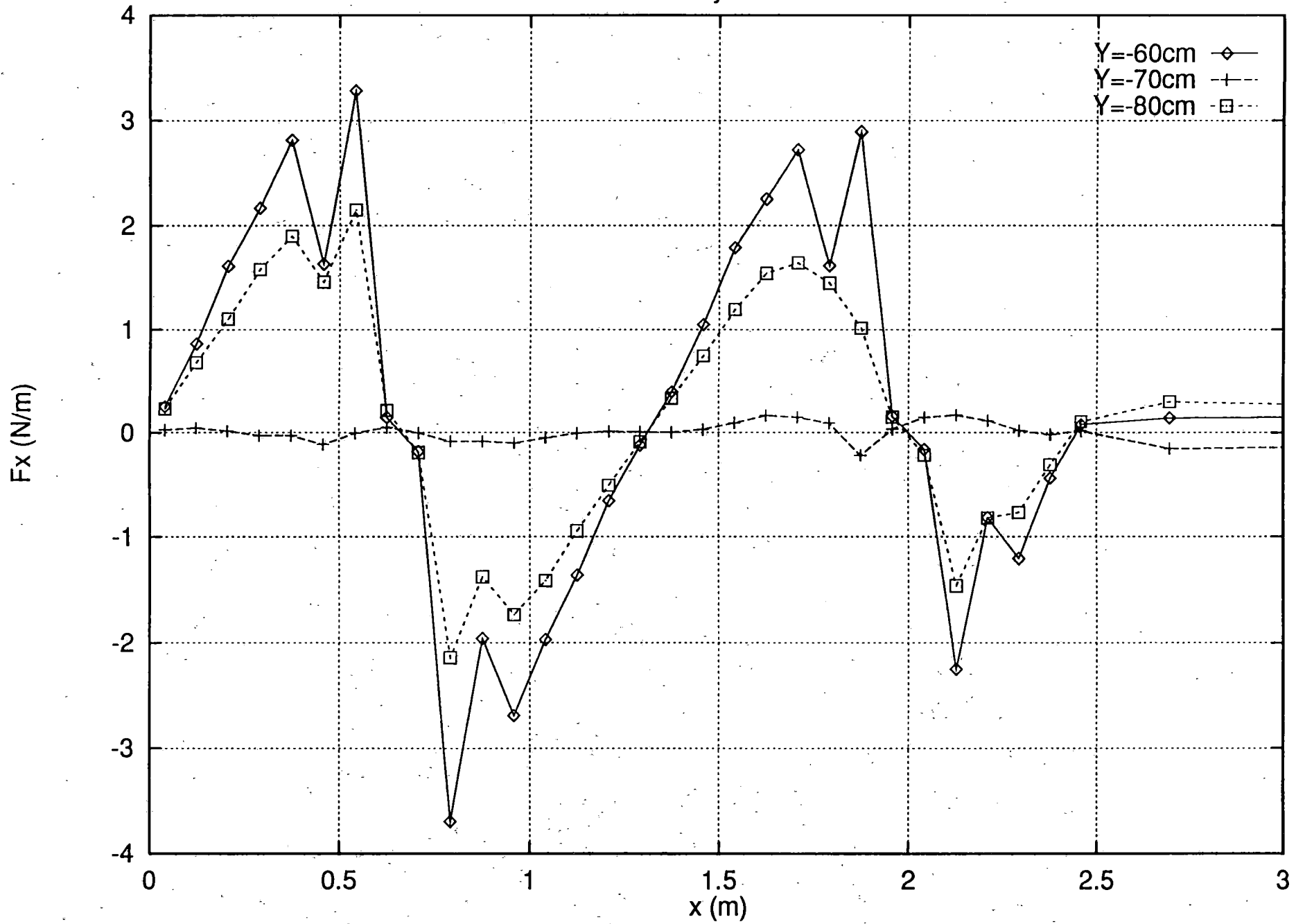
Foster-Miller Guideway Inside Rebars Z = -0.5



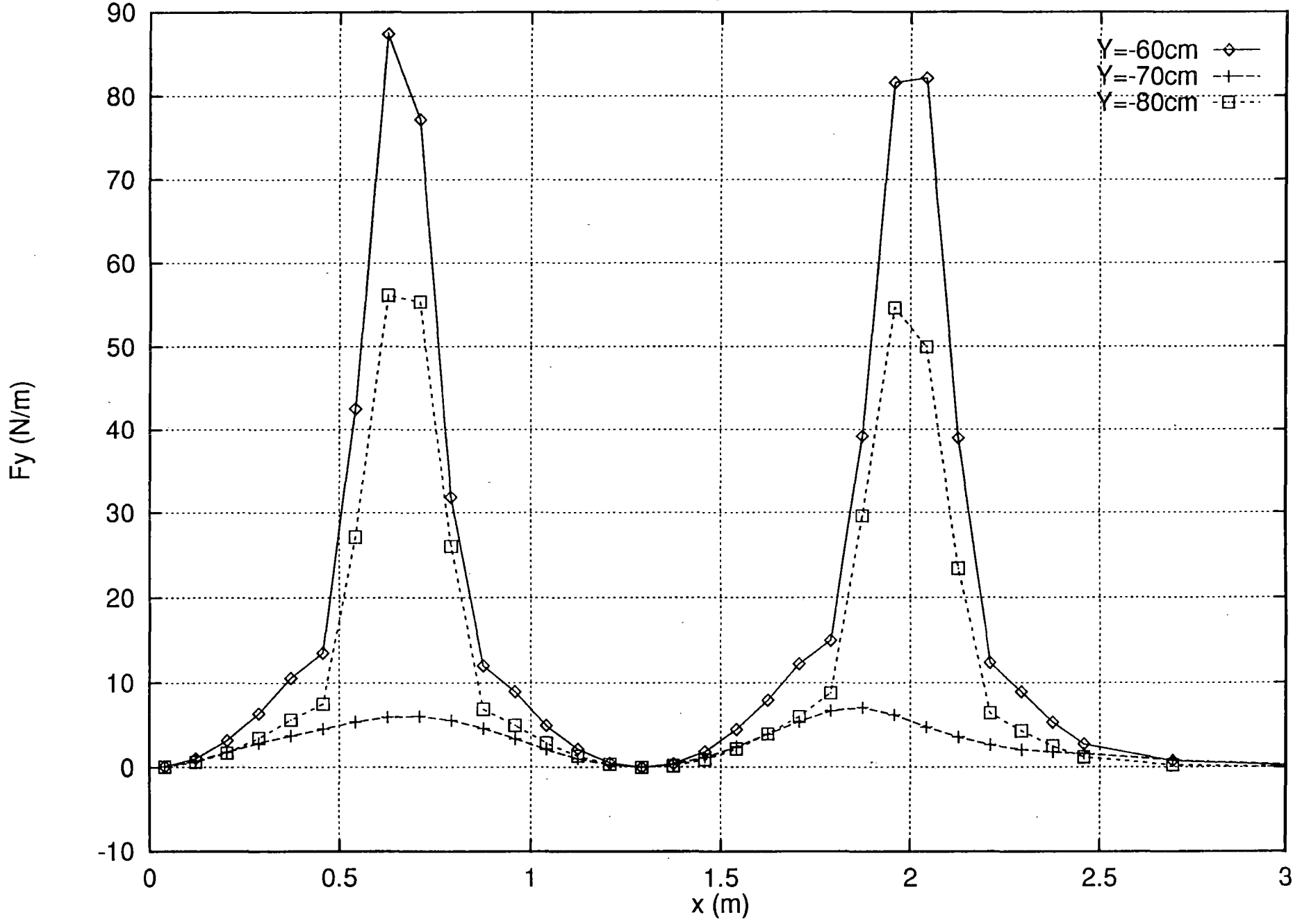
Foster-Miller Guideway Inside Rebars Z = -0.5



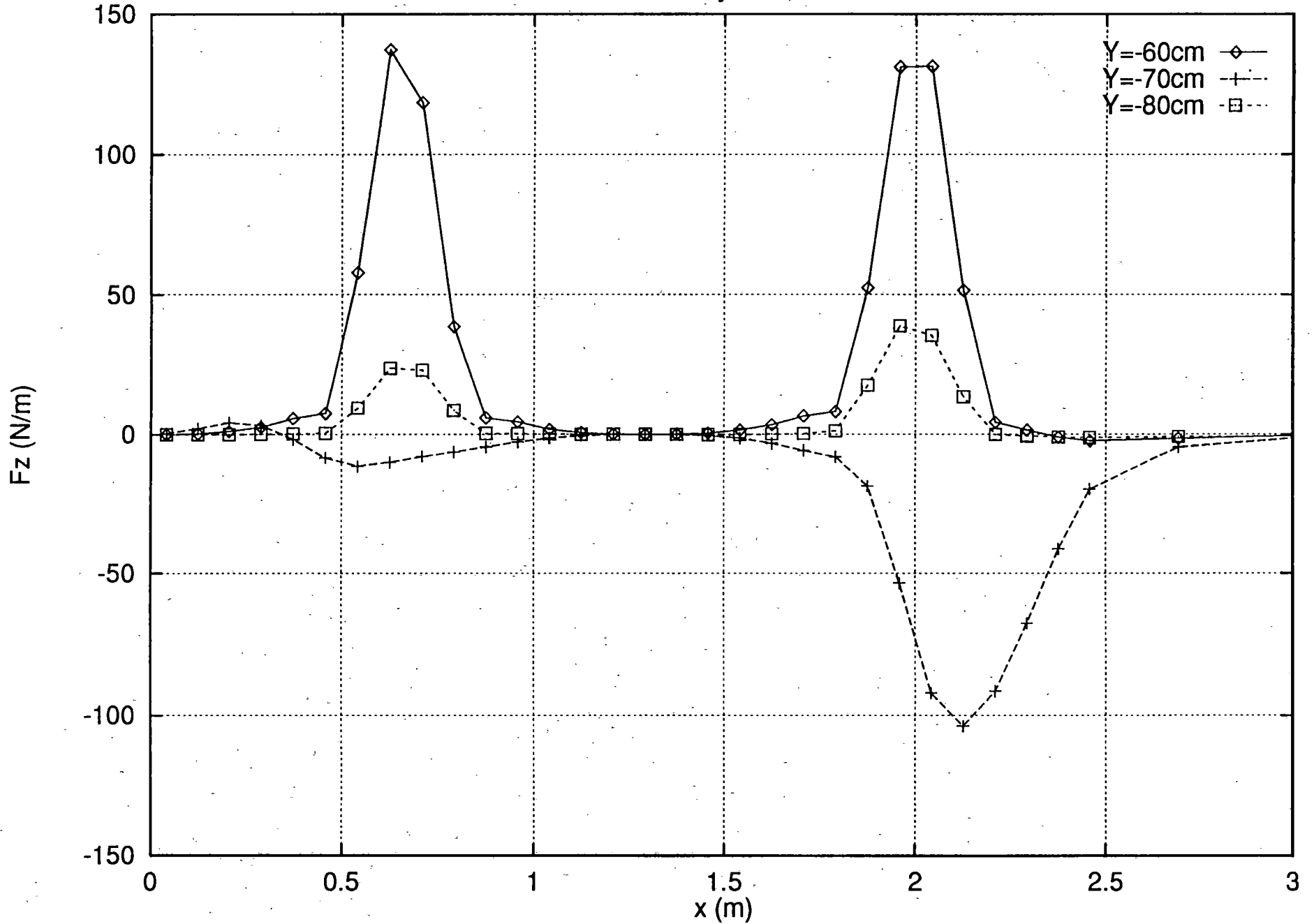
Foster-Miller Guideway Inside Rebars Z = 0.0



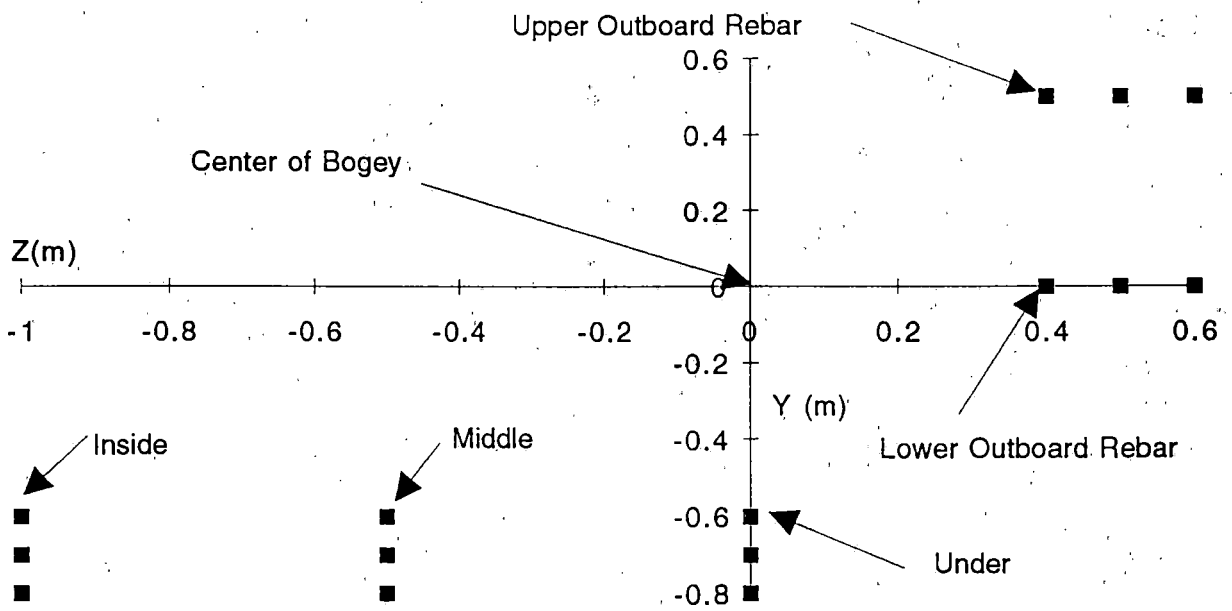
Foster-Miller Guideway Inside Rebars Z = 0.0



Foster-Miller Guideway Inside Rebars Z = 0.0



End View of Foster-Miller Guideway With Rebar Location



**ELECTROMAGNETIC EFFECTS ON REBARS
IN MAGLEV GUIDEWAYS**

SHORT REPORT ON "*BOND FATIGUE*"

Thanasis C. Triantafillou

June 26, 1994

GENERAL

Steel reinforcing bars in Maglev guideways are subjected to both *mechanical* forces due to external loads (e.g. dead loads, vehicle-guideway interaction loads, wind, snow, earthquake etc.) and *electromagnetic* forces caused by the presence of high fields near the magnets. For instance, for the typical rebar installation shown in Fig. 1 (Bechtel/MIT's guideway concept), the top rebars in the webs are subjected to relatively high frequency electromagnetic forces acting normal to the rebars, superimposed on larger and lower frequency cyclic mechanical forces acting along the rebar axes.

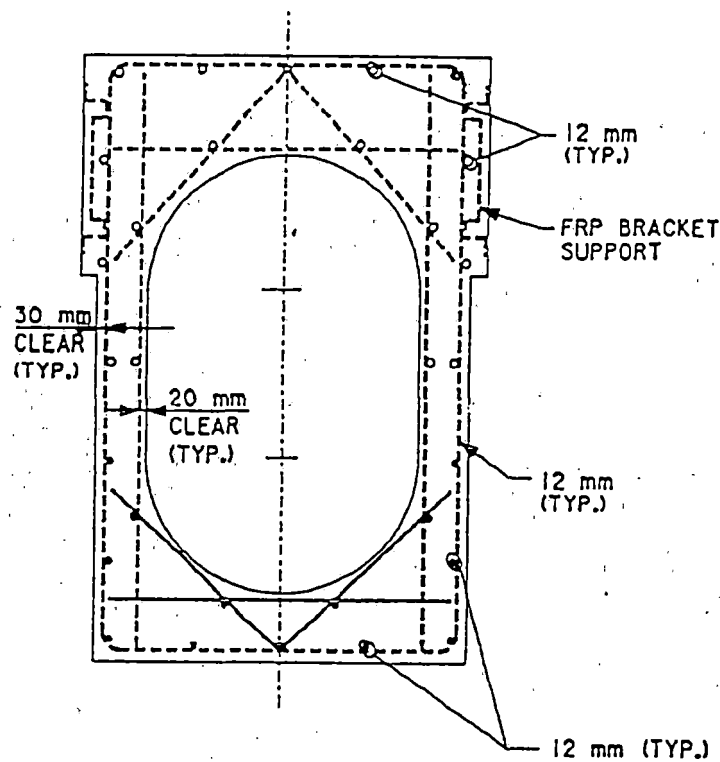


Fig. 1 Typical cross section in Bechtel/MIT's guideway.

The objective of this work is to provide an understanding of the rebar-concrete bond behavior due to cyclic loads, to provide guidelines for determining the force limits before bond fatigue becomes critical, and to suggest experimental procedures that may give answers to problems that cannot be solved based on existing analytical models and existing knowledge of structural behavior.

EFFECT OF LOW FREQUENCY MECHANICAL FORCES

The action of cyclic mechanical force on rebars is illustrated schematically in Fig. 2.

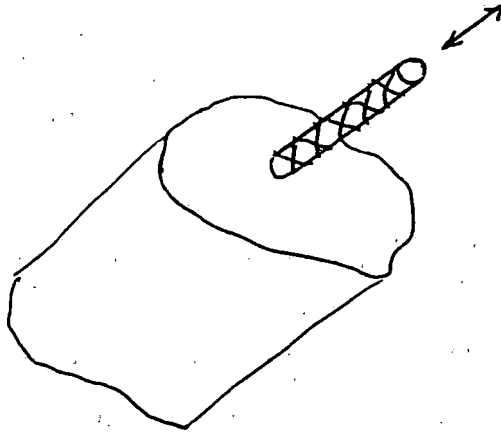


Fig. 2 Action of low frequency mechanical forces on rebars.

When bond failure ensues, it results generally in splitting of the concrete along the rebars, either in vertical or in horizontal planes. Such splitting comes chiefly from wedging action when the ribs of the rebars bear against the concrete. When splitting spreads all the way to the end of an anchored bar, complete bond failure occurs, by sliding of the steel relative to the concrete. The above mechanism will be analyzed considering a vibration frequency in the range 2-10 Hz, and a number of cycles in the order of 10^6 . The problem under consideration is not new to civil engineers; it has been analyzed quite extensively, and the literature is rich in information on both experimental and analytical studies (e.g., references at the end of this report).

For modern deformed bars, tests seem to indicate that splitting occurs when the total bond force U per unit length of a rebar, which is transmitted from steel to concrete, reaches a critical value U_{bs} (Fig. 3). This ultimate bond force is largely independent of bar size or perimeter. The concept of a wedging action is in reasonable conformity with this finding, since the effects of a wedge of given shape depend more on the force with which it is driven than on its size.

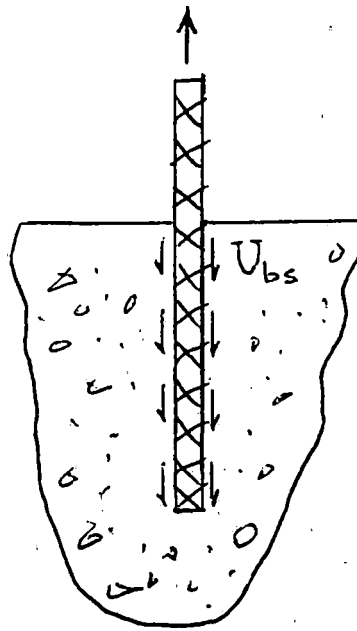


Fig. 3 Ultimate bond force (or bond strength).

It has been found that the ultimate average bond force per unit length (N/mm) of bar is approximately

$$U_{bs} = 75\sqrt{f'_c} \quad (1)$$

where f'_c is the compressive strength of concrete (in MPa). Hence, the minimum rebar length which is necessary to develop, by bond, a given bar force $A_b f_s$ is $A_b f_s / U_{bs}$ (A_b =rebar cross section area, f_s =rebar stress). In particular, in order to ensure that a bar is securely anchored by bond to develop its maximum usable strength (the yield stress, f_y), this length must be approximately $l_d = A_b f_y / U_{bs}$, which is called *development length*. From this discussion it is seen that the main requirement for safety against bond failure is that the length of the rebar, from any point of given steel stress (at most f_y) to its nearby free end must be at least equal to l_d . If this requirement is satisfied, the magnitude of bond stresses is only of secondary importance, since the integrity of the member is assured even in the face of possible minor local bond failures. If the actual available length is inadequate for full development, special anchorage, such as by hooks, must be provided to ensure adequate strength.

Some of the key issues found in the literature with regard to bond fatigue are listed next:

- Both the mean load and the load range are important in determining the number of cycles to failure for a given frequency.
- The number of load reversals until bond fatigue failure occurs increases with decreasing the maximum load and/or increasing the lower load.
- The fatigue strength of bond corresponds to the fatigue strength of centrally loaded concrete. This means that no bond fatigue failure will occur during several million load reversals if for the usual anchorage lengths required for reinforcing bars the maximum load is smaller than about 50% of the static pullout load (bond strength).
- If no fatigue failure occurs, a repeated load has only an influence on the bond behavior under service load. The increase of slip between steel and concrete causes a decrease of the local bond stiffness. The result is a redistribution of the forces along the anchorage length, which can also be expected under a sustained load of the same magnitude.

Making use of the important conclusion that the fatigue strength of bond corresponds to the fatigue strength of plain concrete subjected to uniaxial compression, the same models describing concrete fatigue can be adopted to characterize bond fatigue. A simple and yet reliable modeling approach is based on the "Smith" diagrams, such as that given in Fig. 4 for two million cycles in the range of frequencies between approximately 4-7 Hz.

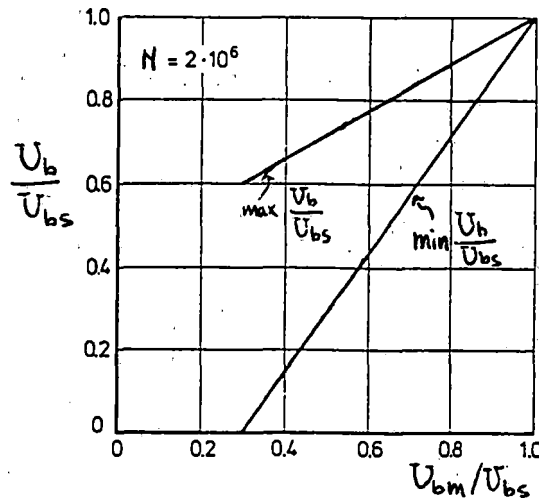


Fig. 4 "Smith" diagram adopted to describe bond fatigue due to mechanical forces.

In the diagram of Fig. 4, U_{bm} is the mean bond force per unit length, and U_b is the maximum or minimum bond force per unit length (depending on which line is used to determine it). Hence, for a given rebar anchorage length, the diagram gives the relationship between the mean, the maximum and the minimum forces that can be carried safely for the particular frequency range and number of cycles considered. As such, it can be used not only as a valuable design tool, but also as a means of checking the bond strength of a given design. The above procedure is illustrated next in an example.

A #6 rebar (diameter = 6/8", area=284 mm²) made of Grade 60 steel ($f_y=414$ MPa=60 ksi), is embedded in concrete with compressive strength $f'_c=41.4$ MPa (=6000 psi). It is assumed that at a critical section the rebar is subjected to a rather high axial force with a mean value of 70 kN, while the associated anchorage length is 355 mm (as provided by the ACI Code of Practice). Equation (1) gives $U_{bs}=480$ N/mm, and U_{bm} is calculated as $70 \times 10^3 / 355 = 200$ N/mm. Hence, $U_{bm} / U_{bs} = 200 / 480 = 0.42$, and from Fig. 4 $U_{b,min} / U_{bs} = 0.17$ and $U_{b,max} / U_{bs} = 0.67$. Finally, the minimum rebar force is calculated as $0.17 \times 480 \times 355 = 28,000$ N = 28 kN, and the maximum force as $0.67 \times 480 \times 355 = 112,000$ N = 112 kN. In summary, two million load reversals will not cause bond fatigue failure as long as the rebar force (with a mean value of 70 kN) is in the range 28-112 kN. It is clear that the design can always be improved (in case the max. and min. forces lie outside the above range) by changing the anchorage length.

EFFECT OF HIGH FREQUENCY ELECTROMAGNETIC FORCES

The action of cyclic electromagnetic forces on rebars is illustrated schematically in Fig. 5.

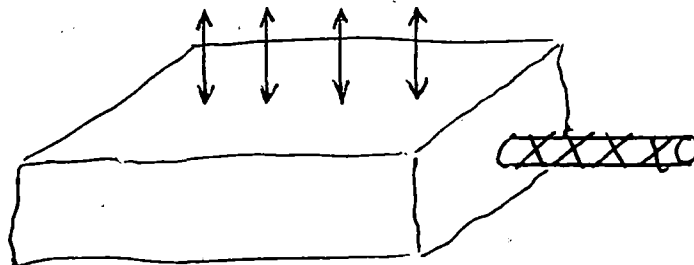


Fig. 5 Action of high frequency electromagnetic forces on rebars.

Typical frequencies are expected to be in the range 20-100 Hz, with a number of cycles in the order of $N=10^8$. Preliminary calculations indicate that the transverse rebar forces will result in stresses perpendicular to the surface of the rebars in the order of a few (less than 2-3) MPa. These stress levels are considered to be low, and the likelihood of bond degradation is estimated to be negligible. However, no experimental results can be found in the literature addressing the problem of bond fatigue due to transverse loads. The best approach to quantify the bond fatigue caused by transverse loading would be to design a set of experiments. These experiments could be performed according to the sequence given in Fig. 6.

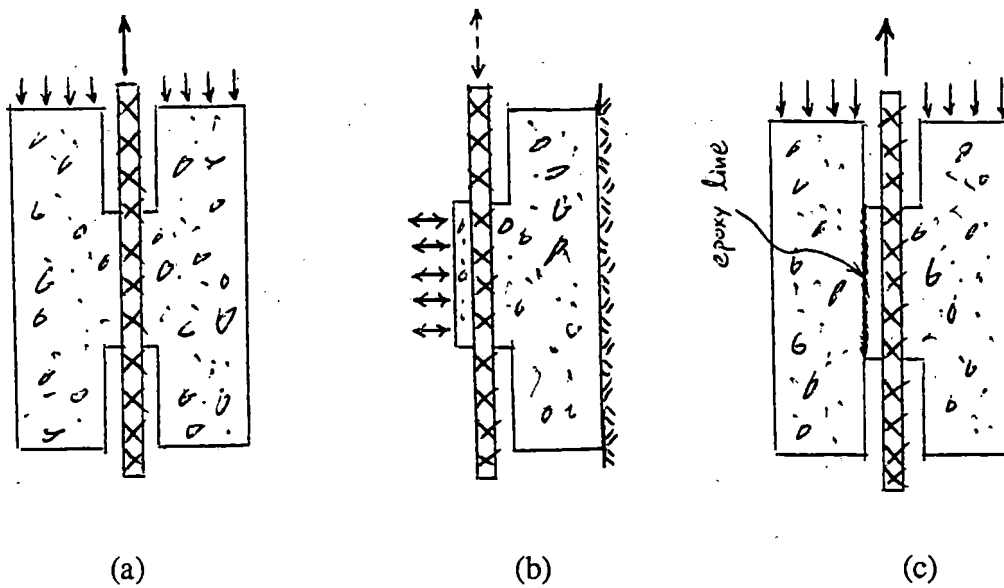


Fig. 6 *Experimental procedure for the measurement of residual bond strength due to transverse loading.*

The experimental procedure should include the following three steps ((a)-(c) in Fig. 6):

- (a) Measurement of static bond strength.
- (b) Application of electromagnetic force cycling at high frequencies (as expected in the real structure), for $N \sim 10^8$, and at transverse force levels analogous to those expected in the top reinforcing rebars.
- (c) Modification of concrete specimen to measure the residual bond strength.

It is recommended that step (b) be performed both without and with the presence of a cyclic axial rebar force, so that the effect of simultaneous action of the two kinds of forces can be quantified.

DISCUSSION-CONCLUSIONS

For the case of low frequency mechanical forces, the whole issue of bond fatigue becomes really an issue of selecting the appropriate rebar anchorage length. Rebar designs should be such that the expected forces always lie within the "safe" region of "Smith" diagrams such as that shown in Fig. 4. For the Bechtel/MIT guideway concept, where the rebars under consideration are primarily in the compressive zone and the guideway's primary reinforcing elements are prestressing tendons, it is expected that the rebar forces will be minimal, keeping the bond stresses well below 50% of the static bond strength. Under these circumstances bond fatigue is not considered to be a critical design consideration.

Extrapolating the conclusion commonly found in the literature that "bond fatigue is analogous to plain concrete fatigue" to the case of high frequency but low magnitude electromagnetic forces acting transversely to the rebars, it is expected that bond degradation will not be of major concern in this case. However, such a statement has to be verified along the lines of the experimental procedure described above.

SELECTED REFERENCES ON BOND FATIGUE

- (1) Diederichs, U. and Schneider, U. (1982). "Changes in bond behavior due to elevated temperatures", in *Bond in Concrete*, ed. by P. Bartos, ASP, London, 229-238.
- (2) Gambarova, P. G. and Karakoc, C. (1982). "Shear-confinement interaction at the bar-to-concrete interface", in *Bond in Concrete*, ed. by P. Bartos, ASP, London, 82-96.
- (3) Hawkins, N. M. (1974). "Fatigue characteristics in bond and shear of reinforced concrete beams", ACI SP-41 *Fatigue of Concrete*, 203-236.

- (4) Hawkins, N. M., Lin, J. J. and Jeang, F. L. (1982). "Local bond strength of concrete for cyclic reversed loadings", in *Bond in Concrete*, ed. by P. Bartos, ASP, London, 151-169.
- (5) Holmen, J. O. (1982). "Fatigue of concrete by constant and variable amplitude loading", ACI SP-41 *Fatigue of Concrete*, 71-110.
- (6) Ismail, M. A. F. and Jirsa, J. O. (1972). "Bond deterioration in reinforced concrete subjected to low cycle loads", ACI Journal 69-34, 334-343.
- (7) Perry, E. S. and Jundi, N. (1969). "Pullout bond stress distribution under static and dynamic repeated loadings", ACI Journal 66-28, 377-380.
- (8) Rehm, G. and Eligehausen, R. (1979). "Bond of ribbed bars under high cycle repeated loads", ACI Journal 76-5, 297-309.
- (9) Royles, R., Morley, P. D. and Khan, M. R. (1982). "The behavior of reinforced concrete at elevated temperatures with particular reference to bond strength", in *Bond in Concrete*, ed. by P. Bartos, ASP, London, 217-228.
- (10) Sager, H. and Rostasy, F. S. (1982). "The effect of elevated temperature on the bond behavior of embedded reinforcing bars", in *Bond in Concrete*, ed. by P. Bartos, ASP, London, 206-218.
- (11) Stroeven, P. and Wind, G. (1982). "Structural and mechanical aspects of debonding of a steel bar from a cementitious matrix", in *Bond in Concrete*, ed. by P. Bartos, ASP, London, 40-59.

**Static forces on Rebars
for the
Foster-Miller Magnet-Guideway Geometry**

R. D. Pillsbury, Jr.

7 December 1994

This document and all reports and memoranda in this series are intended as a record of work in progress. They are for use in informal discussions of design, fabrication and further computation alternatives. This material is subject to change and should not, therefore, be published or referred to in the open literature. Conclusions are preliminary and distribution should be strictly limited.

Massachusetts Institute of Technology
Plasma Fusion Center
Cambridge MA 02139

To: J. R. Hale
From: R. D. Pillsbury, Jr.
Subject: Static forces on Rebars for the Foster Miller Magnet-Guideway Geometry

REF: PFC-RM-010

The magnetostatic forces that would be experienced by magnetically permeable reinforcing bars that may be in the guideway proposed for the Foster-Miller Maglev system has been assessed. Rebars in a number of different locations were evaluated to ascertain the sensitivity of the forces to the location within the guideway. A parallel study was performed for the Bechtel guideway design¹.

The Foster-Miller onboard magnet system consists of 2 bogeys on each side of the vehicle with 4 coils in each bogey. The polarity of the coils changes in a from magnet to magnet. The coils on either side of the vehicle oppose each other, that is, they have the opposite sign of current.

A three dimensional, magnetostatic analysis was performed using the finite element program ANSYS². Therefore, the results presented in this memorandum correspond to the case of the vehicle at rest, *i.e.*, zero speed. It is assumed that there is no interaction with the levitation windings in the guideway. The fields from the LSM are also ignored. The analysis was performed on a single rebar at a time. There were fifteen separate runs of differing distances from the coils. There are six bar positions in the out vertical legs of the U-shaped guideway and nine positions along the bottom of the guideway.

Figure 1 shows four views of the model and the magnetic flux density vectors in a rebar in the vertical leg of the guideway that is centered on the coil and 40 cm away. Symmetries of the coils and rebar imply that these results are equally valid for bars in the negative y-direction.

In this analysis, the rebar is modeled from the center of one bogey a plane of symmetry 12.5 m away. The bogey is centered on $X = 0$. There are four elements in the cross-section of the rebar.

In the Stress Tensor approach, the surface tractions are calculated. Figure 2 shows the traction vectors acting on the surfaces of the rebar. The net force in a cross-section is the sum of all the tractions on elements in that cross-section. As can be seen, the forces are toward the magnets as would be expected. The variation along the bar is also evident.

The Figures 1 and 2 were for a case of the rebar 40 cm from the center of the magnets (in the -Z direction). The 40 cm. was chosen as the closest possible location for rebars due to the room required for the levitation windings in the guideway, *etc.* Additional analyses were performed for the rebar 50 and 60 cm. from the coils.

The components of the surface tractions were summed at each cross-section along the rebar (X direction). These force components per unit length are displayed in Figures 3 and 4 and show the X-, and Z-directed components for force per unit length as a

¹ PFC-RM-009, "Static forces on rebars for the Bechtel Magnet-Guideway geometry,"

² ANSYS 5.0A, Swanson Analysis Systems, Inc., Houston, PA.

function of distance along the rebar for the cases of the rebar at 40, 50 and 60 cm from the coils. The Y-directed force is zero since the rebar is centered on the coil. The fall-off of the force with distance is quite evident. Figures 5 and 6 replot the data with an X axis extent of 3 m. The truncation of some of the peaks is a result of the discreteness of the finite element mesh. It can be seen that peak localized forces can be on the order of 900 N/m which was approximately the same order of magnitude as in the Bechtel analysis. One major difference is the large X-directed component of load which has a peak local value of 220 N/m.

The components of the force per unit length acting on a rebar 0.5 m above the center of the coils as a function of position along the rebar for the three different Z direction distances from the coils is shown in Figures 7-9. The fall-off of the force with distance is evident, especially in the Z-directed component.

An additional nine locations were evaluated. These corresponded to the "floor" of the U-shaped channel. Positions in the Z direction of -1.0, -0.5, and 0.0 m were evaluated for Y distances of 60, 70 and 80 cm, respectively. Figures 10-12 show the three force components per unit length for the -1.0 m case. Figures 13-15 and 16-18 show the results for the -0.5 m and 0.0 m case, respectively. The later case corresponds to a rebar directly under the coils centers.

The individual components of the force per unit length can be integrated (summed) to get the net force of the rebar (over a half-span length which, because of the fall-off, is roughly equivalent to a half-bogey. Table I presents these sums.

Table I - Net Forces on a Rebar over a Length of One Half Span

Y Distance (m)	Z Distance (cm)	F _x (N)	F _y (N)	F _z (N)
0	40	18	0	-697
	50	10	0	-472
	60	6	0	-326
50	40	4	-201	-82
	50	3	-131	-89
	60	3	-87	-83
-60	-100	0	11	12
-70		1	36	30
-80		0	15	4
-60	-50	1	66	9
-70		3	152	19
-80		0	31	-9
-60	0	1	52	64
-70		0	9	-48
-80		1	33	13

PFC-RM-010: List of Figures

Figure 1. Magnetic Flux Density Vectors in the Rebar of the Foster-Miller Guideway.

Figure 2. Maxwell Stress Traction Vectors Acting on the Rebar of the Foster-Miller Guideway.

Figure 3. F_x versus x for the rebars 40 cm from the bogey.

Figure 4. F_z versus x for the rebars 40 cm from the bogey.

Figure 5. F_x versus x ($0 < x < 3$ m) for the rebars 40 cm from the bogey.

Figure 6. F_z versus x ($0 < x < 3$ m) for the rebars 40 cm from the bogey.

Figure 7. F_x versus x for the upper outboard rebar at various distances from the bogey.

Figure 8. F_y versus x for the upper outboard rebar at various distances from the bogey.

Figure 9. F_z versus x for the upper outboard rebar at various distances from the bogey.

Figure 10. F_x versus x for the inside rebar at various distances from the bogey.

Figure 11. F_y versus x for the inside rebar at various distances from the bogey.

Figure 12. F_z versus x for the inside rebar at various distances from the bogey.

Figure 13. F_x versus x for the middle rebar at various distances from the bogey.

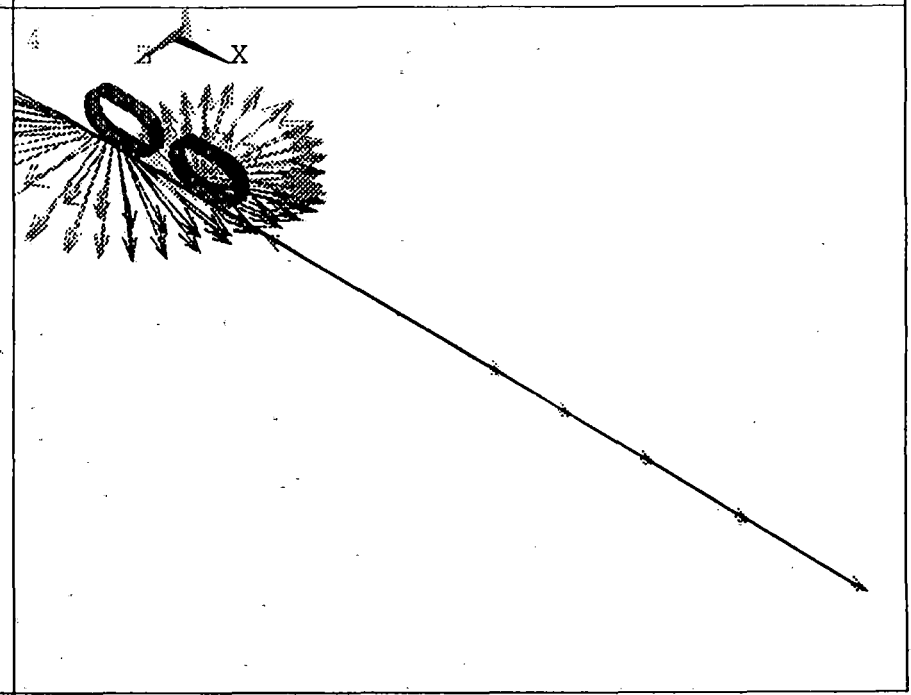
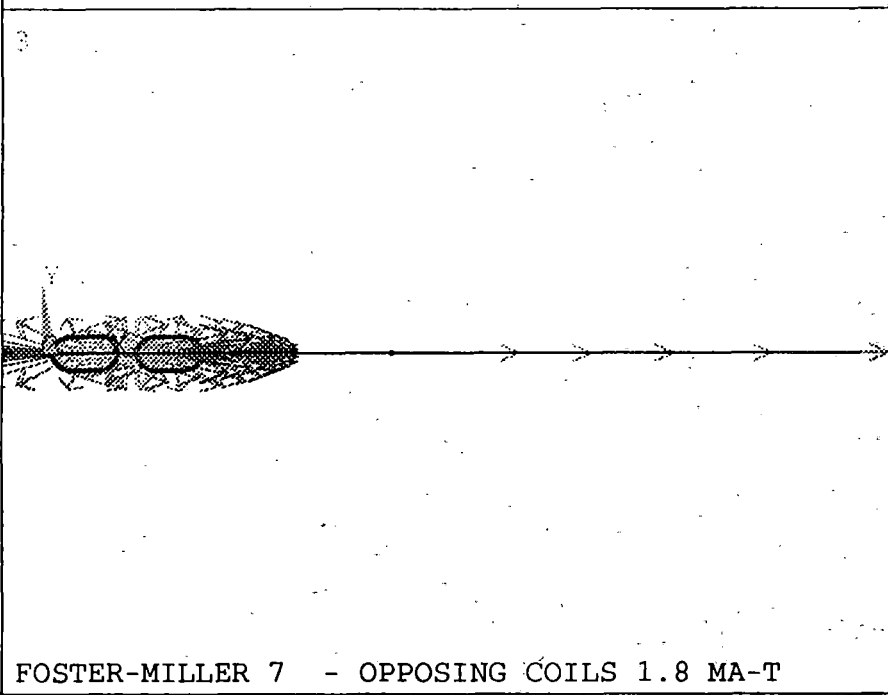
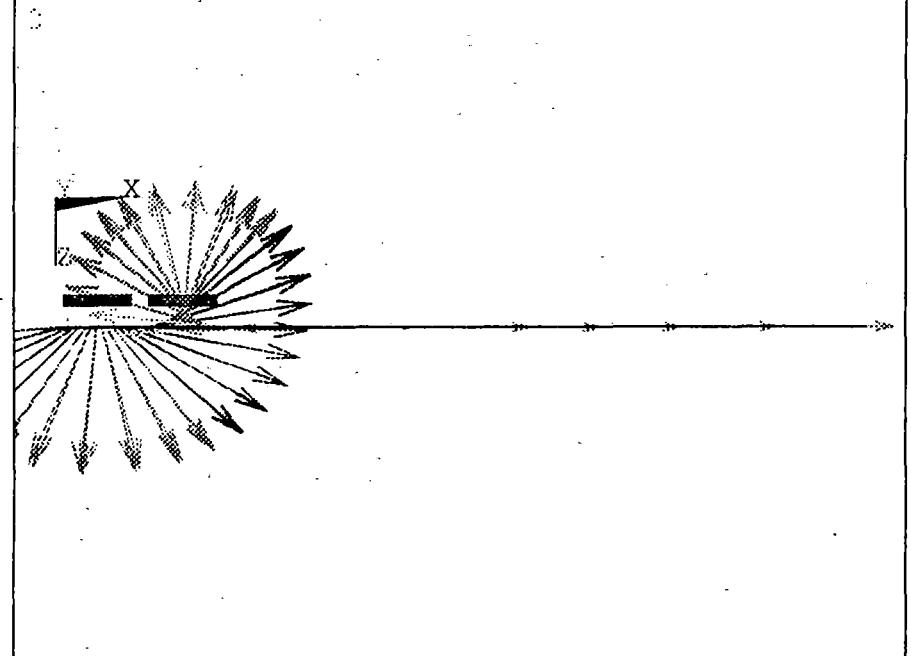
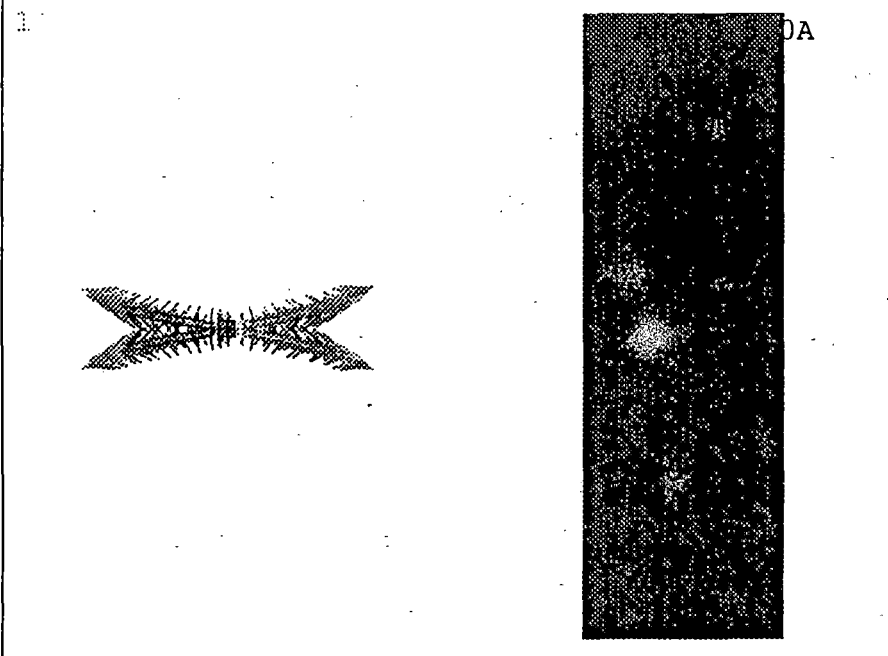
Figure 14. F_y versus x for the middle rebar at various distances from the bogey.

Figure 15. F_z versus x for the middle rebar at various distances from the bogey.

Figure 16. F_z versus x for the under rebar at various distances from the bogey.

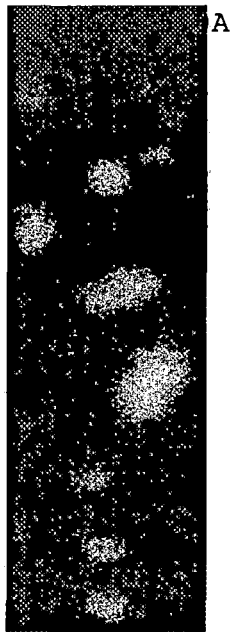
Figure 17. F_x versus x for the under rebar at various distances from the bogey.

Figure 18. F_z versus x for the under rebar at various distances from the bogey.

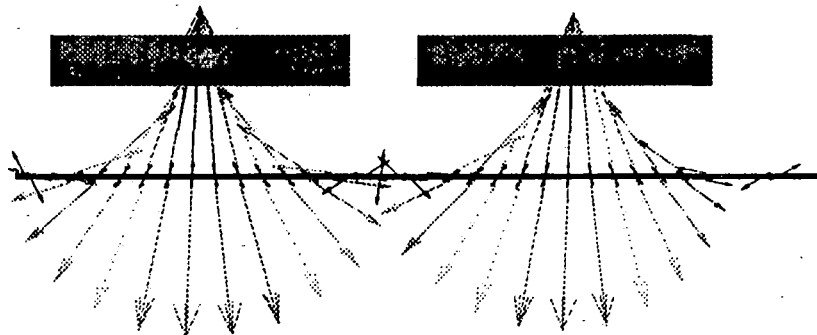


FOSTER-MILLER 7 - OPPOSING COILS 1.8 MA-T

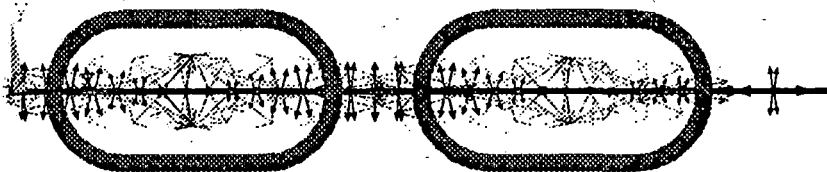
1



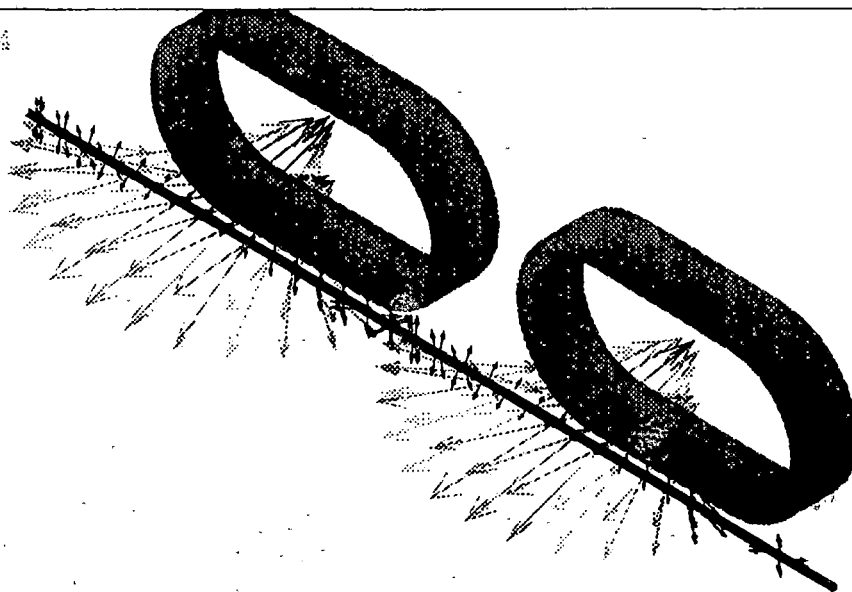
2



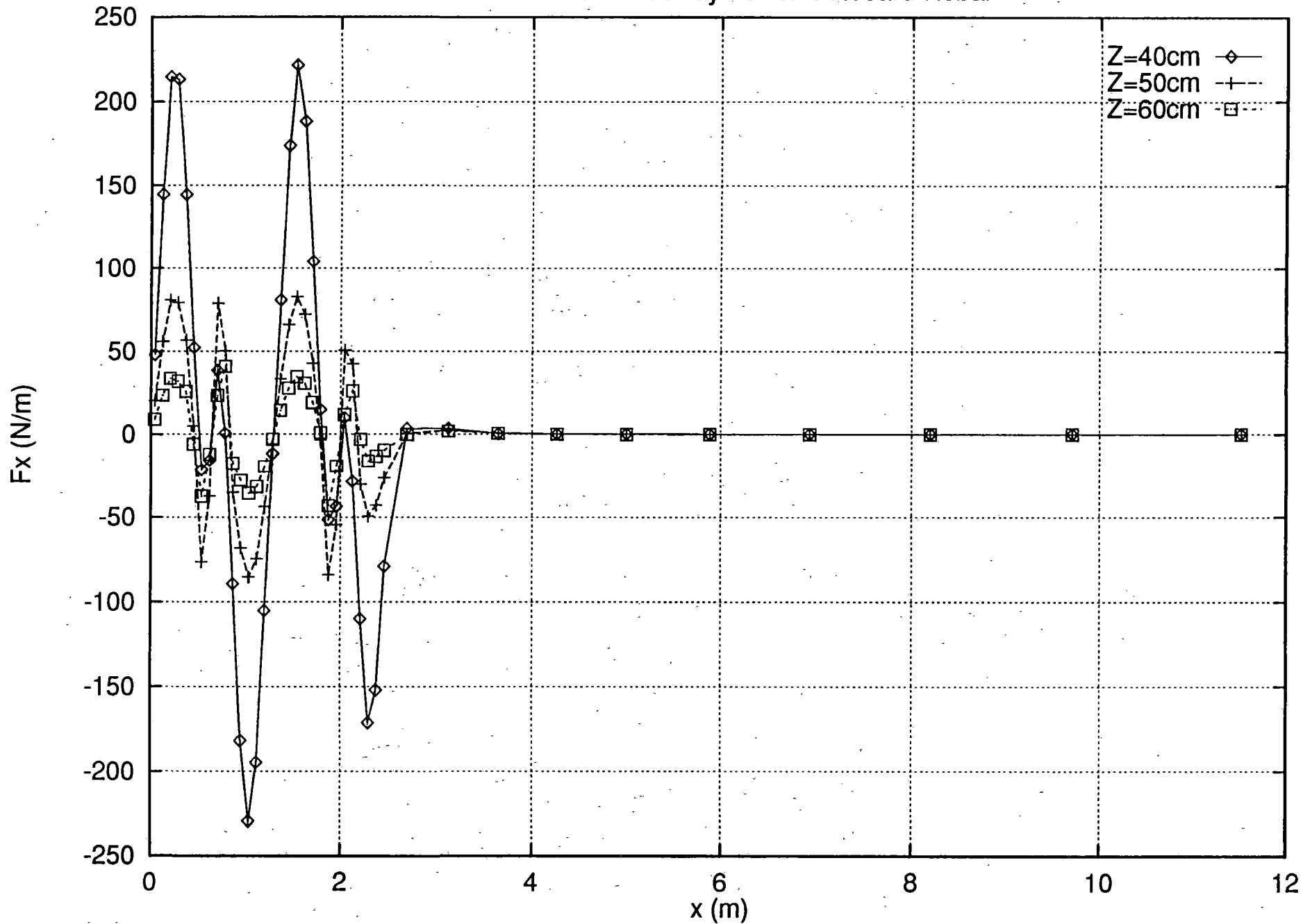
3



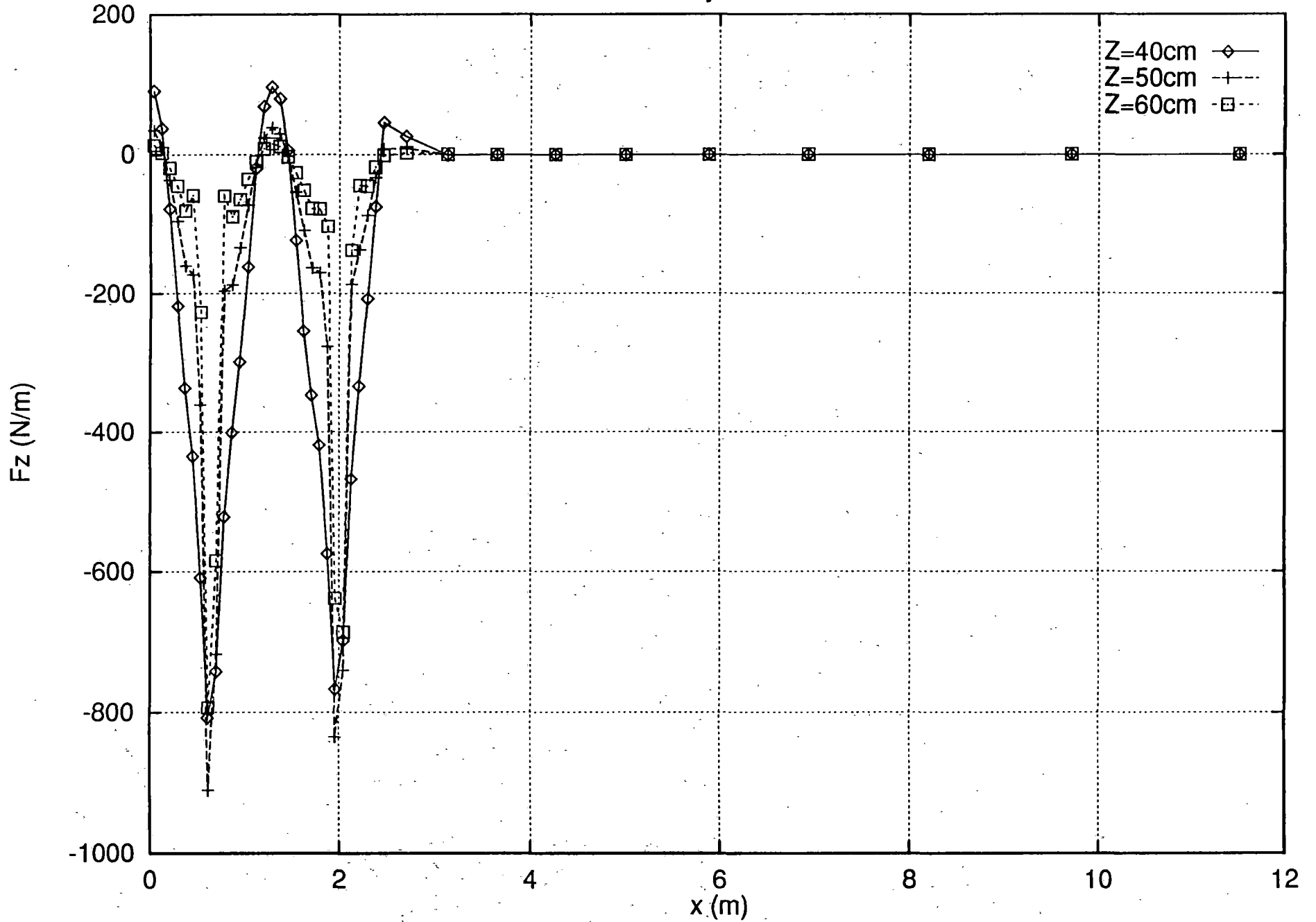
4



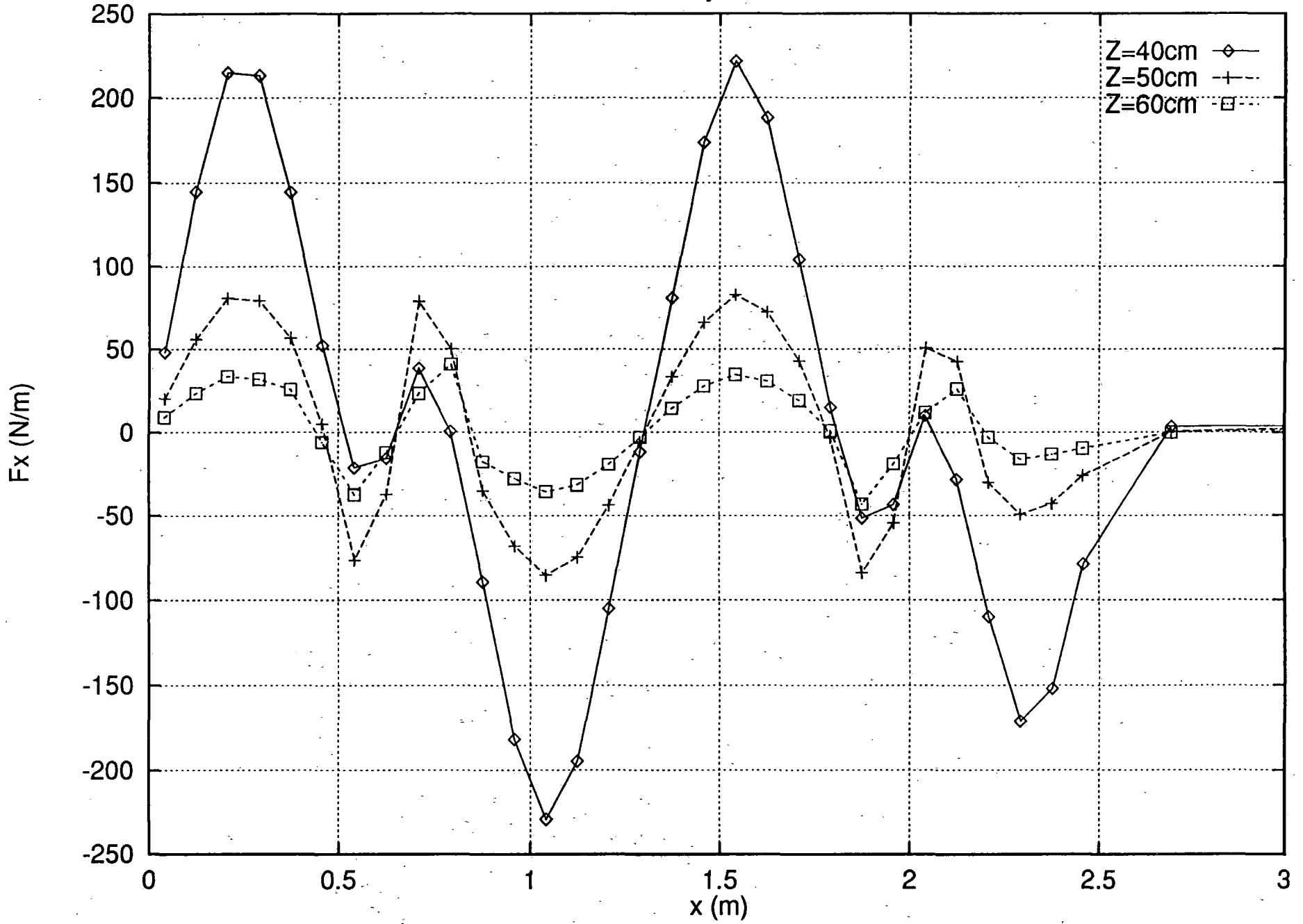
Foster-Miller Guideway Lower Outboard Rebar



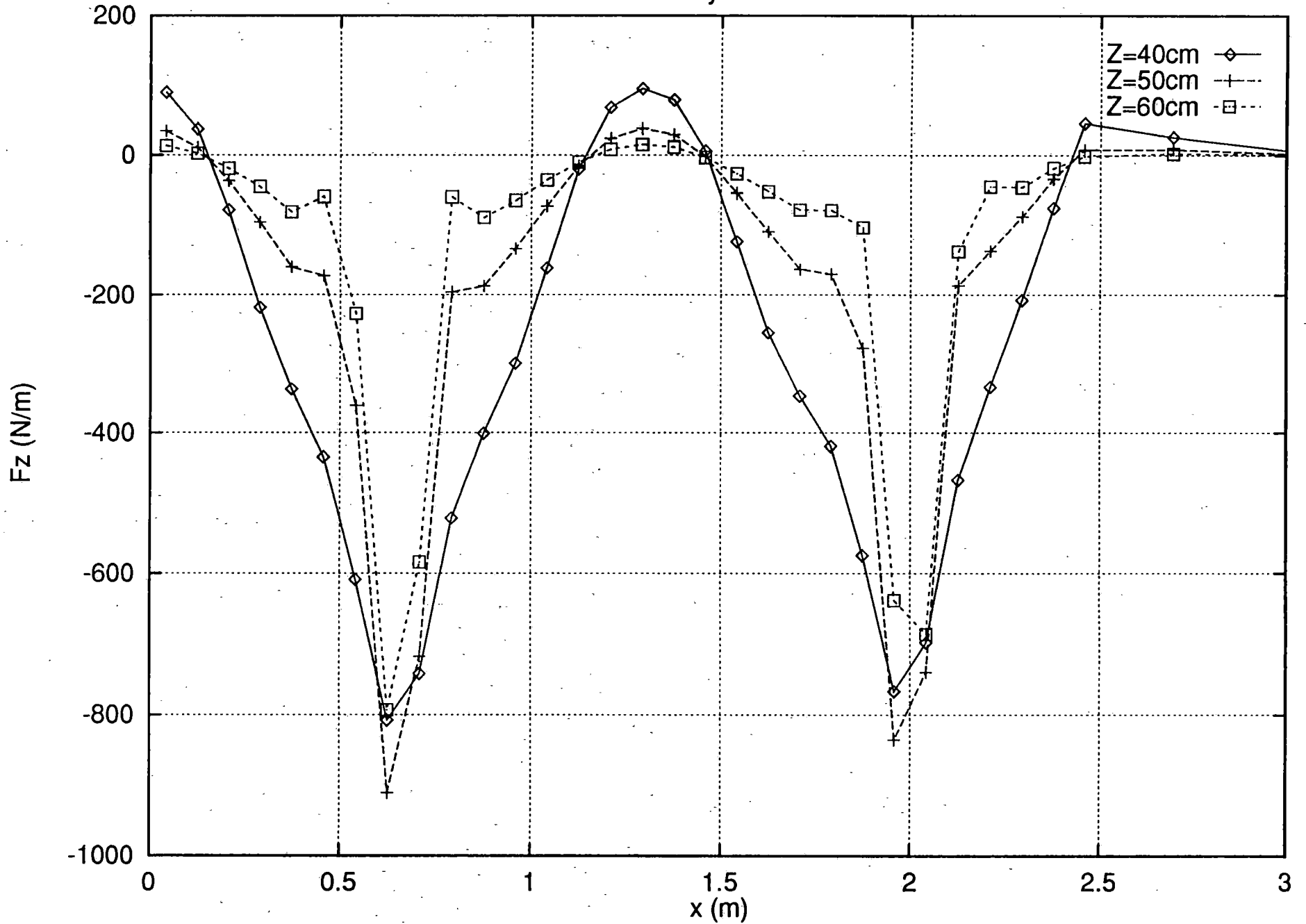
Foster-Miller Guideway Lower Outboard Rebar



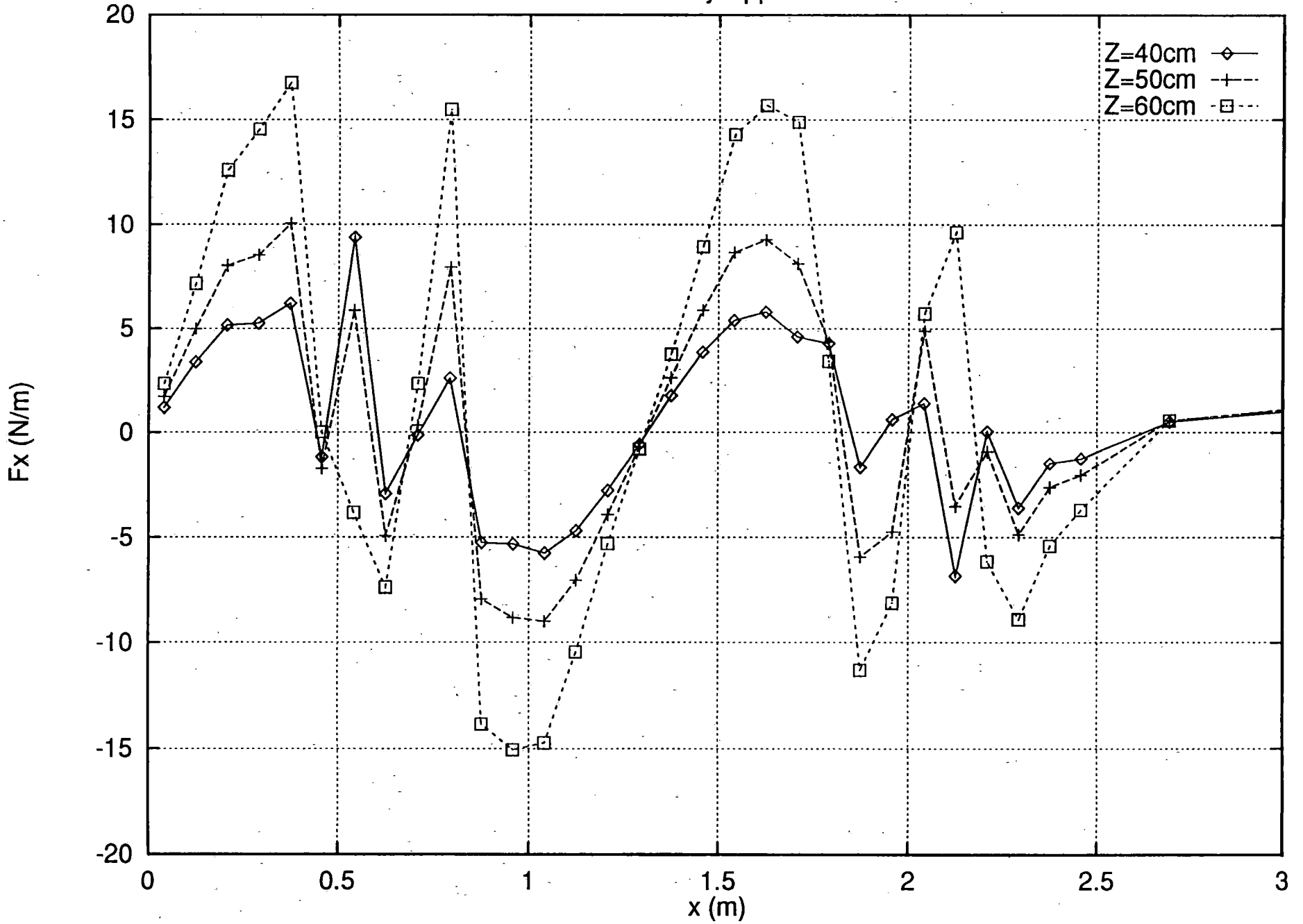
Foster-Miller Guideway Lower Outboard Rebar



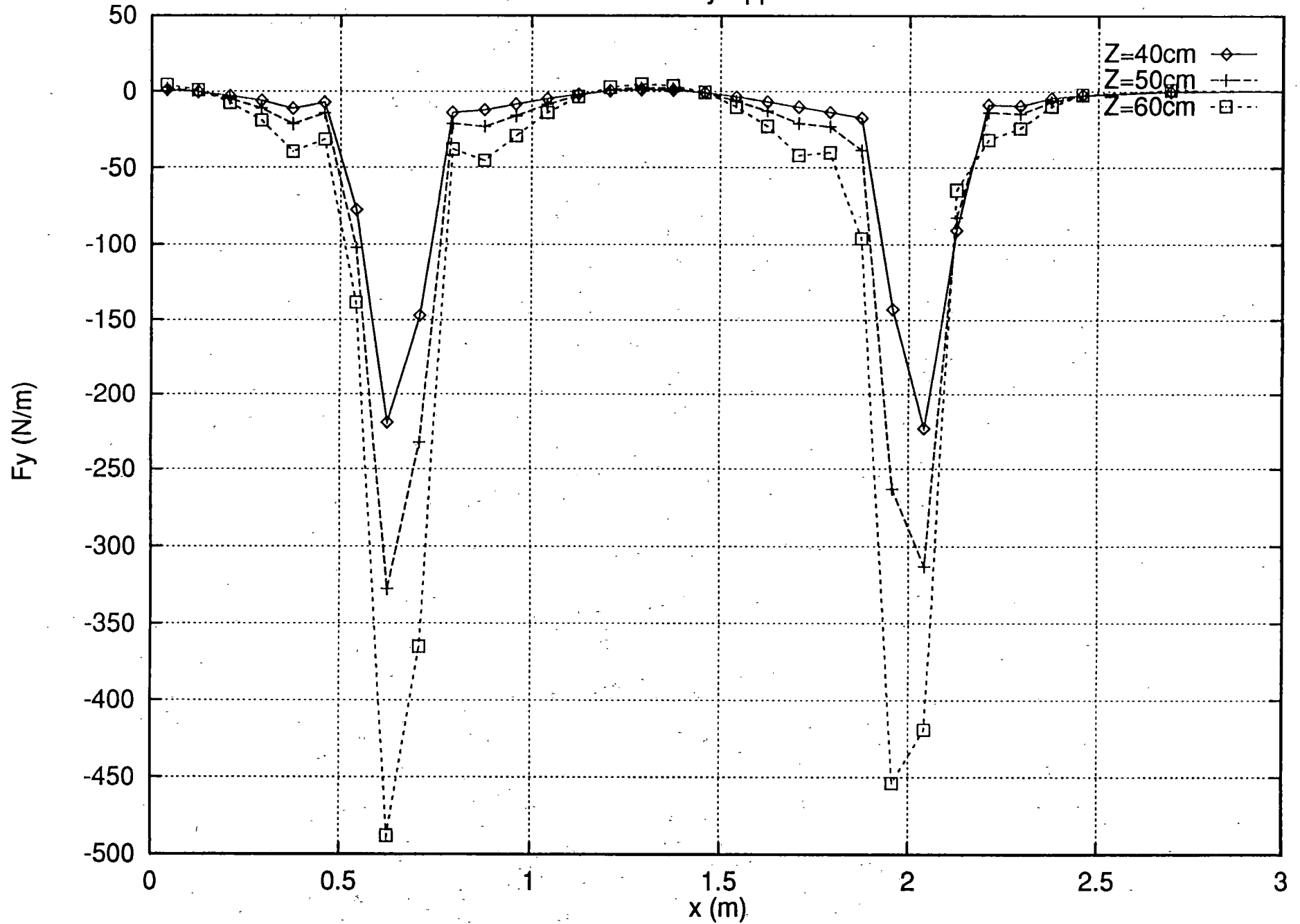
Foster-Miller Guideway Lower Outboard Rebar



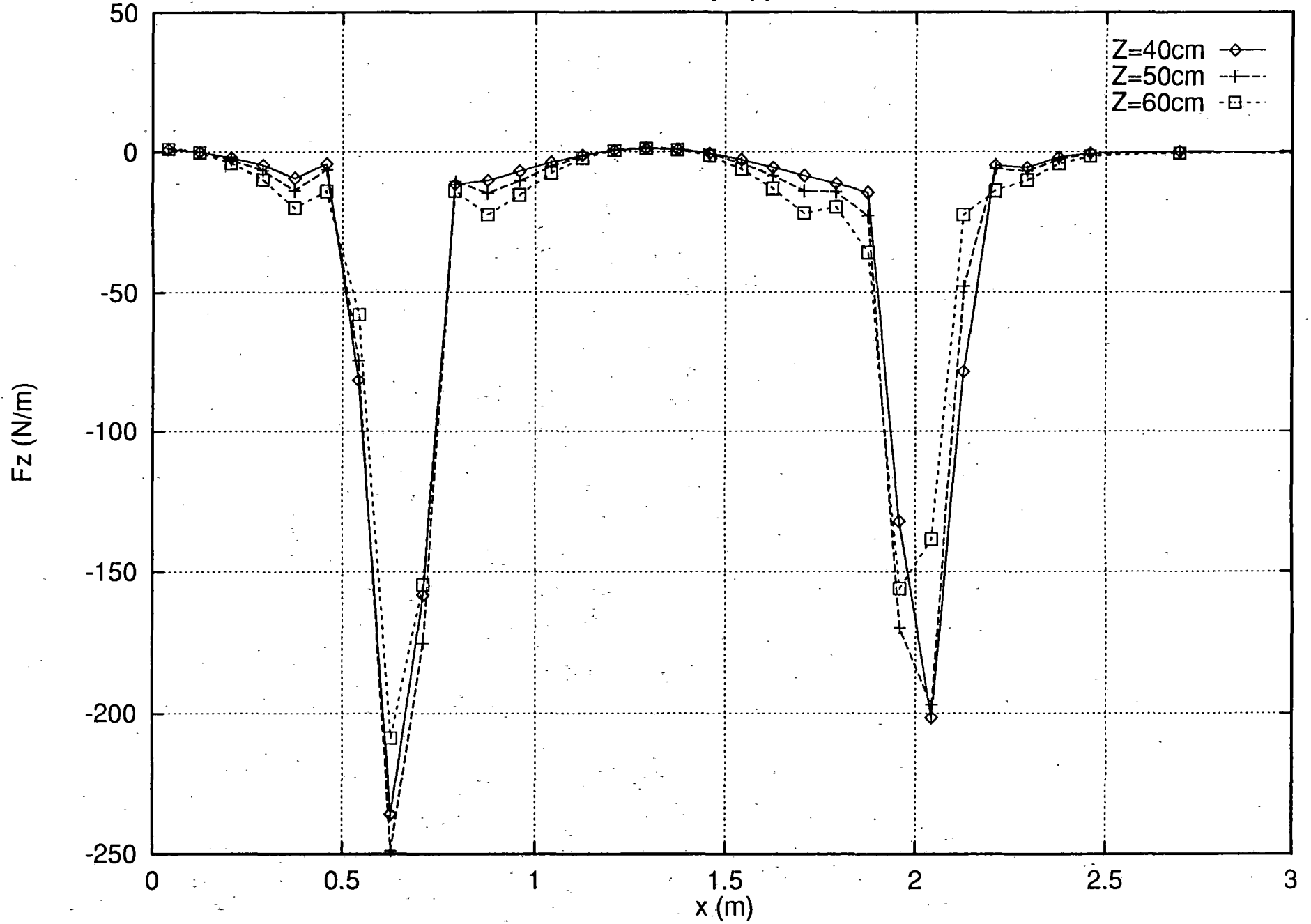
Foster-Miller Guideway Upper Outboard Rebar



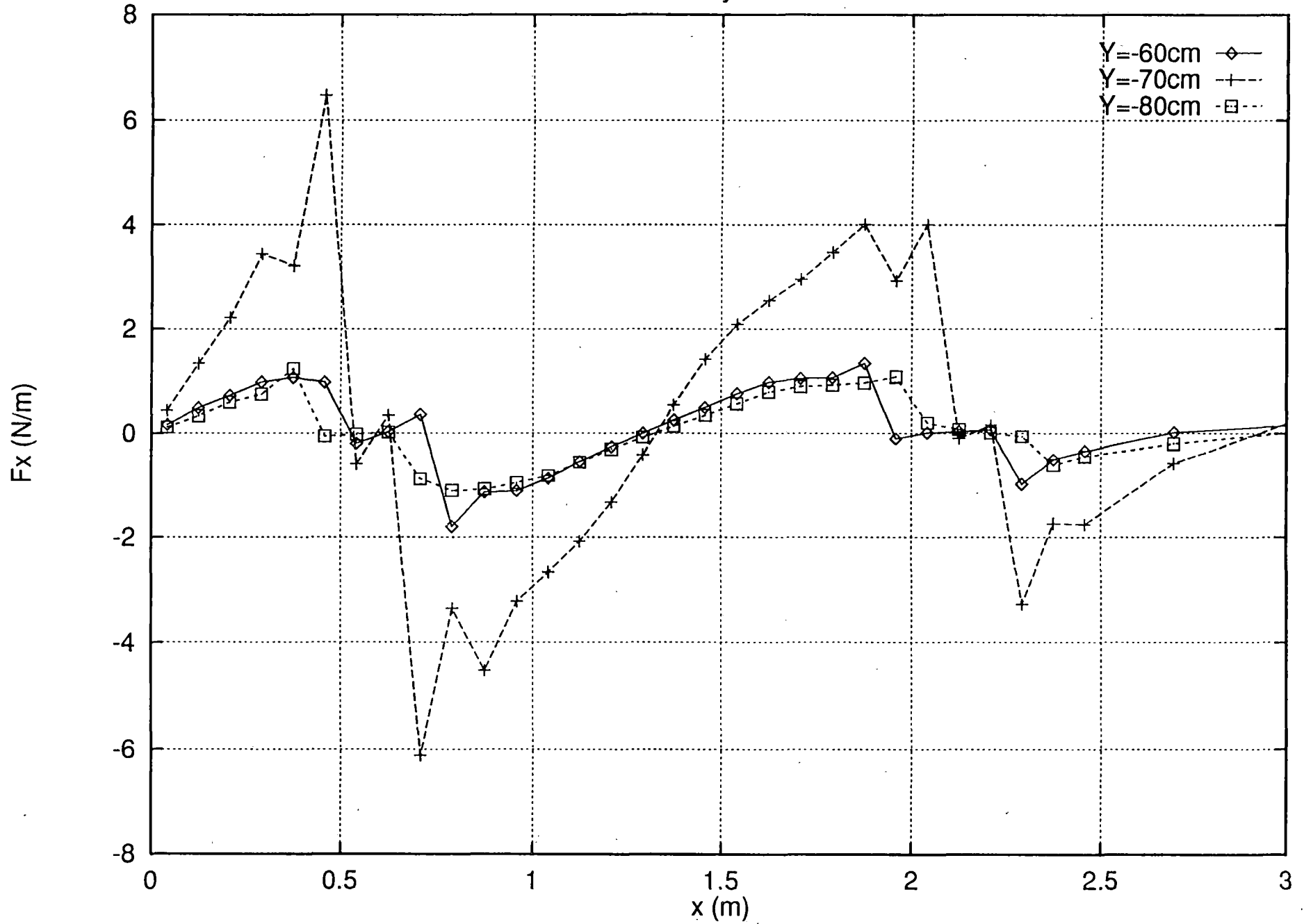
Foster-Miller Guideway Upper Outboard Rebar



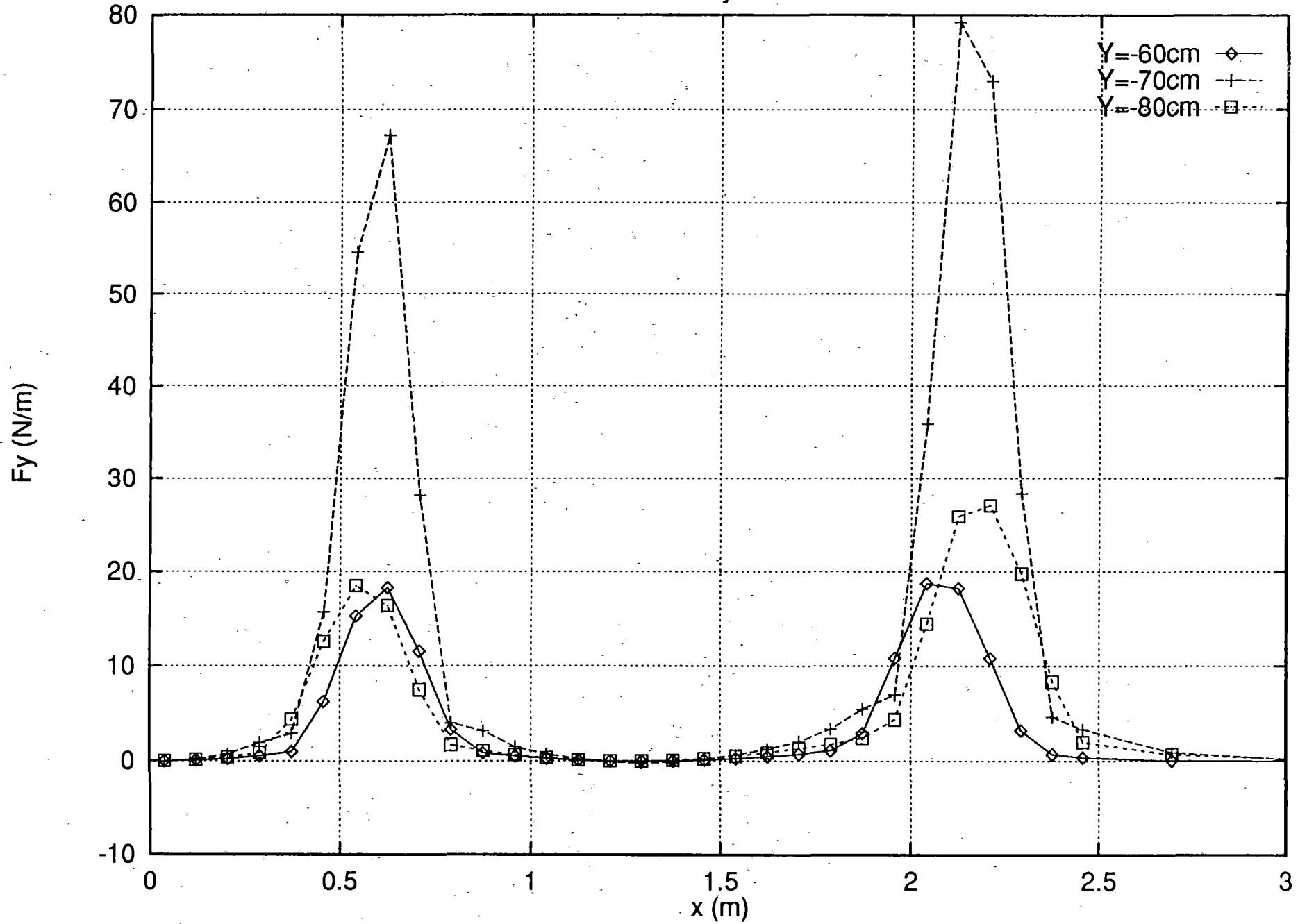
Foster-Miller Guideway Upper Outboard Rebar



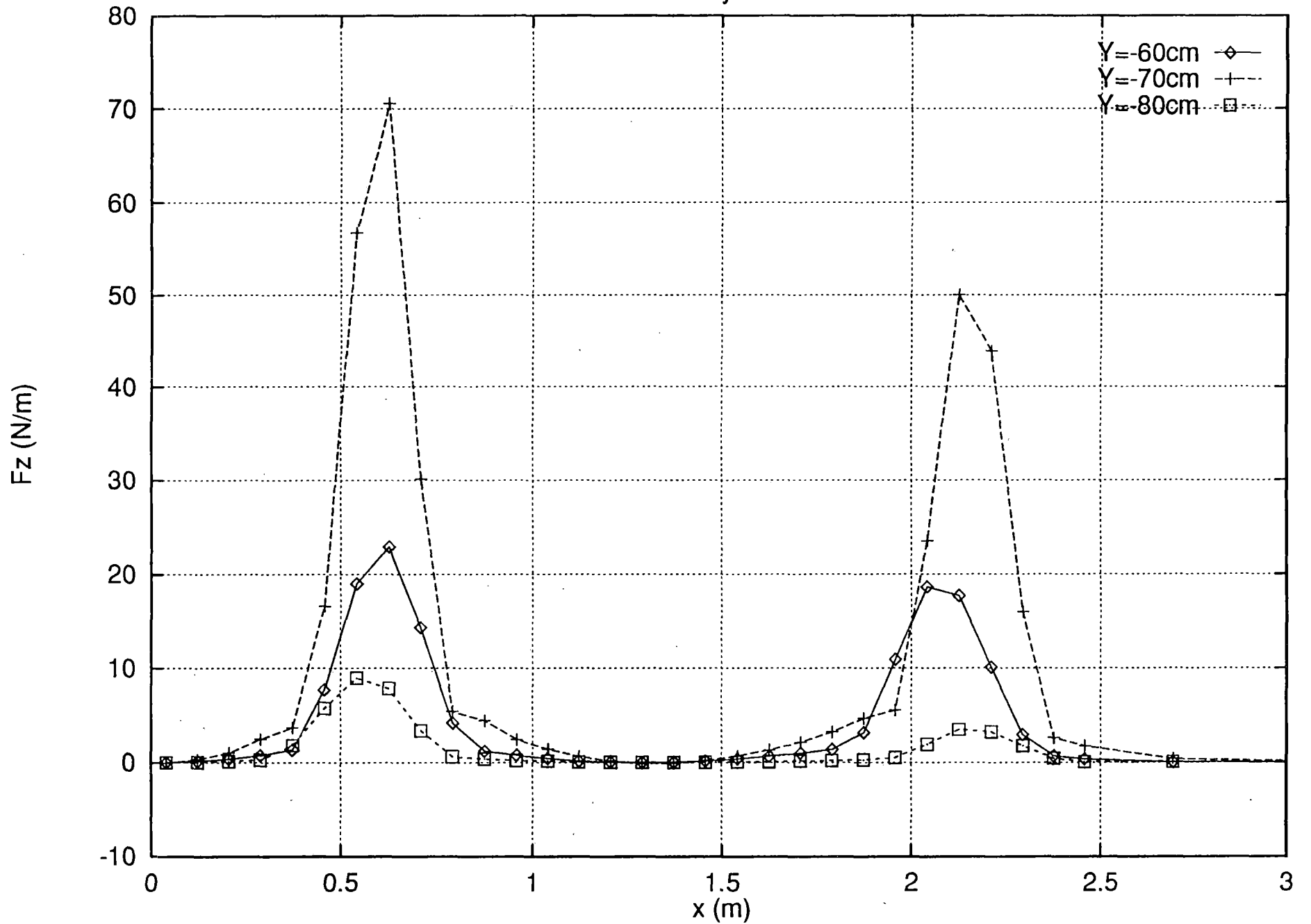
Foster-Miller Guideway Inside Rebars Z = -1



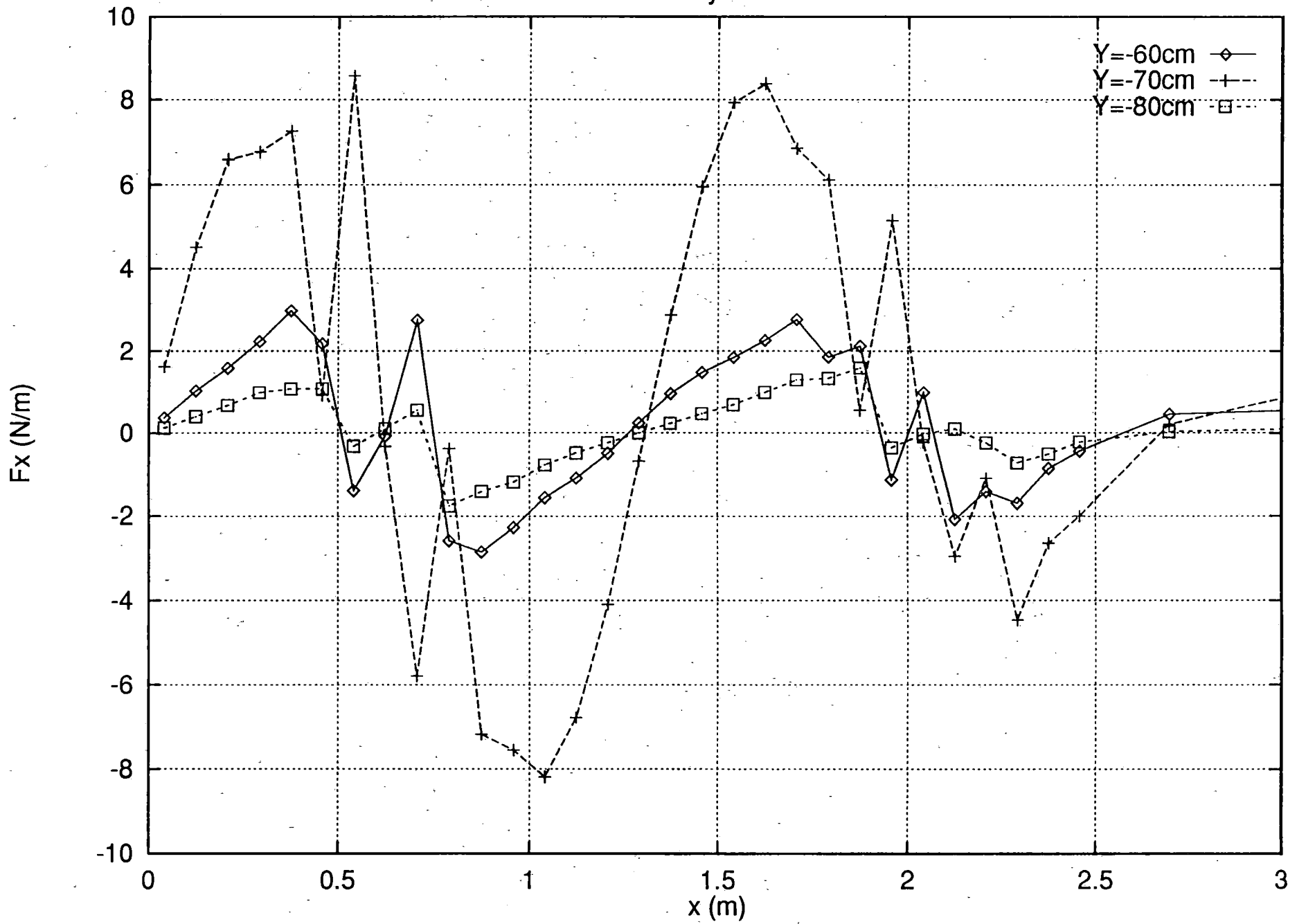
Foster-Miller Guideway Inside Rebars Z = -1



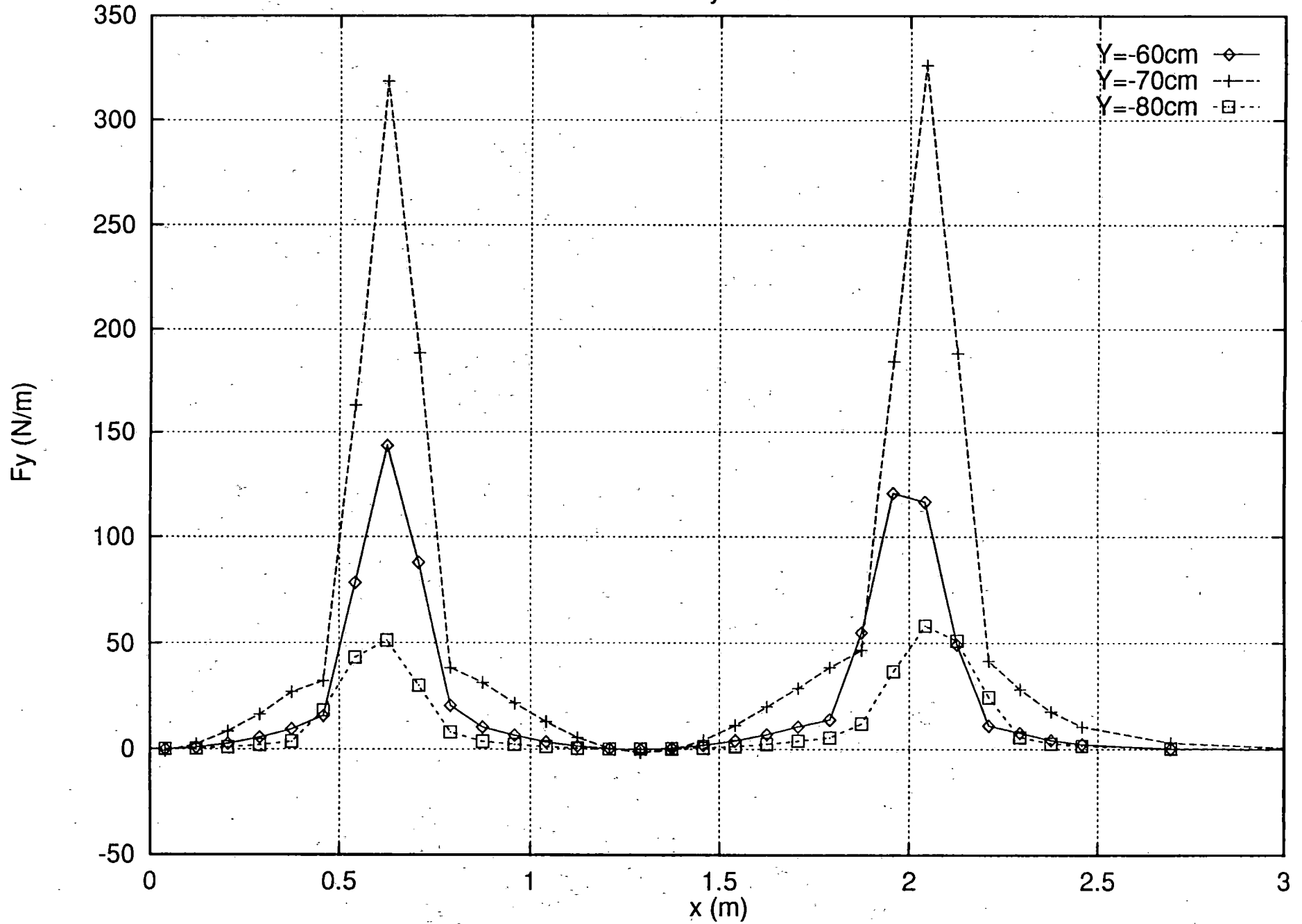
Foster-Miller Guideway Inside Rebars Z = -1



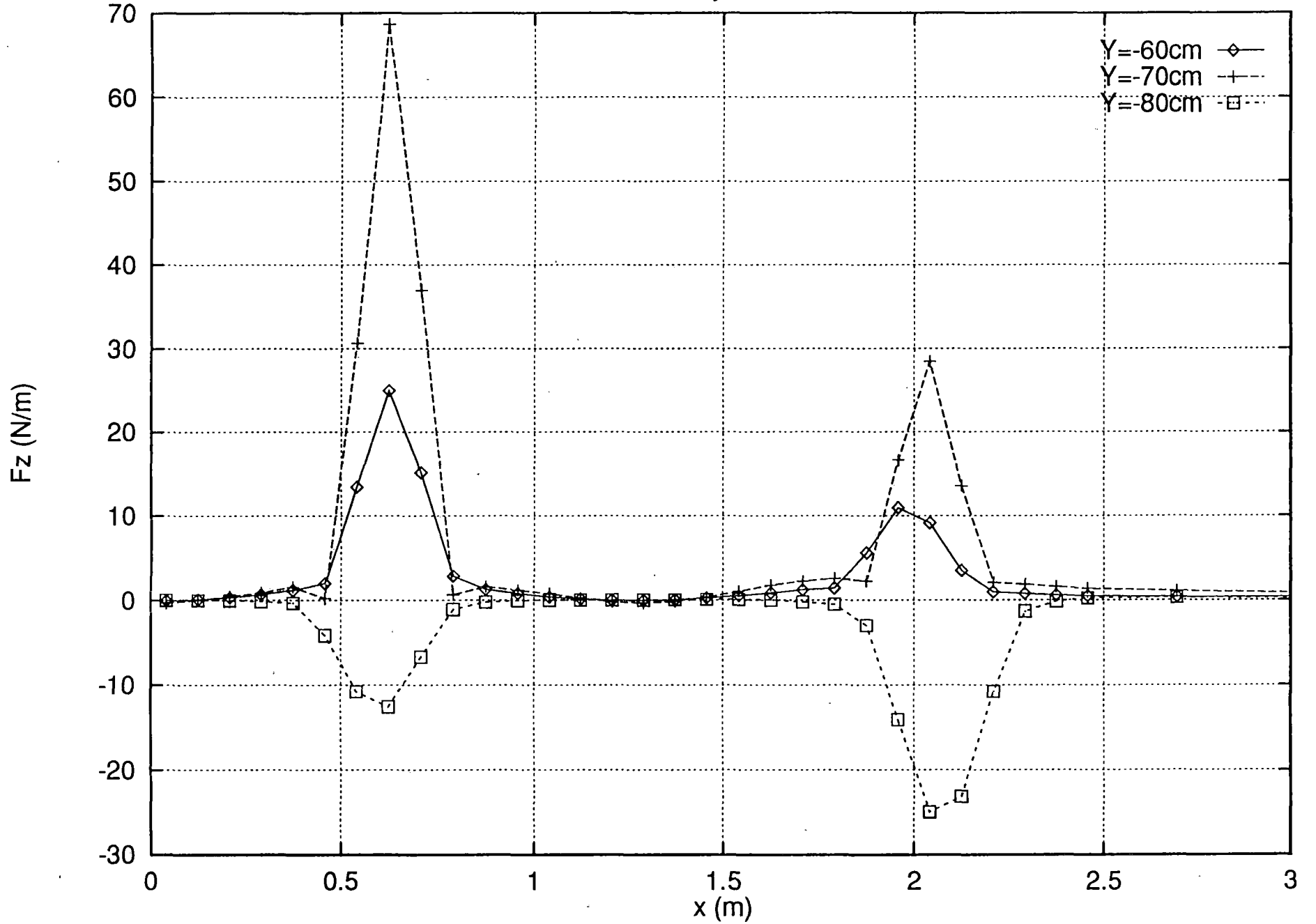
Foster-Miller Guideway Inside Rebars Z = -0.5



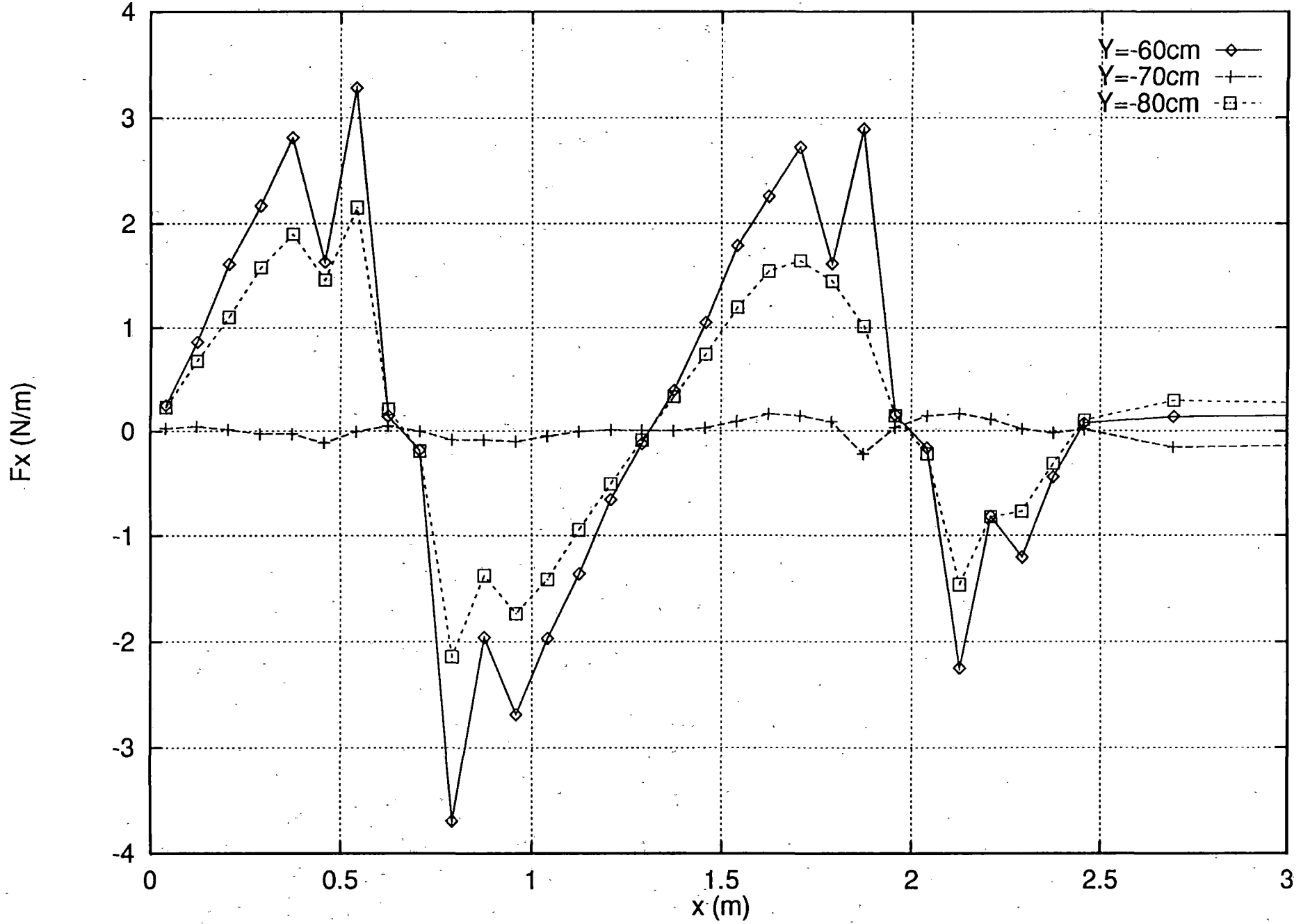
Foster-Miller Guideway Inside Rebars Z = -0.5



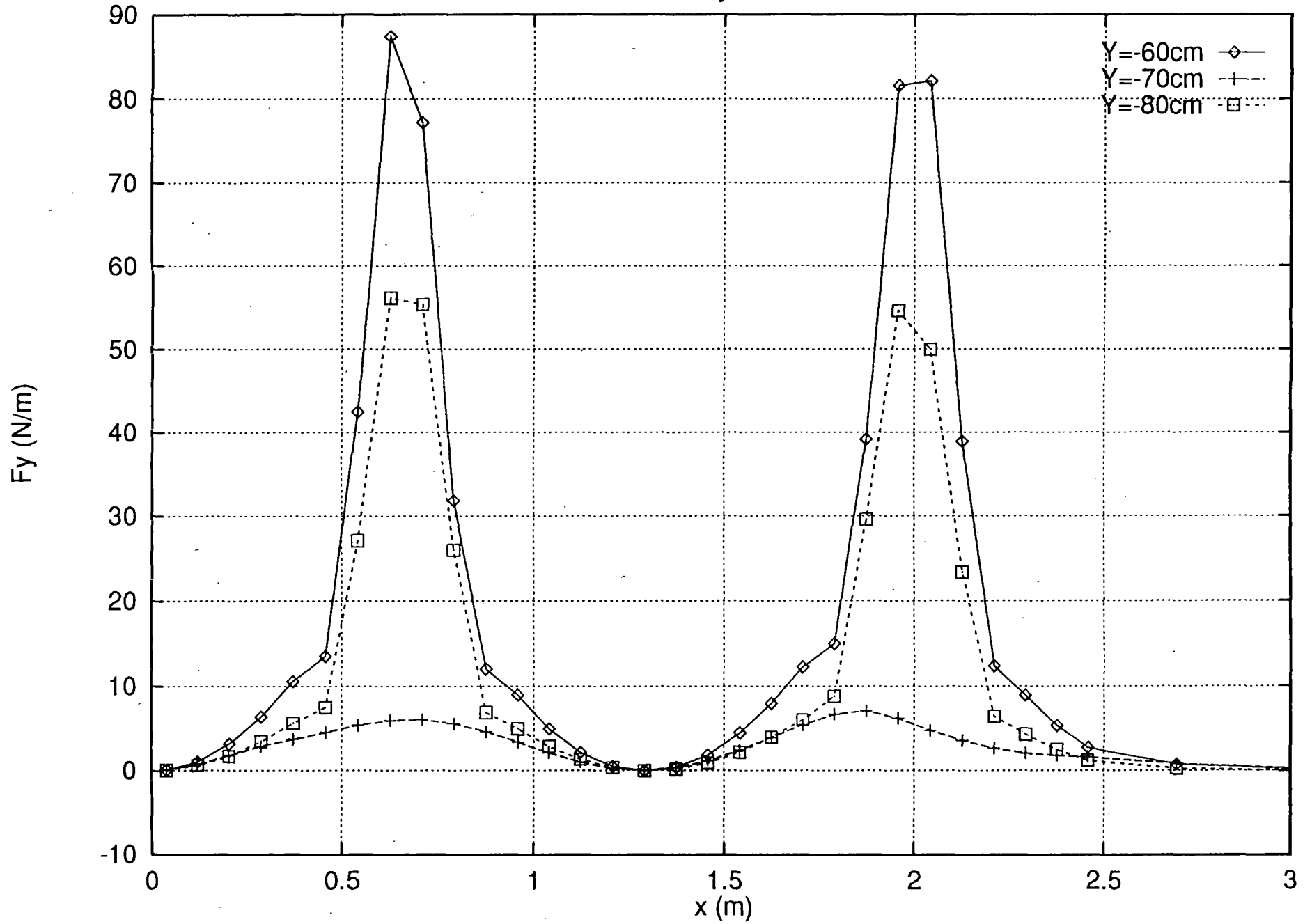
Foster-Miller Guideway Inside Rebars Z = -0.5



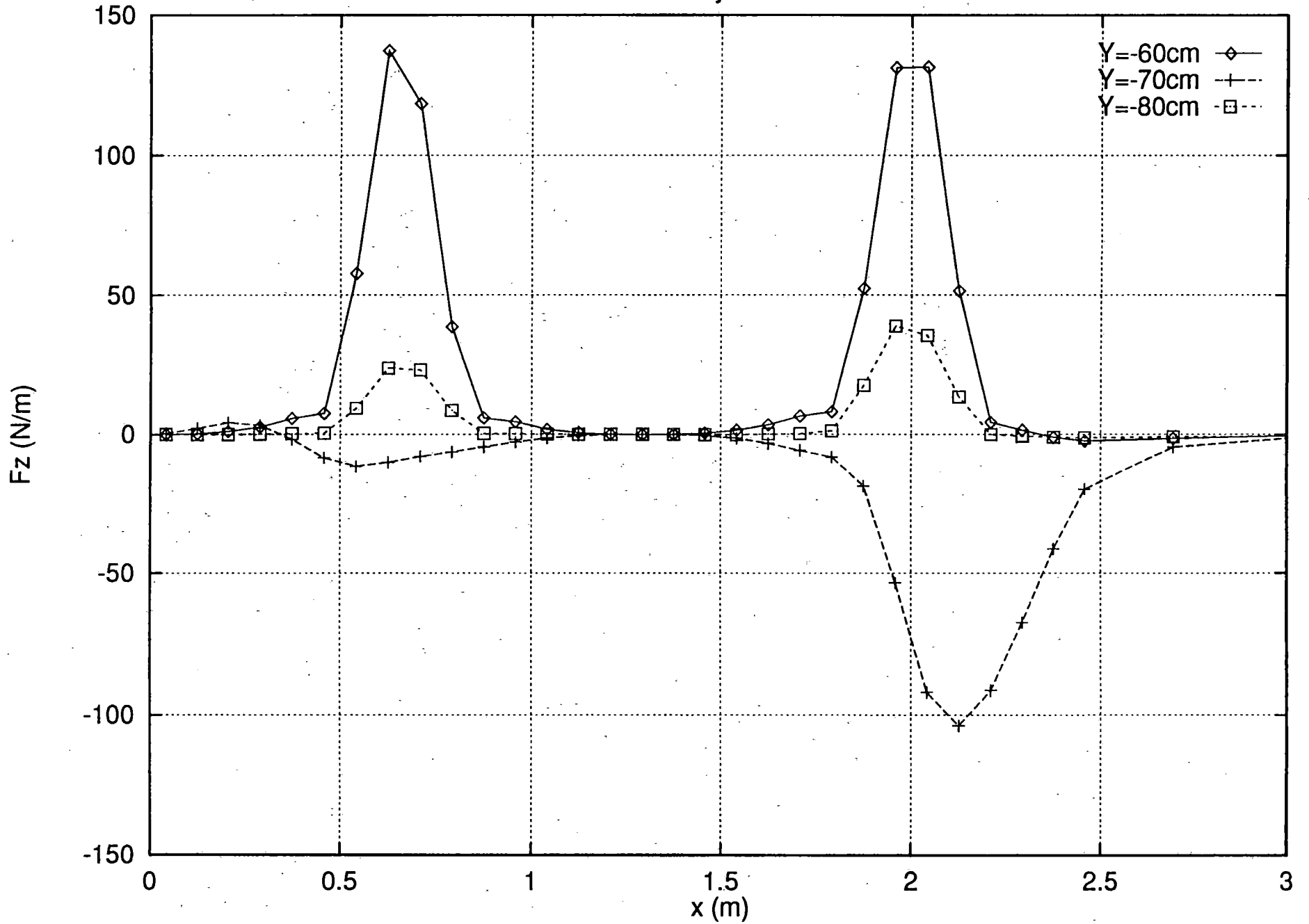
Foster-Miller Guideway Inside Rebars Z = 0.0



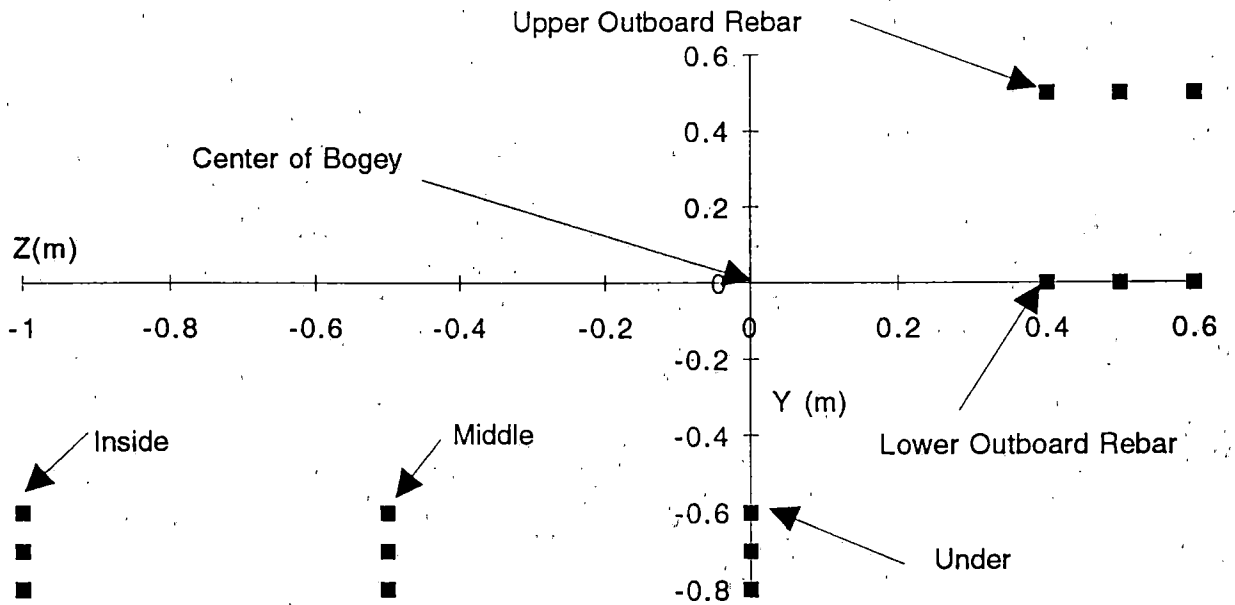
Foster-Miller Guideway Inside Rebars Z = 0.0



Foster-Miller Guideway Inside Rebars Z = 0.0



End View of Foster-Miller Guideway With Rebar Location



Calculating the Drag Force on a Maglev Vehicle
Concomitant to Motion-Induced Eddy Currents in Steel Rebars

24 September 1994

J. R. Hale and R. D. Pillsbury, Jr.

This document and all reports and memoranda in this series are intended as a record of work in progress. They are for use in informal discussions of design, fabrication and further computation alternatives. This material is subject to change and should not, therefore, be published or referred to in the open literature. Conclusions are preliminary and distribution should be strictly limited.

Massachusetts Institute of Technology
Plasma Fusion Center
Cambridge MA 02139

MEMORANDUM

Date: 24 September 1994
To: R. D. Thornton
From: J. R. Hale, R. D. Pillsbury
Subject: Memo PFC-RM-006, rebar project

Calculating the Drag Force on a Maglev Vehicle Concomitant to Motion-Induced Eddy Currents in Steel Rebars

Introduction

Energy dissipated as resistive heating in conducting rebars in concrete maglev guideways is concomitant to a drag force on the vehicle's levitation magnets. In this memorandum, we develop a simple equation from which this drag force can be estimated. In order to utilize the equation, one needs to know the number of magnets on the vehicle in the direction of motion, and the eddy current dissipation, which is a function of both the peak field at a given rebar grid and the vehicle velocity.

Derivation

One goal of this derivation exercise is to make use of previous work on this project, in which eddy current heating in rebars was expressed in terms of Dissipation per Unit Length of rebar per Cycle of magnetic field exposure[1]. Graphs were drawn to enable a reader to find this energy loss either as a function of frequency, equivalent to [velocity]/[pole-pair pitch], for different peak field exposures, or as a function of peak field at various frequencies.

As a starting point, we can write

$$P_d = F_d v$$

where P_d is the power, or energy dissipation rate [watts], attributable to eddy current losses in the rebar, F_d is the concomitant drag force [newtons] on the vehicle, and v is the velocity of the vehicle [m/s]. Keeping in mind our previously stated goal for the derivation, we rewrite this equation as follows:

$$F_d = \frac{1}{v} N_b \frac{\Delta E}{\Delta t}$$

where N_b is the number of pulse bursts per vehicle transit, $\Delta E = \Delta E(B_0, v)$ is the energy dissipated per burst, and Δt is the time interval during which that energy is deposited in the rebar.

The term "pulse burst" as used herein refers to the nature of the magnetic field waveform at the rebars. If, as is typically the case, the coils are mounted on a vehicle as opposing pairs (in the direction of motion), each pair will produce two field excursions of opposite polarity, or one "cycle" of field exposure. The transit of a vehicle past a given point produces a stream of magnetic field cycles, or "pulses. A pulse burst, then, refers to a series of such pulses that does not contain a significant "dead" zone: following are two examples of the use of this nomenclature.

In the Foster-Miller concept design vehicle, sixteen magnets are mounted on two bi-lateral bogies, one at each end of the vehicle. Each bogie structure holds four starboard and four port magnets. The mounting geometry, then, is such that on each side of the vehicle, there are two groups of four coils. In the terms described above, a given rebar will be exposed to two pulse bursts per vehicle transit, each burst comprising two pulses, or cycles.

The Bechtel concept design vehicle, on the other hand, has ninety six coils housed in twelve single-sided bogies; the six bogies on each side are mounted such that the gap between successive magnets in adjacent bogies (in the direction of motion) is exactly equal to the gap between successive magnets within a bogie. In the direction of motion, then, there are two sets of twenty-four coils, one above the other, on both sides of the vehicle: given rebar will be exposed to a single burst of pulses for each vehicle transit, each burst comprising twelve pulses, or cycles.

The energy term in the previous equation can be expressed as

$$\Delta E = \frac{1}{2} N_b N_m \mathcal{L}_r N_r \mathcal{E}(B_0, v)$$

where N_b is the number of pulse bursts per vehicle transit, N_m is the number of magnet coils corresponding to each burst, \mathcal{L}_r is the effective length of any rebar exposed to each burst at any instant in time, N_r is the number of rebars exposed to the loss level, \mathcal{E} , and \mathcal{E} is the eddy current heating loss, in units of j/m-cycle, or in strict SI units, [j/m], which is equivalent to the unit of force, newtons. (Note that because the loss level is expressed in terms of loss per cycle, the energy term above could be written in terms of the number of cycles per pulse burst. However, we feel that designers are more likely to think in terms of numbers of coils rather than cycles: the number of cycles is just half the number of magnets, or $N_m / 2$, along the direction of motion, hence, the factor of 1/2 in the above equation.) The time interval over which the corresponding pulse burst takes place can be written

$$\Delta t = \frac{\mathcal{L}_b}{v}$$

and so,

$$F_d = \frac{1}{2} N_b N_m N_r \mathcal{E}$$

The loss level, $\mathcal{E}(B_0, v)$, was the subject of the previously cited memorandum[1], in which values were plotted both as a function of frequency (proportional to vehicle velocity and inversely proportional to magnet spacing), and as a function of peak field at a rebar. This quantity embodies the geometry of the magnets and the guideway, operating current of the magnets, magnet-to-guideway separation, rebar properties, and other physical parameters of a given maglev system. Hence, a reader would need only to generate plots of the loss term, $\mathcal{E}(B_0, v)$, for a system under study, and then, utilizing these same plots, estimate the drag force that corresponds to the eddy current heating loss, by applying the equation derived above.

One of our specified tasks is to apply the design guidelines developed in the early phases of the project to two representative systems, those of the Bechtel and Foster-Miller teams. The drag force calculation described herein will be applied to these two examples, and the results presented in a separate memorandum.

References

1. J. R. Hale, J. Feng, and R. D. Pillsbury, Jr., PFC-RM-004 (inter-project memorandum) July, 1994.